AFOSR-TR-97-0459 ATCH 6

REPORT DOCUMENTATION PAGE

Form Approved
OMB No. 0704-0188

1. AGENCY USE ONLY (Leave Blank)	2. REPORT DATE	3. REPORT TYPE AND DATES COVERED
	6/28/95	Final Technical Report

4. TITLE AND SUBTITLE
Anomalous Ionization Studies:
Investigations of the Critical Ioniaztion Velocity (CIV) Phenomenon in Space

5. FUNDING NUMBERS
PE-61102F
PR-2308
SA-AS
G-F49620-93-1-0222

6. AUTHOR(S)
Edgar Choueiri and Robert Jahn

7. PERFORMING ORGANIZATION NAME(S) AND ADDRESS(ES)
EPPDyl, MAE Dept. E-Quad
Princeton University
Princeton, NJ 08544

8. PERFORMING ORGANIZATION REPORT NUMBER

9. SPONSORING / MONITORING AGENCY NAME(S) AND ADDRESS(ES)
AFOSR/NA
110 Duncan Ave., Suite B115
Bolling AFB ,
Washington DC 20332-0001

10. SPONSORING MONITORING AGENCY REPORT NUMBER

11. SUPPLEMENTARY NOTES

12a. DISTRIBUTION / AVAILABILITY STATEMENT
Approved for public release; distribution is unlimited.

12b. DISTRIBUTION CODE

13. ABSTRACT (Maximum 200 words)

The research work we conducted under AFOSR support aimed at a detailed study of the fundamentals of the phenomenon of anomalous ionization and its relevance to plasma thrusters. Ionization can represent a major energy sink for plasma accelerators and can thus have a large impact on their thrust performance in general and efficiency in particular. In this project, we combined, analytical, numerical tools with space experiments in order to develop various complementary descriptions of the complex and fundamental problem of collective (or anomalous) ionization. We used the insight gained from these fundamental studies to develop a model for the role of collective ionization in plasma thrusters. The model relates the atomic physics associated with ionization to the collective plasma physics through a prescription of an electron energy distribution function (EDF) that can represents the effects of plasma instabilities namely the creation of suprathermal electron populations. The model is cast in terms of effective bulk and tail temperatures that allows the use of the model in macroscopic descriptions of plasma thrusters.

14. SUBJECT TERMS	15. NUMBER OF PAGES
Plasma thrusters, MPD thrusters, Anomolous ionization, Critical Ionization Velocity (CIV), Active Space Experiments, Neutral Gas Release.	98
	16. PRICE CODE

17. SECURITY CLASSIFICATION OF REPORT	18. SECURITY CLASSIFICATION OF THIS PAGE	19. SECURITY CLASSIFICATION OF ABSTRACT	20. LIMITATION OF ABSTRACT
Unclassified	Unclassified	Unclassified	UL

ANOMALOUS IONIZATION STUDIES: Investigations of the Critical Ionization Velocity (CIV) Phenomenon in Space

AFOSR Grant No. F49620-93-1-0222

FINAL TECHNICAL REPORT
(Feb 93-March 95)

Edgar Y. Choueiri and Robert G. Jahn
Electric Propulsion and Plasma Dynamics Lab. (EEPDyL)
Princeton University
Princeton, NJ. 08544

Scientific Collaborators:
Hideo Okuda *Princeton Plasma Physics Lab.*
Torsten Neubert *Space Physics Lab., Univ of Michigan*
Viktor Oraevsky, Vladimir Dokukin and Alexander Volokitin
IZMIRAN, Russia

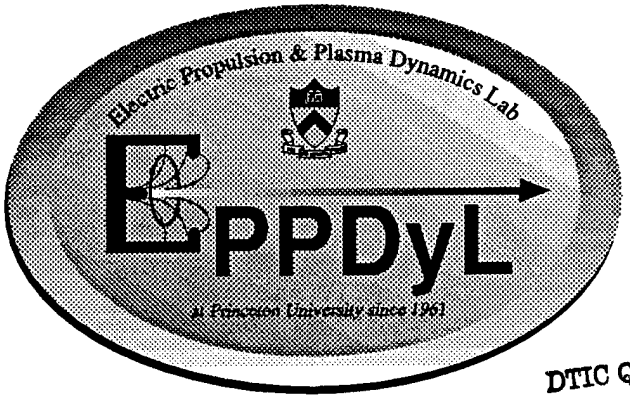

Contents

List of Figures

List of Tables

ANOMALOUS IONIZATION STUDIES: Investigations of the Critical Ionization Velocity (CIV) Phenomenon in Space

AFOSR Grant No. F49620-93-1-0222

FINAL TECHNICAL REPORT
(Feb 93-March 95)

Edgar Y. Choueiri and Robert G. Jahn
Electric Propulsion and Plasma Dynamics Lab. (EEPDyL)
Princeton University
Princeton, NJ. 08544

Scientific Collaborators:
Hideo Okuda *Princeton Plasma Physics Lab.*
Torsten Neubert *Space Physics Lab., Univ of Michigan*
Viktor Oraevsky, Vladimir Dokukin and Alexander Volokitin
IZMIRAN, Russia

1 Synopsis

The research work we conducted under AFOSR support aimed at a detailed study of the fundamentals of the phenomenon of anomalous ionization and its relevance to plasma thrusters. Ionization can represent a major energy sink for plasma accelerators and can thus have a large impact on their thrust performance in general and efficiency in particular. In this project, we combined, analytical, numerical tools with space experiments in order to develop various complementary descriptions of the complex and fundamental problem of collective (or anomalous) ionization. We used the insight gained from these fundamental studies to develop a model for the role of collective ionization in plasma thrusters. The model relates the atomic physics associated with ionization to the collective plasma physics through a prescription of an electron energy dis-

tribution function (EDF) that can represents the effects of plasma instabilities namely the creation of suprathermal electron populations. The model is cast in terms of effective bulk and tail temperatures that allows the use of the model in macroscopic descriptions of plasma thrusters.

In this project we have carried the following five parallel activities:

1. Planned and conducted active space experiments in the ionosphere to study details of anomalous ionization.
2. Reduced and calibrated data obtained from these experiments
3. Used analytical methods to interpret and model the space experiments.
4. Used advanced particle codes to interpret and model the space experiments.
5. Modeled the ionization rates in the MPD thruster.
6. Used the resulting insight to synthesize an overall description of the role of anomalous ionization in plasma thrusters.

In this final technical report we describe all of these activities.

1.1 Report Organization

In Section 2 we present an introduction to the underlying concepts and a description of the various facets of the investigation.

In the first few sections we turn our attention to active space experiments designed specifically for the study of collective ionization.

Under AFOSR support we have been involved with two active space experiments during which CIV (Critical Ionization Velocity) tests were conducted. The first series of tests was part of the ATLAS-1 experiment on board the space shuttle Atlantis. Our involvement with ATLAS-1 was in the data reduction, analysis, simulation and modeling. The second series of CIV tests was conducted on board the Russian APEX satellite.

In Section 3 we focus on the neutral gas releases conducted on board ATLAS-1. After a discussion of the experimental conditions and hardware we evaluate and discuss various criteria that, in principle, must be satisfied in order to insure a positive CIV test (i.e. ionization of the released gas due to the effects of plasma instabilities). We show that most of these criteria were well satisfied for the releases in question.

Following that we present an analysis of the optical data which shows clear signatures of emission from the plasma during each of the xenon releases. Finally we present the wave data recorded during the releases and show that each of the releases coincided with a clearly detectable plasma emission in the oxygen lower hybrid range.

In Section 4 we present our efforts towards a linear description of the dominant wave modes expected to be excited during space tests of CIV and apply the resulting dispersion to the ATLAS-1 releases. We calculate the frequencies and growth rates of these waves as well as their wavelengths and compare the latter with the characteristic lengths of the interaction. This analysis again shows the prominence of lower hybrid waves in the interaction. A more detailed look at the wave generation beyond the linear evolution stage (and their effects on particle heating and ionization) can only be obtained through the numerical particle simulation discussed in Section 7.

In Section 5 we present analytical models developed to study specific aspects of the CIV space tests. Specifically we address in that section the Langmuir probe data and present a model that attempts to account for the density enhancement *without* invoking any ionization processes such as CIV. The model addresses the possibility of ionospheric oxygen ions scattered off the released xenon gas, reaching the Langmuir probe and causing the observed density enhancement. A tracing of the orbits of scattered oxygen ions to the Langmuir probe was made inside flux tubes and the resulting flux was integrated at the probe to estimate the density enhancement. We shown that the resulting enhancement under the most favorable conditions is considerably short of accounting for the observed density enhancement. This finding devaluates the role of particle scattering in causing the plasma enhancement thus further increasing the likelihood of a role for an ionization mechanism such as CIV in the enhancement.

In Section 6 we discuss the releases we conducted from the Russian APEX satellite. We present a description of the experiments and the resulting data.

In Section 7 we present our work on advanced particle simulation of the details of the space releases we are studying. We focus on the interpretation of such experiments using plasma particle simulation (PIC codes). The goal here is to gain insight into the basic aspects of anomalous ionization. For this purpose, a 2-1/2-D particle simulation model has been developed in order to study neutral gas release experiments into the ionosphere from a satellite. The electrons are assumed guiding center particles while the full dynamics of the ions (with real masses) are followed in time and space. Ionization processes of the neutral gas including charge exchange and electron impact are included by means of the Monte Carlo technique. So far we have applied the model to the Atlas-1 xenon releases. The simulation results show how suprathermal electrons produced by a beam instability of the lower hybrid mode, create, through electron impact, a xenon ion population that exceeds that produced by classical (thermal) means, indicating the prevalence of a CIV-type mechanism. These simulations provide the most complete and self-consistent picture of the interaction and correlate well with the observed data.

In Section 8 we apply the insight gained from the numerical and experimental studies of the CIV phenomenon to the problem of ionization in plasma thrusters. In particular, we present a prescription for the electron energy dis-

tribution function that allows the representation of suprathermal electron tails such as those produced by the nonlinear effects of plasma microturbulence. The model is specified by a bulk temperature, a tail fraction, a tail energy scaling parameter and a tail spread parameter. The parametric distribution function is combined with a multi-level atomic model of argon and used to calculate the reaction rates for 23 collisional excitation transitions from ground state by electron impact by applying a high-accuracy quadrature on the convolution integrands containing the appropriate cross-sections. The prime goal was the study of the parametric dependencies of the minimum ionization characteristic length on the tail parameters. Calculations are compared with the recent measurements of the dimensions of an ionization "front" observed in a low-power MPD thruster by Randolph et. al. The ionization length which is at least 10 times smaller than that calculated assuming Maxwellian statistics is shown to be more consistent with distributions having suprathermal tail fractions and energies that could be produced by plasma microturbulence. Tail fractions of about 1%, under some conditions, can reduce the spatial extent of ionization to the millimeter level. Typical tail parameters obtained from a particle simulation code designed for the study of anomalous ionization were used to illustrate the model's implications. The model is cast in terms of effective bulk and tail temperatures that allows the the model to be coupled to macroscopic flow models of plasma thrusters[1].

2 Introduction

Ionization represents a largely irrecoverable energy sink in magnetoplasmadynamic (MPD) thrusters (as well as other types of plasma thrusters) and thus directly impacts their thrust efficiency. This is mostly due to the fact that, for typical temperatures and pressures of most plasma thrusters, the plasma flow through the chamber is essentially "frozen" with respect to recombination[5] (i.e. the plasma residence time scale is much shorter than the recombination characteristic time). While anode region losses dominate at low power levels, at higher power (above 100 kW) ionization losses become more dominant, as a fraction of the thrust inefficiency, for many propellants and under nominal operation.

A spectroscopic investigation of the ionization process in the MPD thruster conducted recently in our laboratory[2] has yielded the first hard evidence implicating anomalous ionization. The study found that classical ionization rates are exceeded by two to four orders of magnitude. Such findings effectively imply that the role of plasma microinstabilities in enhancing ionization must be invoked. This has reinforced our earlier theoretical speculations[6] on the role

[1]Provided that a model for electron heating by the unstable modes exist and is cast in terms of macroscopic parameters. Such a model for the case of the MPD thruster was developed under a previous AFOSR grant in the context of anomalous transport[4].

of the critical ionization velocity (CIV) phenomenon in MPD thruster physics.

The critical ionization velocity (CIV) phenomenon is an instability-driven ionization process that is central to many problems in plasma dynamics. It has been first hypothesized by Alfvén in 1942 and then invoked in the context of cometary physics, the formation of the solar system, planetary tori and more practically interaction of spacecraft exhaust with plasma environment, ionization processes in plasma guns and self-field MPD thrusters (see the review in ref. [7]).

In all situations where CIV is invoked, a plasma microinstability (of the streaming type) is believed to heat (through the resulting turbulence) the high energy population of the electrons thus significantly enhancing electron-impact ionization. Since the relative motion becomes strongly coupled to the ionization process through the instability, an equipartition of energy leads to the breaking of the relative motion of the plasma down to a characteristic velocity u_{ci}

$$u_{ci} \equiv \sqrt{2\epsilon_i/M} \tag{1}$$

that is dependent on the ionization potential (ϵ_i) and mass (M) of the neutral atom and is called *critical ionization velocity*. The characteristic velocity u_{ci} thus plays a threshold role for the initiation of enhanced ionization.

In the self-field MPD thruster the ionization and acceleration processes can become coupled through a current-driven instability. A CIV-type interaction can thus result without a relative motion between ions and neutrals since the relative motion between ions and electrons (i.e. the current) can provide the source of energy channeled by the instability to the ionizing electrons.

The presence and importance of current-driven microinstabilities in the MPD thruster have been unambiguously proven by theoretical, numerical and experimental work in the past 5 years[8, 9]. The unstable modes have characteristic frequencies much like the unstable modes excited by the ion-streaming instabilities behind the space manifestations of CIV. Moreover, the importance of u_{ci} as a characteristic velocity and scaling parameter in the performance of MPD thrusters has been demonstrated in 1985 through experimental testing of an MPD thruster with various propellants[6] (argon, krypton and xenon).

2.1 Review of Previous Work

Until recently, there has been only *indirect* evidence that the ionization might be related to collective effects (i.e. oscillations and turbulence in the plasma). Early speculations[6] (1985) were motivated by the importance of the critical ionization velocity as a scaling parameter and its ability to reduce measured voltage or thrust curves of self-filed thrusters to one curve largely independent of mass flow rate or propellant for many monatomic gases[10]. Scaling with v_{ci} is characteristic of many situations in plasma dynamics[11] where collective effects are present. In CIV situations, plasma instabilities extract available

kinetic energy from the flow and use it produce suprathermal electrons that can substantially enhance ionization, thus tying the directed flow energy to the ionization sink.

The earliest experimental evidence of anomalous ionization (1968) comes from a spectroscopic study by Abramov et .al. that was briefly reported in [12]. In that study, a thin ionization front was observed upstream in the chamber and had a thickness much smaller than the classical ionization length. In the same study, anomalously high level of radiation was also measured and could not be accounted for on the basis of a 2 eV Maxwellian electron distribution. The authors invoked collective phenomena as responsible for these effects.

Ionization in the MPD thruster has been the focus of a number of theoretical and numerical studies[13, 14, 15]. The emphasis was on either the non-equilibrium aspects of ionization or its role in ignition. There has been no attempt, to date, to address the impact of non-Maxwellian distributions, such as those produced by collective effects, on ionization.

Most recently, (1992) Randolph et. al. reported the results of a detailed spectroscopic study of ionization[2]. In that study, the ionization front was observed and its thickness measured at a few millimeters. A model for collisional excitation of argon was used to calculate the smallest ionization length that can be accounted for on the basis of a Maxwellian distribution and was found to be between 1 and 3 orders of magnitude larger than the measured value.

2.2 CIV Experiments in Space

One obstacle in studying the CIV phenomenon experimentally within the MPD thruster is the smallness of the ionization front (about 1 mm thick[2]) and its location (near the gas inlet) which render the ionization region very difficult for access by standard probing techniques.

The importance of the Earth ionosphere and magnetosphere as an ideal laboratory to test the CIV phenomenon has been widely recognized in the past 15 years[16]. The relative velocity between a neutral gas injected from a spacecraft and the background plasma is effectively the orbital velocity which is larger than u_{ci} for many gases. Moreover, the use of plasma diagnostics onboard satellites and subsatellites could allow for a thorough and parametric test of CIV.

Under AFOSR support we have been involved with two active space experiments during which CIV tests were conducted. The first series of tests was part of the ATLAS-1 experiment on board the space shuttle Atlantis. Our involvement with ATLAS-1 was in the data reduction, anaylsis, simulation and modeling. The second series of CIV tests was conducted on board the Russian APEX satellite. The analysis and modeling of these experiments are discussed in detail in this final report.

3 CIV Experiments on ATLAS-1

[2]

3.1 Background

Space Experiments with Particle Accelerators (SEPAC) was the only active experiment in the ATLAS 1 payload, which was carried into a 57 deg, 290 km orbit by the Shuttle Orbiter Atlantis on March 24, 1992. Although SEPAC was primarily a series of experiments with a 7.6 kW electron beam, in particular aimed at the creation of an artificial aurora, the second SEPAC accelerator, a plasma contactor (PC), was used to perform several tests the Alfvén's Critical Ionization Velocity (CIV) effect.

Many of the early CIV experiments in space were shaped-charge releases of alkali-earth metals in the ionosphere, and among them only the Porcupine experiment (Haerendel, 1982)[17] produced more than a few percent ionization yield. In fact, the macroscopic theory of Torbert (1990)[18] predicts only marginal prompt ionization in the ionospheric experiments reviewed by that author, including Porcupine, leaving open the possibility that some process other than CIV may have been at work in that case. Another rocket experiment with barium, CRIT II, was designed specifically to test CIV and showed a factor of 6 increase in the ambient density[19]. Subsequent analysis[20], however, revealed that most of the yield can be attributed to charge exchange collisions.

As an alternative to low ionization potential atoms such as the alkali-earth metals, high atomic weight gases have also been used to study CIV. Murad et al. [1986] proposed a Shuttle CIV experiment using N2 released through a special nozzle to enhance the formation of dimers and trimers, thus producing neutral gas molecules of sufficiently high atomic weight to give them a critical velocity below the 7 km/s orbital velocity of the Shuttle. Murad and Lai have recently conducted such an experiment on the Shuttle and obtained inconclusive results regarding te occurrence of CIV[21].

A CIV study using a xenon gas release from Spacelab was proposed in the report of the AMPS Science Working Group in 1975 (see Mobius (1979)[16]). This method takes advantage of the fact that the Shuttle orbital velocity of 7 km/s exceeds the 4.2 km/s critical ionization velocity for xenon. The first Spacelab CIV experiment was in fact performed using partially ionized argon ejected at supersonic speeds (near 20 km/s) from the SEPAC magnetoplasmadynamic (MPD) source on Spacelab 1. Although the experiment was not intended to study CIV, enhanced ionization was observed. No ionization was observed when only neutral gas was injected (Sasaki,1986)[22]. For ATLAS 1, the MPD was replaced by the xenon PC, making it possible to perform the CIV

[2]This section was co-authored with Dr. Jill Marshall of the Sowthwest Research Institute (SWRI) who was the PI for the ATLAS-1 xenon releases.

experiment as originally proposed for AMPS. Releases with only neutral gas or neutral gas and plasma can be made.

CIV studies have also been performed from free flying satellites, including barium releases from CRRES and xenon releases from the Soviet satellite ACTIVNY. While some (optical) evidence of CIV has been reported for the CRRESS releases those from ACTIVNY were reported to be negative.

Until the time the space experiments discussed in this report were undertaken, no definitive and unambiguous observation of CIV enhanced ionization has been reported from previous active space experiments.

3.2 Hardware

The SEPAC plasma contactor was a 25cm hollow cathode capable of ejecting 1.5A of xenon plasma in a continuous mode and/or .1 mole of neutral xenon (131 g/s) in 100 msec pulses. Both neutral and plasma releases were intended to aid in neutralizing the Orbiter during electron beam firings. In addition to the the PC and the electron beam accelerator (EBA), the SEPAC hardware also included a diagnostic package containing a Langmuir probe, a floating probe with three sensors, an electron energy analyzer, high and low frequency wave probes and an ionization gauge to measure ambient neutral pressure. The plasma contactor orifices are approximately 1.5 m from the diagnostic package probes. More description regarding the hardware can be found in ref. [23].

3.3 The Neutral Gas Releases

The release velocity of the xenon from the PC at the 245 psi nominal plenum tank pressure is only on the order of 100 ft/s, and therefore the neutral xenon will have essentially the orbital velocity of 7 km/s when released from the PC regardless of the orientation of the release with respect to the velocity vector. It is possible, however, to vary the neutral xenon velocity perpendicular to the earth's magnetic field by performing the release at different points in the orbit.

An experimental sequence was designed to look for enhanced ionization (beyond that due to collisions and other processes) when the Orbiter velocity vector is perpendicular to the earth's magnetic field, i.e. at high geomagnetic latitudes. A control experiment was planned to be performed when the perpendicular velocity is near zero, i.e. near the geomagnetic equator. Reference [23] describes the orientation of the shuttle in the proposed high and low latitude cases respectively. Releases of neutral xenon in both these attitudes were scheduled as part of the SEPAC CIV experiment, collectively known as Functional Objective #8, or FO8.

FO8 consists of series of 100 msec neutral xenon releases, repeated once every five seconds for five minutes. FO8 was performed twice during ATLAS 1 with Orbiter velocity perpendicular to the magnetic field: once in the FO8

high latitude configuration and once in the artificial aurora configuration (consult ref. [23]). The artificial aurora attitude is not optimum for the CIV experiment because the gas is released perpendicular to the velocity vector, i.e. not into the wake; however, we chose to take advantage of available experiment time with the Orbiter in this attitude.

3.4 Results from the Diagnostic Package

The recorded data (current and voltage) from the Langmuir probe showed that the collected current level increases by a factor of about 60 during the releases (the range is from 50 to 100). A time history of the Langmuir probe data during one of the releases is shown in Fig. (1). The average increase in the probe current is about a factor of 60 and is typical of other releases as discussed in refs [23] and [24]. These data seem to imply that a substantial increase in the ambient plasma density is directly related to the neutral gas release.

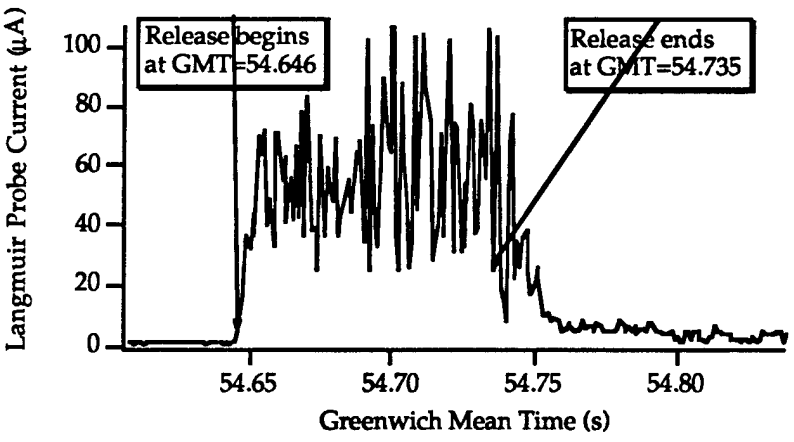

Figure 1: Time history of Langmuir probe current for the fourth release.

In addition to the Langmuir probe data, the neutral gas release on ATLAS 1 were monitored by the SPEAC plasma wave probes. For FO8, the high frequency sensor was swept from .1 to 10 MHz and the low frequency sensor was held at 2 kHz. More details on the wave hardware and the recorded wave data is presented in Section 3.7 below. It is important to state here that a clear signature of the release was observed in the wideband wave data at and near the lower hybrid frequency of oxygen (10 Khz).

FO	Attitude	Max LP Current (μA)	Vperp (km/s)	Pitch Angle (degrees)	Waves (MHz)
8-1	aurora	103	7	81	.2
8-2	CIV	112	7	90	.6-2
2-2	aurora	120 (NG+plasma) 40 (plasma) 10 (NG)	7	63	.2-2

Table 1: Table summarizing the four CIV experiments from ATLAS 1

3.5 CIV Test Criteria

We evaluated a set of necessary conditions or criteria that a CIV release in space must satisfy in order for a CIV interaction to be possible. Most of these criteria have recently been compiled and discussed by Lai and Murad (1922)[25]. We refer the interested reader to that reference for a discussion of the formulas used in the calculations reported below.

3.5.1 Parameters of Modeled Release

To compare with the CIV test criteria we selected a typical 100 msec release of xenon at 131 g/s from the FO8-1 series. The release happened on 16:11:19 UT of day 87 with a spacecraft orbital velocity of 7.4 km/s. The magnetic field strength was calculated from a geomagnetic model using the orbital parameters and was found to be .67 G. The pitch angle (angle between local magnetic field and the release velocity vector) was 81 degrees. The initial temperature of xenon the gas was 15^o and an ionization (seed) level of 10^{-8} was assumed. The gas expansion velocity was 60 m/s. To estimate the ambient oxygen plasma conditions we used the Langmuir probe current-voltage characteristics from the 5 seconds immediately preceding the first FO8, during which the applied probe voltage was swept from -9 to +9 V. This yielded an electron density of 5×10^4 cm^{-3} and an electron temperature of .1 eV.

3.5.2 CIV-prone Region

Lai and Murad[25] define a CIV-prone region bounded by distances x_1 and x_2 from the spacecraft.

The distance x_1 is the upper bound for the CIV-prone region and is obtained by requiring the ionization time scale to be shorter than the residence time scale of electrons in the spirit of a Townsend criterion for the initiation of a self-sustained discharge. For the above conditions, this distance was calculated to be $x_1 = 134$ m from the spacecraft. At the end of the 100 msec pulse the

released gas cloud would have a dimension of 6 m. Since this dimension is smaller than x_1 the release cannot be considered as a steady-state conical beam but rather as a puffed cloud.

The distance x_2 is the lower bound for the CIV-prone region and is obtained by requiring the time it takes a magnetic field line to span across the cloud to be shorter than the time needed for the electrons to be heated by the instability fueling the CIV interaction. Assuming that the latter time scale is $30/\omega_{lh}$ as suggested in ref. [26], we get $x_2 = 12$ m.

CIV is therefore restricted to happen between distances 12 and 134 m from the release point.

3.5.3 Release Velocity Criteria

Alfvén's original criterion for CIV, $v_{rel} \geq v_{ci}$, was satisfied for xenon whose v_{ci} is only 4.2 km/sec. Another inequality that must be satisfied by the relative velocity, as pointed out by Papadopoulos[27], states that the v_{rel} must not exceed $(1+\beta_e)^{1/2} v_A$ (where v_A is the Alfvén velocity and β_e is the electron beta) lest electromagnetic modes decrease the heating efficiency of the instability. This yields an upper limit for v_{rel} of 460 km/sec at x_1 and 400 m/s at x_2 implying that the criterion is initially violated near the spacecraft where the density is relatively very high ($n_e = 1.7 \times 10^{12}$ cm^{-3} at x_2 assuming an ionization fraction of 10^{-8}) but quickly becomes respected as the cloud recedes from the spacecraft (n_e drops to 2.6×10^4 cm^{-3} at x_1).

3.5.4 Magnetic Field Strength Criterion

The inequality $\omega_{pe}/\omega_{ce} > (m_e/M)^{1/2}$ was proposed by Brenning and Axnäs (1981,1990)[28, 29] to set an upper limit on the magnetic field. The smallest value for this upper limit in our particular experiment is calculated to be .04 Tesla which is well above the strength of the local magnetic field implying that the criterion is satisfied (at both x_1 and x_2).

3.5.5 Pitch Angle Criterion

Lai and Murad[25], using electron escape arguments, stated that the release pitch angle θ must satisfy the inequality $L\sigma n_e > \sin\theta > v_{ci}/v_{rel}$ where L is the dimension of the cloud and σ is the effective cross-section for electron impact ionization of xenon neutrals. This yields $33 < \theta < 90$ (at both x_1 and x_2) for our case, a condition well respected by the release.

3.5.6 Collisionality Criteria

Choueiri et al. (1985)[6] derived from a model of the rate kinetics a condition that must be satisfied by the level of collisionality of the newly produced ions in order for collisions not to disrupt the energization process. This criterion

cast in terms of a condition on the maximum allowable effective Hall parameter for the newly produced ions, Ω_{Hi}, reads $\Omega_{Hi} > 1/\left(v_{rel}^2/u_{ci}^2 - 1\right)$. This sets an upper limit on the allowable effective collision frequency for the new xenon ions which is calculated to be about 18 Hz. This criterion is clearly violated at x_2 where the neutral gas density is very high ($n_n = 1.7 \times 10^{20}$ cm^{-3}) but becomes more tenable toward the further boundary of the CIV-prone region (the effective collision frequency of the new xenon ions drops to 96 Hz at x_1).

3.5.7 Criterion for Metastable Enhancement

The ionization time from the $(6s[3/2]_2)$ metastable state of xenon is calculated to be 70 s for the conditions at x_1 and 3 μs for the conditions at x_2. Both values are lower than the metastable lifetime for that state. This implies that the likelihood of sustaining a CIV discharge for this particular release may be enhanced due to ionization from metastable states[30, 31].

3.5.8 Mass Loading

The mass loading effect may reduce the effective relative velocity through strong momentum coupling between the ions produced in the beam and the ionospheric ions[32, 25]. This effect sets an upper limit on the plasma density in the beam, n_b, given by[25] $n_b = .8 n_a M_a v_A / M_b v_{rel}$. For the conditions of our particular release this translates into a ion density yield of 10^6 cm^3 which is about a factor of 20 increase in the ambient density. It is interesting to note that this factor is of the same order as the factor by which the Langmuir probe signal was increased during the release.

3.5.9 Prospect for a CIV Interaction

The prospect for a CIV type interaction for this particular release is good judging from the application of the above criteria. The criteria are mostly (and at worst marginally) respected at distances close to x_1 from the spacecraft. One criterion not considered stipulates that the dimension of the cloud must exceed the wavelength of the unstable mode responsible for electron energization. Finally, criteria for disqualifying the possible role of other density enhancement mechanisms in these releases, such as the role of oxygen plasma scattering by the xenon cloud towards the probe, have been modelled and are presented in Section ??.

3.6 Optical Data

An optical instrument called the Atmospheric Emissions Photometric Imaging (AEPI) Instrument was used to monitor the light emission during the releases. We discuss below some relevant aspects of the instrument and the recorded data.

3.6.1 The Instrument

The part of the AEPI instrument that is of interest to us is a filtered low-light-level intensified charge-coupled device that is positioned looking outward from the bay close to both the gas release point and the plasma diagnostic package as shown in in Fig. (2).

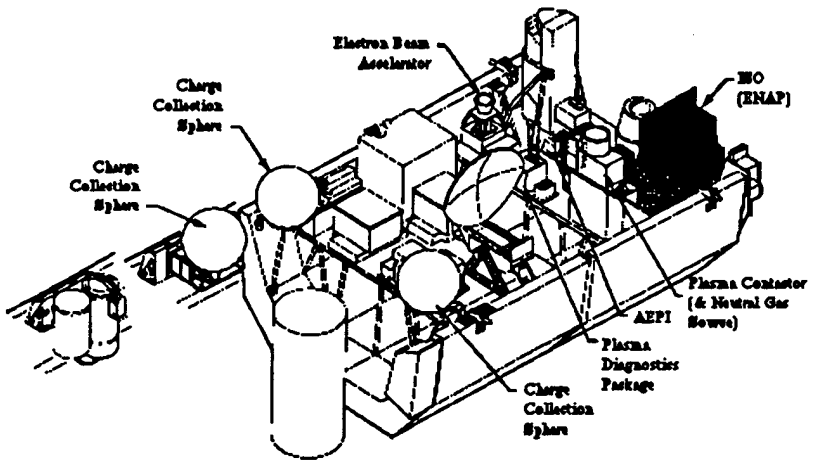

Figure 2: The SEPAC (Space Experiments with Particle Accelerators) instruments of ATLAS-1 including the DGP and the AEPI (Atmospheric Emissions Photometric Imaging) instruments (described in text) as mounted in the space shuttle payload bay.

The detector pointing range is from 40 to 155 degrees with respect to the axis normal to the space shuttle payload bay area. The instrument is originally designed for recording the light emission from natural aurora, from the shuttle glow as well as from artificial aurora excited by the ATLAS-1 electron beam. The filters were thus chosen to isolate particular line emission from magnesium and metastable oxygen ions. The filters were applied in sequences interspersed by operation with no filters i.e. continuum emission.

3.6.2 Nature of the Data

The data discussed below were reduced from the video tape of the AEPI CCD frames recorded during the FO-8 series of releases that we have discussed previously[23]. The frames were recorded at a rate of 30 frames a second. A typical frame is shown in Fig. (3).

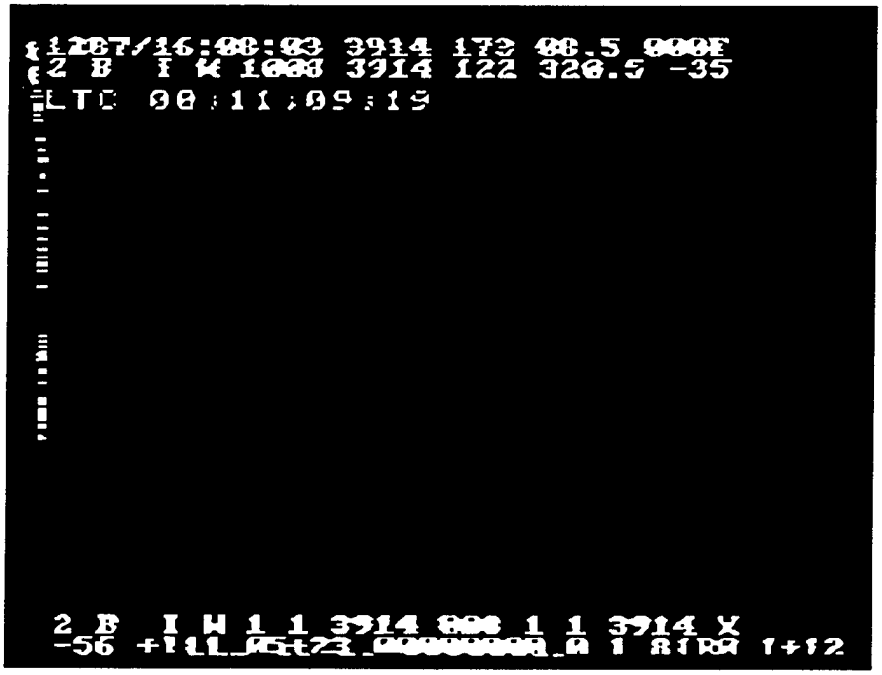

Figure 3: A typical frame from the AEPI instrument digitized in 8-bit resolution from the output tape. The frame size is 512 by 512 pixels. Some of the annotations on the frame are explained in the text.

Each frame carries a series of annotations that aid in the characterization of the various conditions under which the frame was recorded. Of most relevance to our purpose are: the first two digits on the upper left corner of the first line which denote the frame number (from 0 to 29 and resetting to 0 every second), the following eight digits which represent the Universal Time (GMT), the following 4 digits which give the value of the applied filter in Angstroms, the following three digits which denote the angle in degrees between the line of sight and the zenith, the next three digits represent the angle between the line of sight and the orbiter z-axis, the next three digits denote the angle between the line of sight and the local magnetic field vector as calculated from a geomagnetic field model, and the last digit on the first line is a letter being either F or C denoting whether the frame corresponds to filtered or continuum emission.

Other annotations give more details on the particulars of the camera position, and operation mode.

The raw frame does not offer any apparent clues to the unaided eye. It is

also impossible to discern visually, through video tape playback, any modulation in light intensity that corresponds to the frequency of the xenon gas releases (one release every five seconds). Digital data reduction and analysis were thus required.

3.6.3 Data Reduction Procedures

In order to carry a digital analysis on the frames, the video tape had to be digitized. This was accomplished using a Panasonic AG-1960 Multiplex VCR and a Macintosh IIfx computer using a 24-bit Raster-Ops digitizing Video ColorBoard 364 (run in 8-bit mode). Due to the stability of the video fields and the lack of an appropriate feedback control that could synchronize the video playback and the computer digitization, the digitization of the entire tape was done by scrolling manually each of the frames using the manual jog search control of the multiplex player[3]. The digitized frames were stored on a large capacity (1GB) optical removable disk and imported to the NIH Image 1.49 image processing package running on a Macintosh Quadra 950. Macros developed in APL specifically for this analysis were used to average and store the pixel density of each of the frames. The average was taken for a selected rectangular region of 152 by 173 pixels inside each of the 512 by 512 pixel frames. The position of the clipped region was selected based on the pitch angle information[4].

3.6.4 Results

In the last two plots we present typical data reduced from the AEPI output. The arbitrarily selected data shown in Fig. (4) cover a time starting shortly before the 40th release and ending after the 50th. The arbitrary pixel intensity are plotted versus elapsed time or frame number with 30 frames per one second of elapsed time.

The closely spaced dips in the intensity are due to filtered operation and are not relevant to the present discussion. The two remaining features in the structure of this plot are a lower frequency modulation of the intensity which can be attributed to the natural emissions from the background of the orbiter and most importantly a series of detectable and very repeatable peaks in the background intensity. That theses peaks are indicative of enhanced continuum radiation linked to the gas releases can be established by marking on the same plot the exact times the releases were made as done in that same figure. This provides one more piece of evidence for the presence of a chemically active process that is linked to the xenon releases.

[3]The authors acknowledge the help of Marlo Graves at EPPDyL who carefully undertook the tedious manual digitization of the many thousands of frames.

[4]We acknowledge the help of Steve Geller and Steve Mende of Lockheed Missiles and Space Company for their helpful comments.

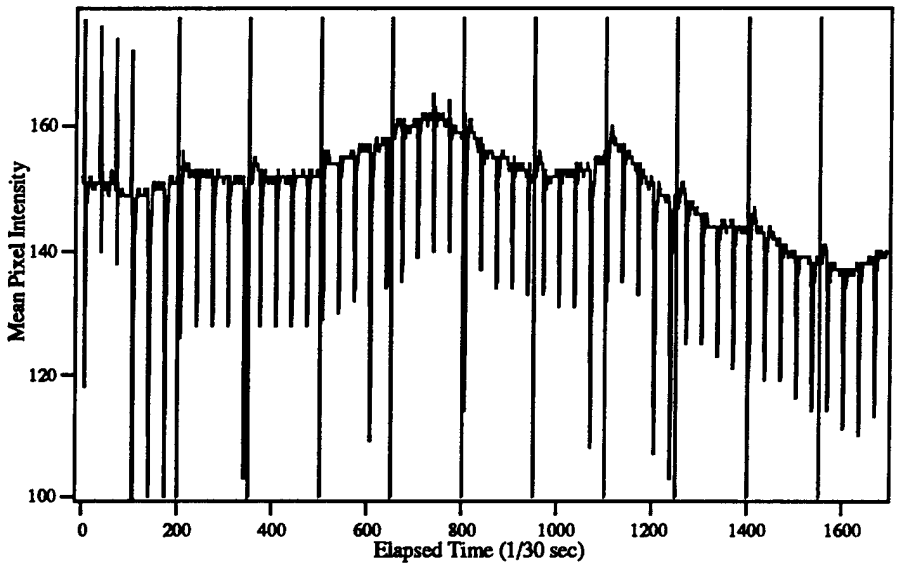

Figure 4: Typical results of AEPI data reduction showing the values of the arbitrary pixel intensity (for releases number 40 to 50) plotted versus elapsed time (or frame number with 30 frames per one second of elapsed time.) The vertical lines denote the times when the 100 msec-long releases were made. An enhancement in the continuum emission can be seen to follow each of the releases.

More information on the location of the emission region can be inferred from the same data by expanding the plot along the time axis as shown in Fig. (5) where releases 46 and 47 were chosen arbitrarily. The two closely spaced lines for each release consecutively denote the instants the valve was turned on and off. It can be seen that a delay of about 400 to 500 msec occurs from the time the valve is closed until the time the light emission is recorded. We are currently not totally sure that this delay is real. Due to shynchronicity problems between the clock on the APEI data and that of the valve on/off data we were not able to determine the exact value of this delay. This problem could not be resolved in time for this report.

If this delay is real the following calculation can offer insight into the releases. Based on the known temperature and pressure inside the xenon storage tank we calculate a thermal expansion velocity for the released xenon cloud to be between 60 and 100 m/s. This combined with the time delay we found from the above data would place the light emission region between 24 and 50 meters from

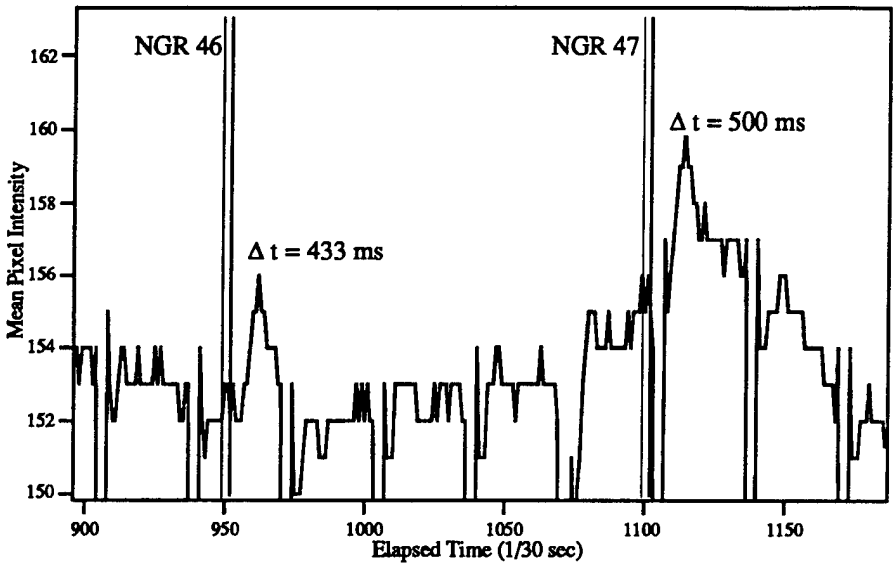

Figure 5: Data from the previous plot for two arbitrarily chosen releases (number 46 and 47) expanded to show the time resolved events of the start and end of each release (marked by vertical lines) and the time delay in light emission enhancement.

the release point. This places the interaction region well within our previously predicted CIV-prone region which was calculated to extend from 12 to 134 meters from the release point[23]. This finding cannot be confirmed pending the resolution of the clock synchronicity issue.

3.7 Probe and Wave Data

3.7.1 Plasma Wave Instruments

Th plasma wave instruments were developed by the Institute of Space and Astronautical Sciences, Tokyo, Japan. More detailed specifications including block diagrams and circuitry can be found in ref. [33].

All the wave instruments are located in the plasma Diagnostics package (DGP) whose location in the shuttle bay is shown in Fig. (2). A more detail view of the DGP and its components are shown in Fig. (6).

Four separate instruments comprise the plasma wave instrumentation. They are the three floating probes (FP), the low-frequency plasma wave probe (PWL),

the high-frequency plasma wave probe (PWH), and the wide band wave system (WB).

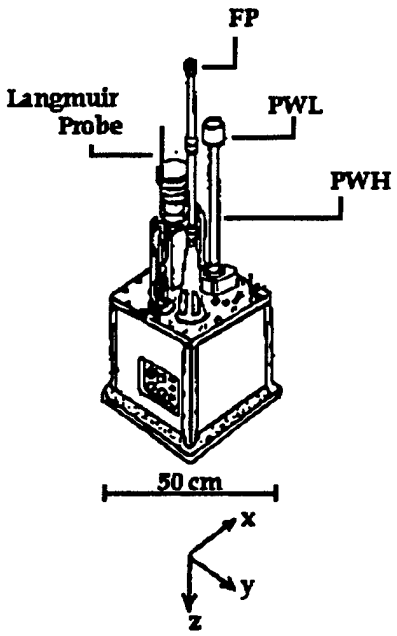

Figure 6: A detailed view of the plasma diagnostics package (DGP) showing all the instruments related to this report: The plasma floating probes (FP), the low frequency plasma wave probe (PWL), the high frequency plasma wave probe (PWH) and the Langmuir probe.

The FP sensors consist of three gold plated cylinders, 40 mm in diameter and 40 mm in length, mounted 290 mm, 540 mm and 790 mm above the top surface of the DGP on an insulated rod 25 mm in diameter. The input impedances of the first FP amplifiers are 10 megohms. The frequency range of the FP is 0-400 Hz and the outputs are sampled at a 1 ksample/s rate. The mounting location of the sensor cylinders in the payload (see Fig. (2)) probably meant that they were in the sheath of the orbiter most of the time.

The PWL measures the currents to a Faraday cup mounted on top of the PWH sensor and the potential induced on the outer cylinder of the Faraday cup. The Faraday cup is gold-plated, with an entrance aperture diameter of 40 mm. The outer dimensions of the cup are 70 mm in diameter and 75 mm high. The bottom of the Faraday cup is 435 mm above the DGP upper surface, (cf Fig. (6)).

The PWL sensors, the Faraday cup and the outer surface of the Faraday cup, after preamplification, drive two synchronized sweep frequency receivers which measure the intensity of the variations in the sensor signals over the frequency range from 750 Hz to 10 kHz. This range is divided into 255 steps and a complete sweep of the 40 Hz wide bands takes one second.

Broad band signals with a frequency range of 0.75 to 10 kHz from the Faraday cup body pass through an automatic gain control (AGC) amplifier with a 75 dB range and are passed to the Wide Band (WB) system described below.

The PWH sensor is the 30 mm diameter by 435 mm long cylinder that supports the PWL Faraday cup and which is mounted to the top of the DGP. After preamplification, the PWH signal drives a sweep frequency receiver. The sweep frequency receiver covers the range from 0.1 to 10.5 MHz, with 2046 steps, each step having a bandwidth of 10 kHz and a frequency separation of 4 kHz. The intensity of the received waves are measured once every millisecond, so that a complete sweep takes 2 seconds. The receiver can also continuously measure the wave intensity at any of the 2046 frequency steps. The range is from 2×10^{-7} to 10^{-1} Volt.

Broad band signals in frequency ranges from 0.1 to 4.2 MHz or 4.0 to 7.5 MHz (frequency shifted to 0 to 3.5 MHz in the case of the upper frequency range, 30 seconds for one frequency range, 30 seconds for the other), pass through an AGC receiver with a range of 75 dB, and are then sent to the wideband (WB) system.

The WB system combines the outputs of the AGC receivers in the PWL and PWH. ATLAS-1 then sends the composite analog signal to the Shuttle for transmission to the ground via an analog data channel.

3.7.2 Wave Data below 400 Hz

Wave data extracted from the signatures of the three floating probe were processed through an FFT and a Hanning window as described in ref. [34]. Peaks near 35, 183 and 316 Hz prevail with 25 Hz sidebands appearing on each side of many of the prominent peaks[34]. When we compared these peaks with those observed during instances immediately preceding the releases we found that none of these peaks can be clearly attributed to the releases since they seem to be ubiquitous in the background.

3.7.3 Wave Data between 400 Hz and 125 kHz

The most interesting wave activity was found in the 10 kHz range of the wideband data. The wideband data in the 400 Hz-125 kHz band is shown in Fig. (7) for the first three releases. The vertical lines at the bottom of the plot denote the time of the releases. It is obvious that the releases coincide with a pronounced narrow-band activity in the range of 6 to 15 kHz as marked by the three red vertical lines in that range. It is difficult to judge the upper frequency

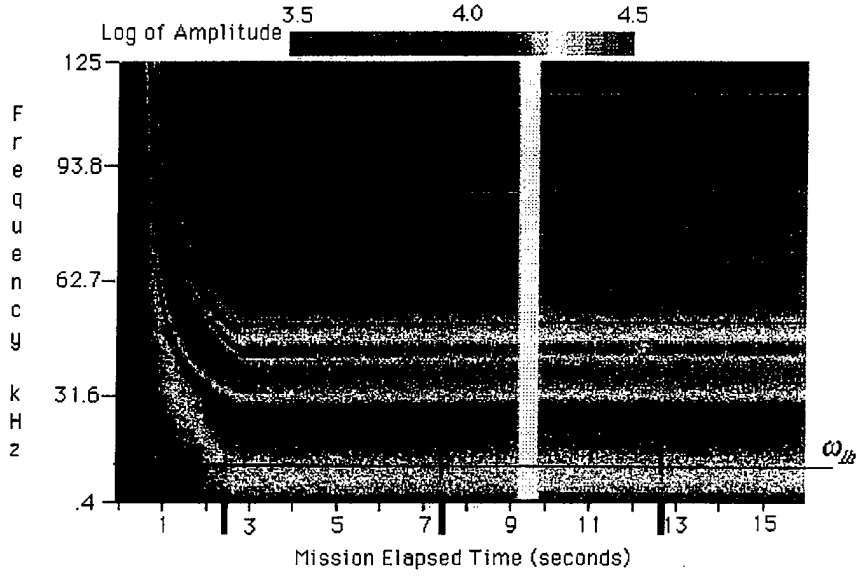

Figure 7: Wideband data in the range .4-125 kHz recorded during the ATLAS-1 CIV tests. The vertical lines at the bottom of the plot denote the time of the first three releases. The lower hybrid frequency of oxygen (10 kHz) is marked by a horizontal line across the plot.

bound of that band as it merges with natural activity (i.e. not associated with the releases) in the 20-30kHz band (seen as the bottom red strip across the plot). The lower hybrid frequency of oxygen is marked by a black line across the plot and shows that the wave activity that is associated with the releases correlates fairly well with lower hybrid waves. This is an important observation to keep in mind since our numerical simulations of these releases, described in SectionpicsecA, predict such an activity as a result of the beam instability caused by the oxygen ions counterstreaming with respect to the xenon ions created through charge exchange. It is interesting to note from the plot that the intensity of these waves is about an order of magnitude larger than the background noise.

3.7.4 Wave Data between 125 kHz and 1 MHz

In this range the only discernible signature of the releases was observed in the wide band data between 260 and 570 kHz. This portion of the data is shown in Fig. (8) for the first three releases. Two effects, related to the releases, can be discerned from this plot. During each release, there is a *decrease* by a factor

of 1.2 to 1.6 in the amplitude of oscillations with frequencies between 250 and 430 kHz. This abatement in the background noise level lasts approximately 200 msec from the time the valve is on and is followed immediately by an *enhancement* in the amplitude of oscillations with frequencies between 375 and 570 kHz. This enhancement reaches a factor of about 2.5 above background and lasts about 200 msec at 375 KhZ and tapers down to about 70 msec at 570 kHz.

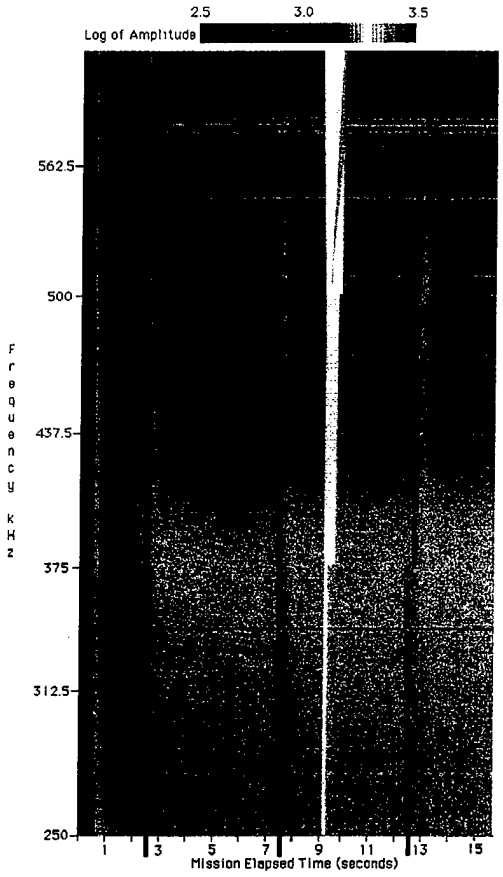

Figure 8: Wideband data in the range 250-600 kHz recorded during the ATLAS-1 CIV tests. The vertical lines at the bottom of the plot denote the time of the first three releases.

3.7.5 Wave Data between 1 and 10 MHz

The only wave data above 1 MHz that we have is the raw data from the PWH system. We described the processing of the output of the PWH system in ref. [34]. Due to the sweep operation of the instrument, the raw data we processed permits only observation of the release in a narrow frequency band that corresponds to the band being swept during the release. Each of the sixty releases showed an enhancement above background of the amplitude of the frequencies (between 1 and 10 MHz) that were being swept during the release. This implies that the releases did register a wide band signature in that range. Due to the composite nature of the data it is however difficult to construct a continuous and quantitative spectrum of the oscillations in that range *during* the releases.

3.8 Conclusions Regarding the Data from the ATLAS-1 Releases

A series of neutral xenon releases from the Atlas 1 payload Shuttle Orbiter Atlantis were made to test the critical ionization velocity (CIV) effect. The gas was released with a velocity relative to the ionospheric plasma exceeding the critical ionization velocity of xenon (4.2 km/s). The hardware, conditions and some of the, optical wave and probe data are discussed. Experiments under varying conditions show that a factor of 60 increase in the current collected by a Langmuir probe occurs during the neutral gas release along with a detectable light emission from the plasma as well as significant rf emission in the lower hybrid range. The release conditions are also shown to generally satisfy various known criteria necessary for a CIV interaction. These experiments present a well documented test case which, along with the models and numerical simulations described in the following sections, has allowed for much insight into the fundamentals of anomalous ionization.

4 Linear Dispersion Relation for Wave Emission during ATLAS-1 Releases

[5]

In this section, we present a relatively simple model for the wave generation during CIV tests in space. Of course, the PIC simulations discussed in Section 7 can give a far more accurate and realistic description of the wave emission during the releases (a description extending well beyond the linear regime) but a simpler analytical linear description has its advantages. A linear dispersion relation can give direct and "inexpensive" insight into the general features of the dominant

[5]We acknowledge the help of Brian Kantsiper, a student at EPPDyL, in carrying calculations for the material in this section.

plasma wave modes during the experiments. Moreover it may be used as the basis of quasilinear description of the CIV interaction.

Our approach is to start with a simplified dispersion relation that can be used to study the basic wave stability of a neutral gas beam interaction with a magnetoactive background plasma. Of course collective effects can only occur when the neutral gas carries a "seed" plasma that can form a counter-streaming charged particle population with respect to the background plasma.

We start with the simple case which neglects collisions and electromagnetic effects. This will allow us to explore at least the relatively manageable limits of the problem. We do not necessarily expect the predictions of the dominant wave mode obtained from this simplified dispersion relation to explain in any detail the wave activity recorded on ATLAS-1. The intent here is first to get familiar with the parameter space of the problem.

4.1 Formulation

Most probably any wave activity recorded on ATLAS-1 would represent a saturated mode (or modes). It is however customary to expect that the non-linear effects are not so dominant (weak turbulence) as to totally obliterate the *linear* aspect of the mode. In other words, it is usually hoped that the dominant mode predicted by a theory of *linear* oscillations is characteristic of the real (nonlinear) situation.

The starting point for the derivation of the dispersion relations will be the dispersion tensor derived in ref. [8]. This general dispersion relation include, kinetic, collisional, and electromagnetic (finite-beta) effects and allows for counter-streaming of charged particles in the presence of a magnetic field. Due to its complexity we shall not quote the entire tensor here. The interested reader is referred to ref. [8].

We shall restrict our study to the particular case where we neglect collisions and finite-beta (i.e. $\beta = 0$) effects but keep full kinetic effects and those of finite magnetization i.e. kr_{ce} finite, where k is the wavenumber and r_{ce} is the electron cyclotron radius. We shall restrict ourselves to the frequency band $\omega_{ci} \ll \omega \ll \omega_{ce}$ where the three quantities in the inequality represent the ion cyclotron, wave and electron cyclotron frequencies respectively. We also reduce all sums over the cyclotron harmonics to the zeroth order (fundamental) term.

Furthermore, in this first treatment we shall model the release problem with three species: 1) the beam ions representing the ionized xenon atoms of the released gas (quantities with the superscript b), 2) the ambient ions representing the ionospheric oxygen ions (quantities with the superscript a) and 3) one ambient electron population. We shall stay in the reference frame of the ambient plasma. Finally we shall add, for the sake of simplicity, the equi-thermal assumption $T_i^{(a)} = T_e^{(a)} = T_i^{(b)}$ between the three species.

Under all these assumptions, the general dispersion tensor[8] yields the fol-

lowing expressions for the susceptibilities, $\chi_i^{(a)}$, $\chi_i^{(b)}$ and $\chi_e^{(a)}$ of the three species:

$$\chi_i^{(a)} = \frac{2}{k^2 r_{ce}^2} \frac{\omega_{pi}^{(a)2}}{\omega_{ce}^2} \left[1 + \xi_i^{(a)} Z(\xi_i^{(a)})\right] \tag{2}$$

$$\chi_i^{(b)} = \frac{2}{k^2 r_{ce}^2} \frac{\omega_{pi}^2}{\omega_{ce}^2} \frac{n^{(b)}}{n^{(a)}} \left[1 + \xi_i^{(b)} Z(\xi_i^{(b)})\right] \tag{3}$$

$$\chi_e = \frac{2}{k^2 r_{ce}^2} \frac{\omega_{pi}^{(a)2}}{\omega_{ce}^2} (1 + n^{(b)}/n^{(a)}) \left[1 + \xi_e Z(\xi_e) e^{-\mu_e} I_0(\mu_e)\right] \tag{4}$$

with

$$\xi_i^{(a)} = \frac{\omega}{\omega_{lh}} \frac{\omega_{pi}^{(a)}}{\omega_{ce}} \frac{1}{k r_{ce} \left(1 + \omega_{pe}^2/\omega_{ce}^2\right)^{1/2}} \tag{5}$$

$$\xi_i^{(b)} = \left[\frac{m_i^{(b)}}{m_i^{(a)}}\right]^{1/2} \left[\frac{\omega}{\omega_{lh}} \frac{\omega_{pi}^{(a)}}{\omega_{ce}} \frac{1}{k r_{ce} \left(1 + \omega_{pe}^2/\omega_{ce}^2\right)^{1/2}} - \frac{u_r}{v_{ti}}\right] \tag{6}$$

$$\xi_e = \frac{1}{\cos\theta} \left(\frac{m_e}{m_i^{(a)}}\right)^{1/2} \frac{\omega}{\omega_{lh}} \frac{\omega_{pi}^{(a)}}{\omega_{ce}} \frac{1}{k r_{ce} \left(1 + \omega_{pe}^2/\omega_{ce}^2\right)^{1/2}} \tag{7}$$

where ω_{ps}, ω_{cs}, n_s, m_s, v_{ts} are the plasma frequency, cyclotron frequency, density, mass and thermal velocity of species s; ω_{lh} is the lower hybrid frequency, u_r is the release velocity and μ_e is defined as $\mu_e \equiv k^2 r_{ce}^2/2$. The functions Z and I_0 are the standard dispersion function and the modified Bessel function of the first kind of order zero. θ is the angle in radians between the local geomagnetic field vector $\boldsymbol{B}_0$ and the wavevector $\boldsymbol{k}$.

As usual, the electrostatic dispersion relation is given by the sum of the contribution of all the species and of vacuum:

$$1 + \chi_i^{(a)} + \chi_i^{(b)} + \chi_e = 0 \tag{8}$$

We seek the complex root ω_c defined as $\omega_c = \omega + i\gamma$ for the temporal evolution of a wave mode where ω_r is the real frequency and the imaginary part γ represents the temporal growth rate which is positive for an unstable wave mode. It is convenient to work with the dimensionless quantities ω/ω_{lh} and γ/ω_{lh} where we have chosen the lower hybrid frequency as the reference characteristic frequency.

The dispersion relation is found by tracing the root $\omega/\omega_{lh} + i\gamma/\omega_{lh}$ of the above nonlinear meromorphic as a function of kr_{ce}. The problem is completely specified by the following set of six independent dimensionless parameters:

$$\theta, \quad \frac{n^{(b)}}{n^{(a)}}, \quad \frac{u_r}{v_{ti}}, \quad \frac{\omega_{pe}}{\omega_{ce}}, \quad \frac{m_i^{(a)}}{m_e}, \quad \frac{m_i^{(b)}}{m_e} \tag{9}$$

4.2 Solutions

We now use the above dispersion relation to describe the dominant mode for the plasma parameters of the FO8-1 release of ATLAS-1 described in ref. [23]. For the plasma parameters measured during that release (T_e = .1 eV, n_e = $5 \times 10^4 \text{cm}^{-3}$ and B_0 = .67 G) we have ω_{pe}/ω_{ce} = 1.1, u_r/v_{ti} = 5.5 with $m_i^{(a)}/m_e = 2.91 \times 10^4$ and $m_i^{(v)}/m_e = 2.4 \times 10^5$ for oxygen and xenon. Since the parameter $n^{(b)}/n^{(a)}$ is the least known parameter (it depends on the instantaneous ionization fraction of the released neutral gas) we take it as a varying parameter.

Since the wave measurements on ATLAS-1 were wave power spectra and not dispersion relations we are not interested in the dispersion relation itself as much as the characteristic of the dominant unstable mode i.e. the unstable wave with the largest growth rate. For that we have solved for the dispersion relation (i.e. $\omega/\omega_{lh} + i\gamma/\omega_{lh}$ as a function of kr_{ce}) using the prescriptions described above by first setting the propagation angle θ fixed then varying kr_{ce} until the maximum positive γ/ω_{lh} is reached. The wave quantities thus obtained are called growth-maximized solutions and are plotted in Figs. (9), (10) and (11) as a function of the propagation angle θ. The growth-maximized quantities are denoted by an asterisk.

The curves in Fig. (9) show that the most unstable modes are restricted to propagation close to 90 degrees from the geomagnetic field. It can be seen from the plot that the dominant mode (i.e. the solution that is maximized with respect to both the wavenumber kr_{ce} and the propagation angle θ) is at about 89.4 degrees from the field vector.

As expected the maximized growth rate γ^*/ω_{lh} increases monotonically with the seed density within the explored parameter space. The solution for $n^{(b)}/n^{(a)} <$ .1 is essentially the same as that for $n^{(b)}/n^{(a)}$ (asymptotic solution). This implies that the dominant mode has a growth rate of about .5 ω_{lh} for an initially small "plasma seed" in the released gas. The case of $n^{(b)}/n^{(a)} = 60$ is also shown and may be of particular relevance since a factor of 60 increase in the local density was observed during FO8-1 (cf. ref. [23]).

In Fig. (10) we show the corresponding frequencies. It is important to remember that these frequencies are in the reference frame stationary with respect to the ionospheric plasma and must be Doppler-shifted before comparison with measurements made on the orbiter. The frequency of the dominant mode (θ = 1.56 radians = 89.4 degrees) is of the same order as the lower hybrid frequency for all but the cases with large $n^{(b)}/n^{(a)}$.

In Fig. (10) we show the corresponding wavenumbers. For FO8-1, r_{ce} is about 15.92 mm which implies that the maximum wavelength of the unstable mode ranges between 20 and 100 meters. This is of the order of the expanding cloud dimension as it reaches the far boundary of the CIV-prone region (cf. ref. [23]) (the cloud has a diameter of about 40 m when it reaches the far boundary). This indicates that this mode could possibly be responsible for turbulent heating

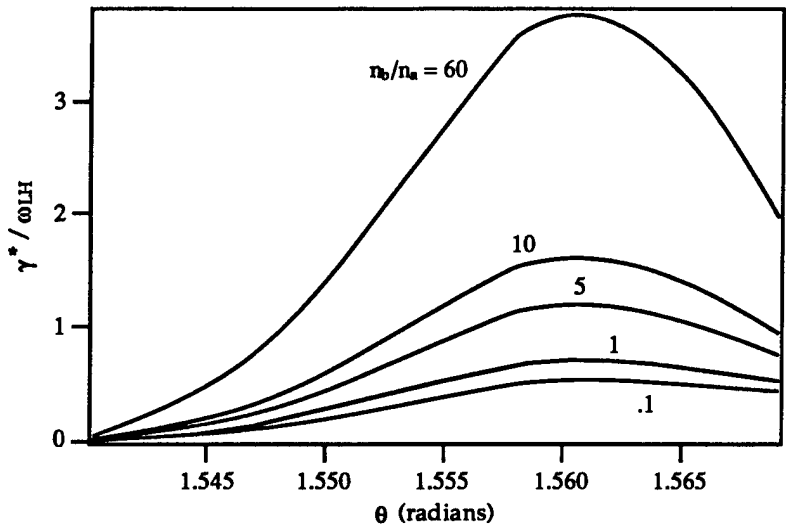

Figure 9: Instability growth rate growth-maximized over wavelength as a function of the propagation angle θ with the ratio of beam to ambient densities $n^{(b)}/n^{(a)}$ as a parameter.

within the cloud. Indeed, $\lambda^* > d_{\text{cloud}}$ is one of the criteria for positive CIV that was not evaluated in Section 3.5.3.

5 Analytical Models for ATLAS-1 CIV Tests

[6]

In the above sections we noted that lower hybrid wave emission was recorded during each of the sixty releases of experiment FO-8, also that the Langmuir probe showed that each of the releases caused a substantial enhancement to the local plasma density above that of the ionospheric background. In this section we address the Langmuir probe data and present a model that attempts to account for the density enhancement without invoking any ionization processes such as CIV. The model addresses the possibility of ionospheric oxygen ions scattered off the released xenon gas, reaching the Langmuir probe and causing the observed density enhancement. Such scattering is quite dependent on the spacecraft attitude and the release geometry as was shown by Sasaki et. al.[1]. We first show that Sasaki's model is not applicable to the ATLAS-1 release then

[6]Contribution of Jonathan Nichols, EPPDyL.

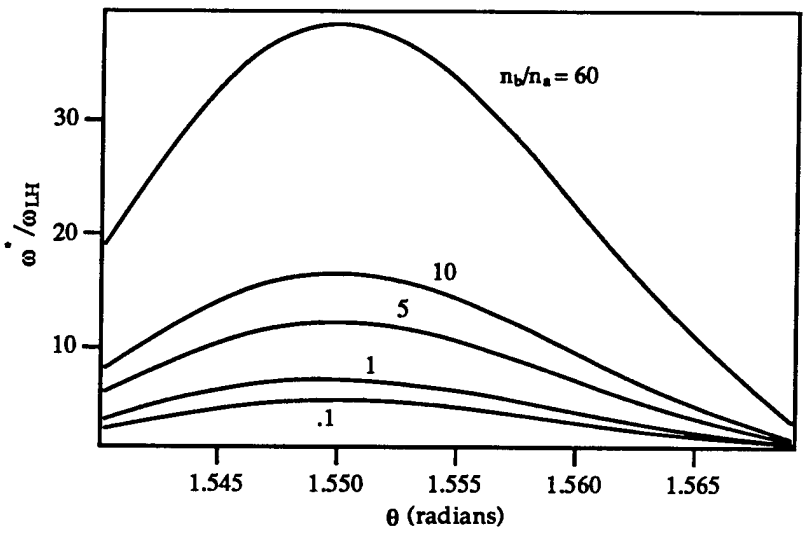

Figure 10: Wave frequency growth- maximized over wavelength as a function of the propagation angle θ with the ratio of beam to ambient densities $n^{(b)}/n^{(a)}$ as a parameter.

present an improved scattering model which among other features includes one major effect that was neglected by Sasaki et. al namely magnetization. A tracing of the orbits of scattered oxygen ions to the Langmuir probe was made inside flux tubes and the resulting flux was integrated at the probe to estimate the density enhancement. The resulting enhancement under the most favorable conditions was found considerably short of accounting for the observed density enhancement. This finding devaluates the role of particle scattering in causing the plasma enhancement thus further increasing the likelihood of a role for an ionization mechanism, such as CIV, in the enhancement.[7].

5.1 Introduction

During the ATLAS-1 mission aboard the Space Shuttle Atlantis on March 24, 1992, neutral xenon gas was released from the shuttle bay to test the occurrence of CIV as described in the above sections. Table 2 shows some of the relevant

[7]**Acknowledgments:** We thank Dr. Jill Marshall (Southwest Research Institute), Dr. Torsten Neubert (Space Physics Lab., U. of Michigan), Dr. Bob Beattie (Hughes Research Lab.), Dr. Ira Katz (S-Cubed), Prof. Peter Sarnak (Math Dept., Princeton University) and Dr. Alexander Volokitin (IZMIRAN, Moscow) for stimulating discussions and/or useful information.

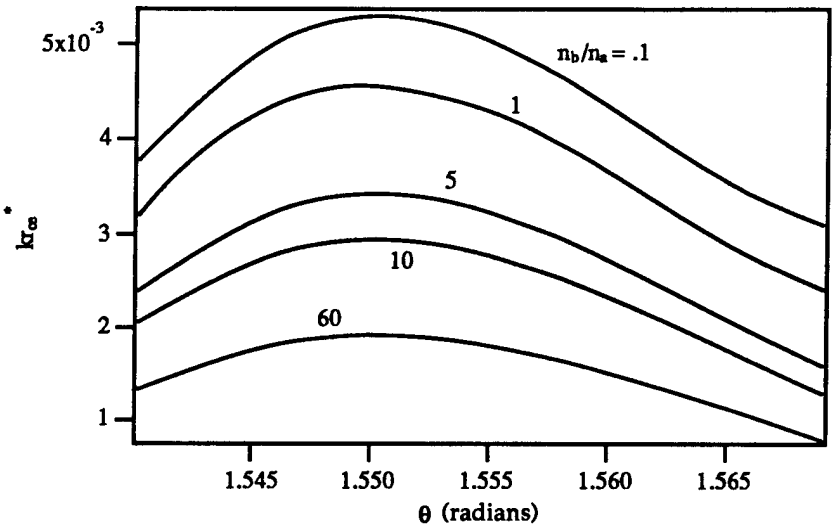

Figure 11: Normalized wavenumber growth-maximized over wavelength as a function of the propagation angle θ with the ratio of beam to ambient densities $n^{(b)}/n^{(a)}$ as a parameter.

parameters during the FO-8 mission (FO-8 is the part of the ATLAS-1 mission that is concerned with CIV tests).

During the FO-8 mission, 100 msec long pulses of xenon gas were performed every five seconds for a period of five minutes. Different types of data were recorded during the releases including optical data, wave data, spacecraft orientation data and Langmuir probe data discussed above. The Langmuir probe current, which is sampled once every 1 msec, is an indicator of the plasma density enhancement that could be caused by CIV. As reported above and in ref. [23], typically an enhancement factor of 60 or more was observed in the Langmuir probe current throughout FO-8, which would correspond to a factor of 60 increase in the local plasma density. A sample of the Langmuir probe data is given in Fig. (1).

We note that the current increases immediately after the valve is opened. The current rises from approximately 1.5 mA to approximately 90 mA within a characteristic time of approximately 25 msec. The current fluctuates about a steady high value for the duration of the release, until the valve is closed, after which, the current drops back to ambient within a few msecs.

The main question here is the cause of this density enhancement. Although wave data showing strong lower hybrid wave emission during the release have

Atomic Mass of Xe	131 a.m.u
First Ionization Pot. of Xe	12.13 eV
CIV of Xe	4.225 km/s
Release Flow Rate	1.1-1.5 mol/s
Release Velocity	61 m/s
Ambient oxygen Ion Density	5×10^4 1cm^3
Ambient Electron Temperature	.1 eV
Geomagnetic Field Strength	.7 G
Xe^+ gyrofrequency	8 Hz
O^+ gyrofrequency	67 Hz
Xe^+ gyrofrequency	8 Hz
$O^+ - Xe$ Elastic Cross-section	10^{-19} m^2
Shuttle Orbital Velocity	7.5 km/s

Table 2: Parameters of ATLAS-1 CIV Tests (FO-8).

been reported by Choueiri et. al. [35] and in section 3.7 above thus hinting to a possible role of CIV (i.e. positive CIV test), we concentrate in this section solely on attempting to explain the density enhancement data. In particular we look at whether it is possible to explain this density enhancement without invoking CIV.

It would be more direct to study the extent to which electron energization by waves and subsequent impact ionization play a role in the ATLAS-1 releases as was attempted in ref. [36]. In order for such an analysis to be realistic it must include details of the wave emission, and saturation using tools from nonlinear plasma physics. We have chosen to bypass the complexity of such an analysis in favor of more realistic computer particle simulations as is reported in section 7 of this report.

In this section we evaluate the role of non-CIV effects in the ATLAS-1 releases looking for insight into whether the density enhancement can be explained without electron energization and rapid ionization. Consistent negative results would not necessarily prove, but would further substantiate the possibility of enhancement by collective ionization.

5.2 Spacecraft Attitude

Any model of the releases must account for the attitude of the spacecraft and the release geometry. Specifically, the orientation of the vectors representing the relative velocity between the ionosphere and the released gas, the geomagnetic field, the spacecraft position, and their magnitude must be known. Of great importance is the pitch angle, which is the angle sustained by the relative velocity

vector and the geomagnetic field vector. The pitch angle plays a direct role in scaling the amount of energy transferred from the relative motion to ionization via electron heating through plasma waves. The relative velocity vector is the sum of the the orbital velocity vector and the gas release velocity vector. Since the latter is small with respect to the former (see Fig. (2)), the relative velocity vector is essentially that of the orbital velocity.

NASA generates values for the geomagnetic field, velocity and position vectors, Euler angles, for each second of the shuttle's orbit. The magnetic field data is generated by a standard geomagnetic model whose accuracy is well above what is required for our analysis. The coordinates of the vectors in the data set are given in the GTOD (Greenwich True of Date) coordinate system, which is fixed with respect to the earth as shown in Fig. (12).

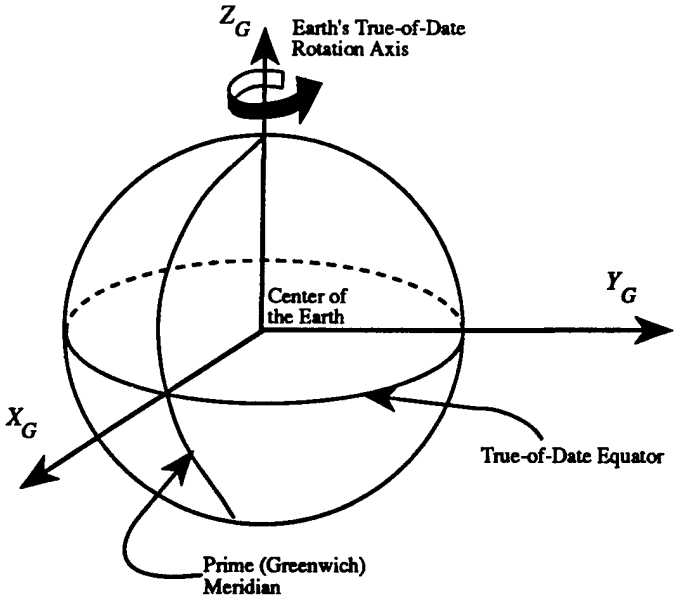

Figure 12: Schematic representation of the standard shuttle body coordinate system. The rotations shown are with respect to the "airplane" mode of the spacecraft. The pitch, roll and yaw angles given by the NASA attitude file are, however, around the axes of the GTOD system.

For the purposes of this investigation, it is necessary to know the coordinates of the vectors in the frame of the stationary shuttle shown in Fig. (13). In order to carry the appropriate transformations and visualize the release geometry starting from the NASA file as input, we have developed a dedicated stand-

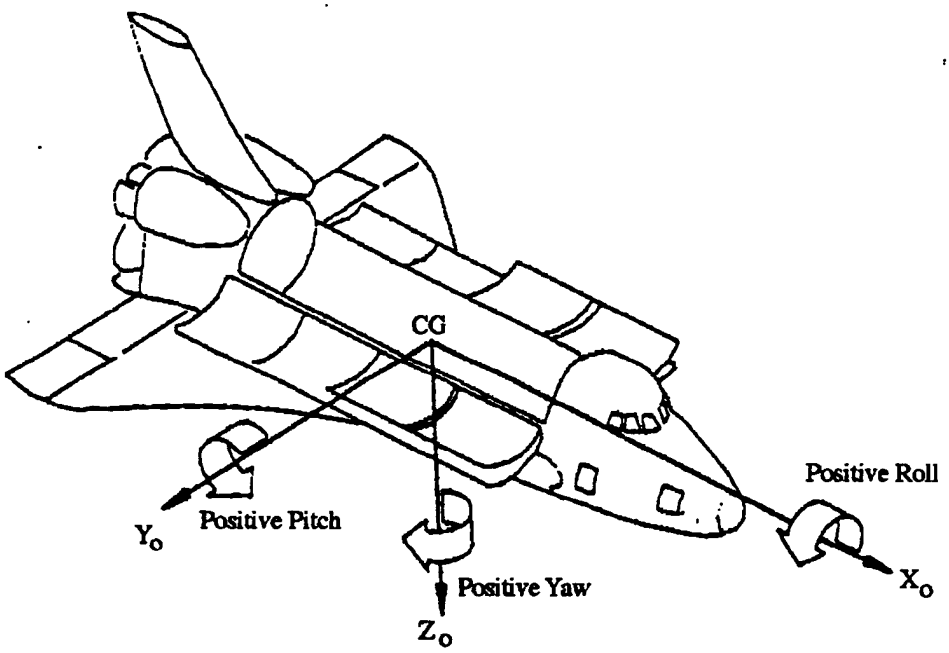

Figure 13: Schematic representation of the Greenwich True-of-Date (GTOD) Coordinate System.

alone software with a graphical interface. The software called ORBIVEC, takes the NASA file for input, calculates all the appropriate transformations and displays in three-dimensional perspective the vectors relevant to the release in a reference frame attached to the shuttle. Also displayed is the pitch angle along with other useful information.

In order to transfer the vectors in the GTOD to the shuttle system a coordinate transformation must be performed, involving a rotation of coordinate systems from the GTOD to the shuttle based system. Since rotations do not commute, it is necessary to determine the order of the rotations. Pitch is a rotation around the GTOD y-axis (positive rotation is given by the right hand rule). The second rotation, yaw, is a rotation around the z-axis of the already once rotated GTOD system. The final rotation, roll, is a rotation around the twice rotated system. These three rotations can be represented by transforma-

tion matrices, which when multiplied in the correct order, will serve as a linear operator, which in turn, when multiplied by a vector in the GTOD system, will give the coordinates in the shuttle system. The transformation of a vector is given by the following

$$Ax = x' \tag{10}$$

and

$$A = R_{x''} Y_{x'} P_y \tag{11}$$

where the primed subscripts correspond to rotations about rotated axes, and the matrices R, Y and P are the rotations for roll, yaw and pitch respectively. The vector x' x corresponds to a vector in the GTOD system, and the vector corresponds to the coordinates of the same vector in the rotated system. The rotation matrices are given by

$$R_{x''} = \begin{bmatrix} 1 & 0 & 0 \\ 0 & \cos\phi & \sin\phi \\ 0 & -\sin\phi & \cos\phi \end{bmatrix}, \tag{12}$$

$$Y_{x'} = \begin{bmatrix} \cos\beta & \sin\beta & 0 \\ -\sin\beta & \cos\beta & 0 \\ 0 & 0 & 1 \end{bmatrix}, \tag{13}$$

$$P_y = \begin{bmatrix} \cos\theta & 0 & -\sin\theta \\ 0 & 1 & 0 \\ \sin\theta & 0 & \cos\theta \end{bmatrix}, \tag{14}$$

where θ, β and ϕ are the pitch, yaw and roll angles respectively. When the above matrices are multiplied together they give the following transformation matrix,

$$A = \begin{bmatrix} \cos\beta\cos\theta & \sin\beta & -\cos\beta\sin\theta \\ -\cos\phi\sin\beta\cos\theta + \sin\phi\sin\theta & \cos\phi\cos\beta & \cos\phi\sin\beta\sin\theta + \sin\phi\cos\theta \\ \sin\phi\sin\beta\cos\theta + \cos\phi\sin\theta & \sin\phi\cos\beta & -\sin\phi\sin\beta\sin\theta + \cos\phi\cos\theta \end{bmatrix}. \tag{15}$$

This matrix, when evaluated with the correct angles and multiplied by a vector in the GTOD coordinate frame, will give the coordinates of the vector in the shuttle based frame. ORBIVEC, however, for visualization reasons, displays the vectors in a frame slightly different than the standard shuttle frame. The y-axis in ORBIVEC points out of the nose, rather than off the right wing. The x-axis points off the right wing, rather than out of the nose. The z-axis, to complete the right handed coordinate system, points directly upwards, rather than downwards. In order to account for this change, a simple modification is required. The sign of each term in the third row of the matrix must be switched to account for the flip in the z-axis. The first and second row must be exchanged

to account for the swapping of the x and y axes. This gives the following final transformation matrix,

$$A = \begin{bmatrix} -\cos\phi\sin\beta\cos\theta + \sin\phi\sin\theta & \cos\phi\cos\beta & \cos\phi\sin\beta\sin\theta + \sin\phi\cos\theta \\ \cos\beta\cos\theta & \sin\beta & -\cos\beta\sin\theta \\ -\sin\phi\sin\beta\cos\theta + \cos\phi\sin\theta & sin\phi\cos\beta & \sin\phi\sin\beta\sin\theta + \cos\phi\cos\theta \end{bmatrix}. \tag{16}$$

Furthermore, it is desirable for the sake of visualization in the ORBIVEC program to change the sign of the velocity and position vectors. Since the NASA data give the coordinates of the position vector beginning at the center of the earth and ending at the center of mass of the orbiter, the vector in the shuttle based system will be pointing into space. Therefore, the operator in Eq. (15) must operate on the negative of the position vector, which would make it point to the center of the earth. Likewise, the velocity vector is directed toward the motion of the spacecraft relative to the background plasma. Since we want to transform to the frame of the shuttle, the above operator must operate on the negative of the velocity vector given in the orbital data set.

The next task of the ORBIVEC program is to calculate the angle of the velocity vector relative to the magnetic field, or pitch angle. The pitch angle, γ is determined by evaluating the scalar product between the magnetic field and the velocity which yields

$$\gamma = \cos^{-1}\left[\frac{V_x B_x + V_y B_y + V_z B_z}{\sqrt{\left(V_x^2 + V_y^2 + V_z^2\right)\left(B_x^2 + B_y^2 + B_z^2\right)}}\right]. \tag{17}$$

Since rotation of vectors preserves lengths and angles, γ should be preserved for the rotation of the coordinate system. Therefore, γ can be evaluated using the input GTOD coordinates.

The output of the ORBIVEC program is shown in Fig. (14), with the orbital vectors normalized, displaying the magnetic field, velocity vector, position vector and pitch angle for release #4. The velocity vector represents the velocity of the moving ionosphere with respect to the orbiter, and the position vector points to the center of the earth.

The figure shows that the neutral gas, ejected vertically upward from the bay of the spacecraft, will interact with the ionospheric plasma above the bay and behind it. If the neutral cloud is swept up by the ionosphere, the cloud will tend to be pushed towards the rear of the spacecraft. The pitch angle is approximately 85 degrees. After examining the output of ORBIVEC over the duration of FO-8b, it was determined that the orbital parameters varied only slightly over the sixty releases, with the pitch angles only varying a few degrees from the first to the last release.

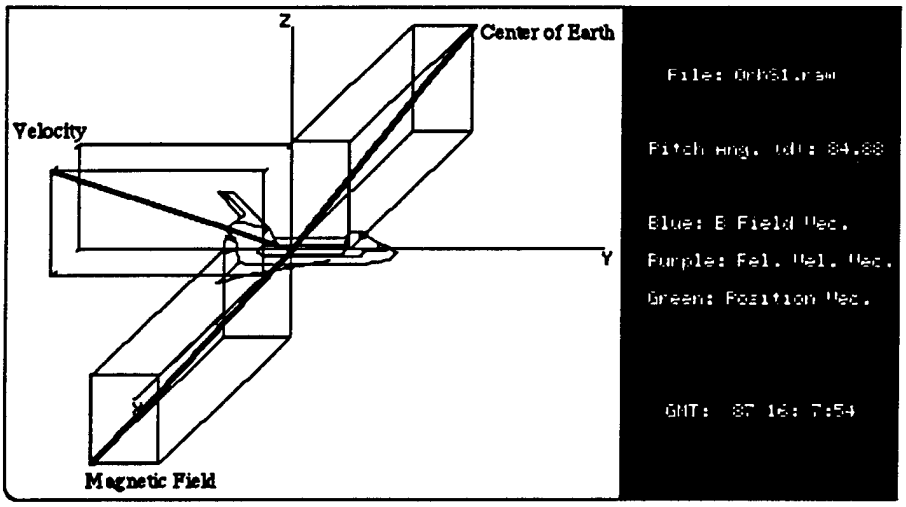

Figure 14: Sample output of ORBIVEC: The normalized coordinates in the shown reference frame of the geomagnetic field vector, the relative velocity vector and the position vector are respectively: $\boldsymbol{B} = (.8403, -.2535, -.4791)$, $\boldsymbol{V} = (.1772, -.8129, -.5548)$ and $\boldsymbol{P} = (-.7855, .2232, .5772)$

.

5.3 Neutral Gas Cloud Density Model

In a SEPAC (Space Experiments with Particle Accelerators) experiment similar to the ATLAS-1 mission, nitrogen gas was ejected from the SPACELAB-1, STS 9 mission in 1983. Sasaki et. al.[1] models the gas release in that experiment as an expanding spherical cone, with constant radial velocity, uniform density at constant radius, and constant half angle. Since the two experiments are very similar, the ATLAS-1 release is modeled in the same way, with a half angle of 40 degrees (Neubert[37]).

In order to calculate the density in the cone we use conservation of particles. If we assume uniform density profiles at constant radius from the spacecraft, the flow rate, I_g of xenon neutrals is given by,

$$I_g = A(r) n_g(r) v_g(r), \tag{18}$$

where variables on the right side correspond respectively to the area of the conical cap, the density at constant radius and the velocity of the gas. We know I_g to be 1.5 mole/s. $A(r)$ is given by

$$A(r) = \int \int_{\Omega} r^2 d(cos\theta) d\phi. \tag{19}$$

Here, ϕ is the azimuthal angle, integrated over 2π and θ is the half angle of the cone. This gives $A(r) = .468\pi r^2$. Taking the release velocity of the gas to be 62 m/s. Therefore, the density profile at a certain radius is,

$$n_g(r) = \frac{I_g}{\Omega r^2 v_g}, \tag{20}$$

or

$$n_g(r) = \frac{10^{22}}{r^2} \quad 1/\mathrm{m}^3. \tag{21}$$

This model states that the gas density at a certain radius is constant with time. This is reasonable because the release is essentially a steady process. The only unsteady aspect is that of the dimension of the cone, which is growing linearly with time.

It is necessary to be careful about the conditions close to the ejection apparatus, at small r. Since the diameter of the gas injection orifice is approximately 5 cm., the minimum r on an ideal cone, at which the gas is released is $r = 3$ cm. Therefore, at the start of the release, $r = 3$ cm. This prevents singularity at $r = 0$. It also provides a value for the initial, and maximum neutral xenon density $n_g(r = 3\mathrm{cm}) = 1.23 \times 10^{25}\, 1/\mathrm{m}^3$

5.4 Release Geometry

Using a Macintosh 3-D rendering application called Aldus 3-D we generated the diagrams in Figs. Figs. (15), (16) and (17) below representing three views of the relative position of the Langmuir Probe, magnetic field vector and the conical cloud formed by the released xenon. The cone half angle is about 40 degrees. The Langmuir probe is mounted 160 cm. starboard of the neutral gas ejection apparatus, and 60 cm. below it.

Note that from Fig. (15) and Fig. (16), the magnetic field line connected to the probe extends toward the xenon cloud. However, Fig. (17) shows that the field line passes by the cone, without intersecting it. The smallest cone half-angle at which the cone intersects the magnetic field is 53.9 degrees.

5.5 Evaluation of Sasaki's Scattering Modeling

A substantial density enhancement was also observed on the STS 9 SPACELAB-1 shuttle mission in 1983 during releases of neutral nitrogen. However, since the critical ionization of nitrogen is approximately 12 km/s, and the orbital velocity of the SPACELAB-1, STS 9 mission was 7.5 km/s, the plasma density enhancement that was observed could not have been caused by the CIV phenomenon. Therefore, Sasaki attempted to predict the density enhancements by modeling scattered ionospheric plasma.

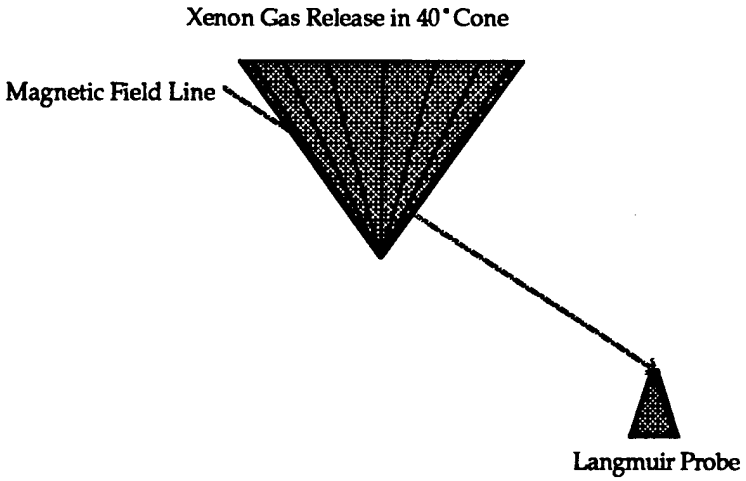

Figure 15: View of release from back of the spacecraft

According to the scattering model of Sasaki[1], the configuration illustrated in our diagrams in Figs. Figs. (15), (16) and (17) should prevent any scattered plasma from diffusing towards the probe. However, since there is some uncertainty in the half angle of the xenon cone, it is still informative to evaluate Sasaki's model by increasing the cone angle until the magnetic field line intersects the cloud.

In order to estimate the density of the scattered plasma that diffuses to the Langmuir probe, Sasaki[1] makes the following assumptions.

1. The scattering of the plasma ions by the gas molecules is isotropic.
2. The scattered plasma diffuses parallel to the magnetic field.
3. Secondary interaction between the scattered ions and the gas molecules is neglected.

The scattering rate of ionospheric plasma from a differential volume ds with unit cross sectional area can be written as

$$dF = F_p n_g(r) \sigma \sin\theta ds/2, \tag{22}$$

where

$$dF = v_{scat} n_p \tag{23}$$

is the scattered plasma flux,

$$F_p = v_{orb} n_o \tag{24}$$

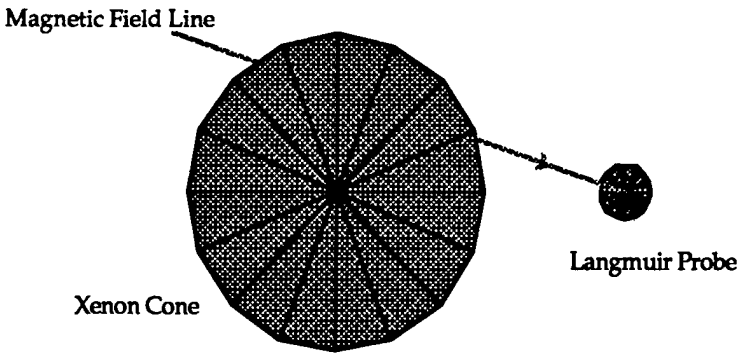

Figure 16: View of release from above the spacecraft

is the ionospheric plasma flux, $n_g(r)$ is the neutral gas density at radius r, σ is the cross section of oxygen-xenon scattering (taken to be[38] $10^{-19}\mathrm{m}^2$), θ is the pitch angle (85 degrees for our case), n_p is the density of scattered plasma, n_o is the density of ambient plasma ($5 \times 10^{10} 1/\mathrm{m}^3$ for our case), v_{orb} is the shuttle orbital velocity (7.5 km/s) and (v_{scat} is the velocity of scattered ions.

The plasma density measured at the probe is then obtained by integrating the above expression along the magnetic field line intersecting the neutral gas cloud,

$$n_p = \int n_o \frac{v_{orb}}{v_{scat}} \sin\left(\frac{\theta}{2}\right) \sigma n_g(r)\, ds. \tag{25}$$

The above expression was evaluated for the the ATLAS-1 releases by varying the cone angle of the xenon cloud, and the scattering velocity of the ambient ions. These two parameters are the only two in this problem which have a significant amount of uncertainty. Much insight into the physical accuracy of this model can be obtained by varying these two parameters so that the model produces the experimental results. The degree to which the varied values of these parameters correspond to the actual physical nature of the problem will determine the applicability of the model. If these parameters must be stretched significantly beyond their actual physical value in order to reproduce the experimental results, then the model is inapplicable. Fig. (18) shows the results from an evaluation of Sasaki's model, where the cone angle and scattered velocity were varied until the density, n_p agreed with the factor of 60 increase recorded by the Langmuir probe.

Fig. (18) shows the results from an evaluation of Sasaki's model, where the cone angle and scattered velocity were varied until the density, n_p agreed with the factor of 60 increase recorded by the Langmuir probe.

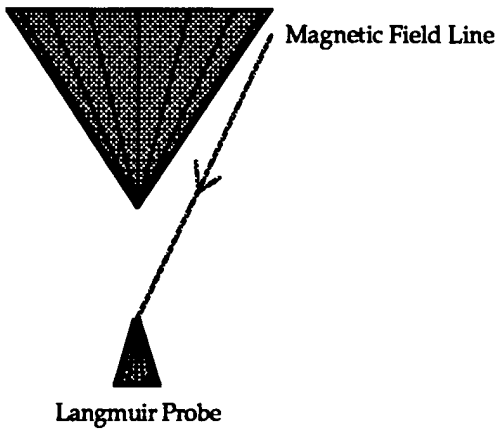

Figure 17: View of release from right wing the spacecraft

The following arguments must be kept in mind while evaluating Sasaki's model for our case. When in the STS-9 releases, the ionospheric plasma collides with released nitrogen, the oxygen ions will impart some momentum to the nitrogen particles. In a single binary collision, because of the comparable molecular weights of oxygen and nitrogen, both particles will scatter in the frame of the spacecraft, with velocities lower than the orbital speed. Therefore, the oxygen ions will lose momentum in the frame of the spacecraft, and thus are more easily magnetized by the geomagnetic field (Sasaki's model assumes that the scattered ions are completely magnetized). Once scattered off of the nitrogen cloud, the ions will travel in a tightly woven orbit along the magnetic field lines. However, when xenon is ejected into the ionosphere as is the case with the ATLAS-1 releases, there should be significant differences. The high molecular weight ratio between xenon and oxygen will cause the xenon cloud to act as a solid wall. The ionospheric plasma will collide off of this wall and impart essentially no momentum to the xenon atoms. In an elastic collision, this will cause the oxygen ions to scatter isotropically with scattering velocities approximately equal to the orbital velocity. This effect will eliminate Sasaki's assumption of completely magnetized ions.

In order for scattered ions to be magnetized, the Larmor radius must be much smaller than the characteristic dimension of the experiment (which for this case, is the dimension of the cloud, and is approximately 1 meter). A characteristic velocity of 3750 m/s (half the orbital velocity) gives a Larmor radius of 8.89 meters, which is larger than the entire experimental apparatus.

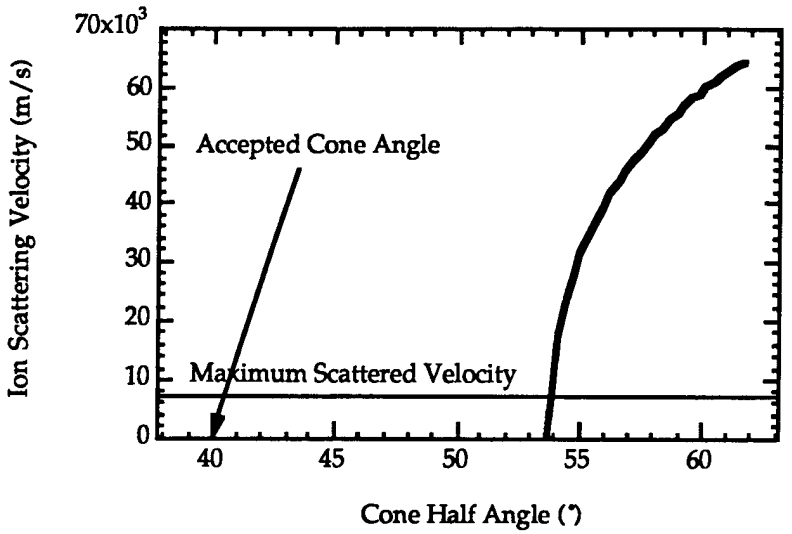

Figure 18: Application of Sasaki's scattering model[1] to reproduce the factor of 60 plasma density enhancement observed on ATLAS-1. Both the cone angle and the scattered velocity were varied.

Therefore, for the ATLAS-1 releases, significant diffusion across the magnetic field lines will occur on the time scales we are interested in, thus devaluating Sasaki's second assumption.

Fig. (18) demonstrates the failure of the model. For the model to reproduce the experimental results, the varied parameters, cone half angle and scattering velocity, had to be extended beyond their physical limits. The figure shows that the model predicts no plasma density enhancement until the cone angle reaches approximately 54 degrees, which is over 10 degrees more than the accepted value. In addition, the calculated scattering velocities are, on the whole, much larger than the maximum scattering velocity of 7.5 km/s. This overestimation reflects the aforementioned inaccuracies of Sasaki's model for our case. If the model assumes complete magnetization of the oxygen ions scattering off of the xenon cloud, the model will greatly overestimate the plasma flux measured at the probe. Since the model sums up contributions to the scattered flux, $n_{sact}v_{sact}$, and the model attempts to reproduce the experimental n_{sact} value of $3.0\times10^{12}1/\mathrm{m}3$ by varying the scattered velocity, an overestimate in the scattered flux will appear as an overestimate in the scattered velocity. Fig. (18) shows that for only a small range of cone angles (53.78-54 degrees) does the scattered velocity fall below the maximum velocity of 7.5 km/s. At cone angles larger than

54 degrees, the required scattering velocity rises sharply to unphysical values.

Another effect that devaluates Sasaki's model for the ATLAS-1 releases is the a measure of the penetration of the oxygen ions into the Xe cloud which is given by the mean free path for elastic collisions, $1/n_{Xe}\sigma_{elast.}$. For the ATLAS-1 releases, the value of the mean free path is only on the order of a few millimeters. If we assume that each oxygen ion collides at most twice with a xenon atom, its penetration would only on the order of two mean free paths. Sasaki's model, however, integrates along the magnetic field line throughout the entire cone, thus neglecting any mean free path effects. This will further overestimate the scattered plasma flux measured at the probe.

Therefore, it is very unlikely that the plasma density enhancement, measured by the ATLAS-1 Langmuir probe can be solely attributed to the model proposed by Sasaki. Even if the actual cone angle is within the small range shown in Fig. (18), further improvements to Sasaki's model including finite Larmor radius effects and mean free path effects should be made. The following sections describe such an improved scattering model and evaluates it for the ATLAS-1 releases.

5.6 Improved Scattering Model

In reality, the scattered ions in the ATLAS-1 experiment will not be completely magnetized, and will not diffuse strictly along the magnetic field lines. Instead, each scattered ion will collide off the Xenon cloud and travel in a randomly chosen trajectory on the solid angle with a speed of 7.5 km/s in the frame of the spacecraft. It will then travel in a helical orbit with a Larmor radius larger than the characteristic dimension of the experiment. Fig. (19) is a schematic representation of the improved scattering model, clearly showing the finite Larmor radius, and the triangular flux tube to be described later.

The improved model will behave as a median between the magnetized scattering model proposed by Sasaki, and purely isotropic scattering which would occur in the absence of a magnetic field. Therefore, we should expect the model which incorporates these orbits to produce density enhancement significantly smaller than those calculated by Sasaki's model. Fig. (20) shows a flow chart that illustrates the basic components of the model.

Instead of integrating along the magnetic field line as Sasaki does, we integrate over the interaction region by dividing the xenon cone into discrete volume elements. This will account for collisions that do not occur on the magnetic field lines, and will allow the model to incorporate mean free path effects. The discrete spherical coordinates of the cone are

$$r = R\frac{i+.5}{L}, \quad 0 \le i \le L-1, \tag{26}$$

$$\phi = \Phi\frac{j+.5}{M}, \quad 0 \le j \le M-1, \tag{27}$$

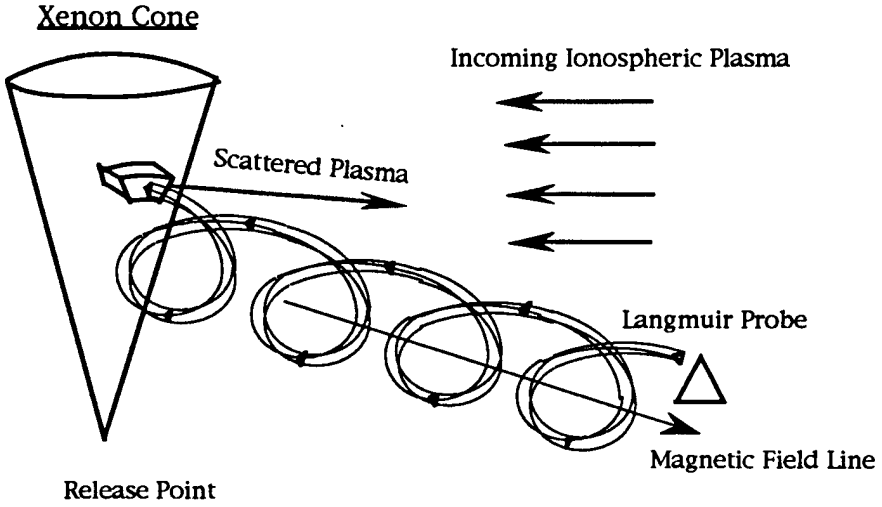

Figure 19: Schematic representation of improved scattering model for the ATLAS-1 releases.

$$\theta = 2\pi\frac{k+.5}{N}, \quad 0 \le k \le N-1, \tag{28}$$

where R is the radial extent of the cone given by $R = v_g t$ and Φ is the cone half-angle and is taken to be 40 degrees. The constants L, M and N are the number of cells in the three coordinate directions. We will refer to these three coordinates as the radial, altitudinal and azimuthal coordinates.

If we assume that the scattering from a differential volume element is isotropic, we can estimate the density of scattered ions on the surface of the volume element by the following process. The number of scattered ions per unit time from a differential volume element is

$$\dot{N} = \sigma_{elast} n_{O^+} n_{Xe} v_{rel} dV, \tag{29}$$

where σ_{elast} is the $O^+ - Xe$ elastic cross-section, n_{O^+} and n_{Xe} are the densities of ambient oxygen and neutral xenon respectively, $v_{rel.}$ is the relative velocity (orbital velocity) and dV is the differential volume element.

By conservation of particles, we can set the above relation equal to the total flow rate of scattered ions out of the volume element,

$$\dot{N} = n_{scat} v_{rel} dS, \tag{30}$$

where dS is the differential surface element. The above yields,

$$n_{scat} = \frac{dV \sigma_{elast} n_{O^+} n_{Xe}(r)}{dS}. \tag{31}$$

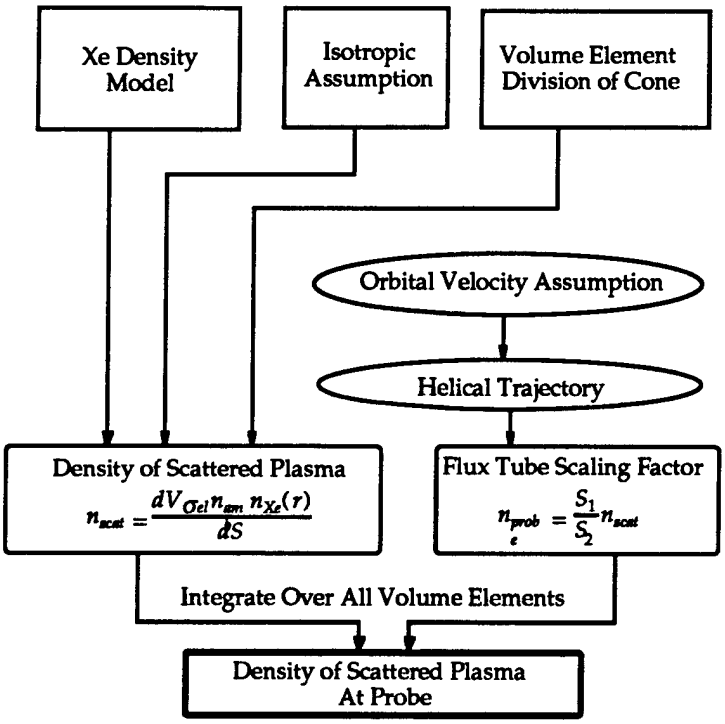

Figure 20: Flow chart illustrating the interaction between the basic components of the model.

Note that this value is independent of the scattering velocity. This is due to the assumption that the scattering velocity will equal the relative velocity, and their effects cancel each other out. If we did not assume that the xenon cone behaves like a wall, then the value of the scattered density would not be independent of either the orbital or scattered velocity.

Once the value of the scattered density at the cell is obtained, we must relate it to the actual density measured at the probe. This can be accomplished by modeling the expansion nature of isotropic scattering in conjunction with the dynamics of the individual scattered ions. Simulating this effect is the essence of the accuracy of this improved model compared to that of Sasaki, because it quantifies the effect of the partial magnetization, rather than assuming it away by only looking at the completely magnetized limiting case.

The expansion nature of the isotropic scattering is modeled by assuming that all of the scattered ions come from a point source. In the absence of a magnetic field, this would accurately simulate isotropic scattering. If the scattered ions travel in straight line paths from the point source at a constant velocity, the density at a distance r, would simply scale with the spherical area, or

$$\frac{n_2}{n_1} = \left(\frac{r_1}{r_2}\right)^2. \tag{32}$$

The geomagnetic field will alter this value, creating a dependence on trajectory.

If a unique trajectory connecting each cell point with the Langmuir probe can be obtained, then the problem can be solved completely. First, assume that we know this trajectory. Then, march along it from the center of the cell to the edge of the cell, where the scattered density has been calculated from the above relation. We can then arbitrarily choose three points in a plane perpendicular to the velocity vector at this point, and coplanar with this point. These three points define a flux tube, which will be used to calculate the scaling of the density from the cells to the probe. Then, if we can calculate the exact trajectory of these three points connecting to the center of the cell (remember that we are considering the scattering as coming from a point source), we can follow this flux tube throughout space. This flux tube will be of triangular cross-section, with its source as a point in the particular cell. It will be expanding due to the spherical expansion mentioned above, and it will be rotating due to the slight magnetization. At the moment that the original trajectory hits the probe, the area subtended by the three particles will give the density at the probe,

$$n_{probe} = \frac{A_1}{A_2} n_{scat}. \tag{33}$$

This was determined by conservation of particles in a flux tube, where the velocity cancels out because it is assumed to be constant. The values, A_1 and A_2 are the triangular areas at the edge of the cell, and the probe respectively. This determines the contribution of the density enhancement at the probe, due to scattering from a single point source in the xenon cone. In order to determine the total density enhancement, we must sum up the contributions from each cell in the cone where the ionospheric plasma penetrates. If we then increase the number of cells to infinity, the density value should converge to a single number, which would represent a continuous limit of the discretization of the problem. What remains to be done is to determine if this unique trajectory exists, and how to find it.

5.7 Derivation of Helical Trajectory

A moving charged particle in a magnetic field will be subject to the Lorentz force,

$$\boldsymbol{F}_L = q\boldsymbol{v} \times \boldsymbol{B}. \tag{34}$$

A general solution to the position of a particle in this force field is a helix, with position,

$$\boldsymbol{r} = \hat{q}_1 \left[r_L \cos\left(\omega_c t + \delta\right) + c_1\right] + \hat{q}_2 \left[r_L \sin\left(\omega_c t + \delta\right) + c_2\right] + \hat{q}_3 \left(v_\parallel t + c_3\right). \quad (35)$$

This is the most general solution because it allows the axis to be pointing in any direction. The tensor, q_{ij} represents a rotation of coordinate systems from one in which the helix axis is in the z-direction, to any other rotated coordinate system. This rotation matrix can be obtained by knowing the components of the magnetic field (which is the direction of $\hat{q}_3$), and calculating an orthogonal basis. The constants, c_1, c_2, and c_3 are translation constants, and can be determined from the initial conditions. The value, δ corresponds to a constant phase shift which will also be determined later. ω_c is the ion Larmor frequency ($\omega_c \equiv qB/m$) in rads/sec. Finally, r_L and $v_\parallel$ correspond to the Larmor radius and the parallel component of the velocity respectively.

In order to calculate the parameters necessary for determining a unique helical trajectory, we must first look at the geometrical characteristics of a helix. If two points fall on a helix they must be equidistant from an axis. Since we are looking at trajectories induced by a magnetic field, this axis is oriented with the geomagnetic field.

If we orient a coordinate system so that the origin is placed at the Langmuir probe, and the z-axis is oriented with the geomagnetic field, then the coordinates, p_1, p_2 and p_3 are the coordinates of a cell in the xenon cone. So, the initial coordinates of the two points on the helix are,

$$q = \{0, 0, 0\} \qquad \text{and} \qquad p = \{p_1, p_2, p_3\}. \quad (36)$$

If we assume that the equation of the line for an arbitrary axis, oriented parallel to the magnetic field is given by,

$$\boldsymbol{x} = \boldsymbol{x}_o + \boldsymbol{A}t \quad (37)$$

where,

$$\boldsymbol{x}_O = \{x_o, y_o, 0\}, \qquad \boldsymbol{A} = \{0, 0, 1\}. \quad (38)$$

The perpendicular distances to the axis from the origin and the point P are respectively,

$$d_1 = \sqrt{x_o^2 + y_o^2}, \qquad d_2 = \left[(p_1 - x_o)^2 + (p_2 - y_o)^2\right]^{1/2}. \quad (39)$$

From charged particle dynamics, these values are equal to the Larmor radius, r_L,

$$r_L = \frac{m_i v_\perp}{qB}. \quad (40)$$

Setting the two distances equal and solving for y_o gives,

$$y_o = \frac{p_1^2 + p_2^2 - 2x_0 p_1}{2p_2}. \quad (41)$$

This relation implies that the locus of axes of helices on which two fixed points lie is a straight line.

By solving the equations of motion for a charged particle in a magnetic field, the following general solution for the trajectory in the aforementioned coordinate system is determined,

$$\boldsymbol{r}(t) = \hat{\boldsymbol{x}}\left[r_L \cos\left(\omega_c t + \delta\right) + c_1\right] + \hat{\boldsymbol{y}}\left[r_L \sin\left(\omega_c t + \delta\right) + c_2\right] + \hat{\boldsymbol{z}}\left(v_\parallel t + c_3\right) \quad (42)$$

where,

$$\omega_c = \frac{qB}{m}, \qquad v_\perp^2 + v_\parallel^2 = V_{orb}^2, \qquad v_\perp = r_L \omega_c, \quad (43)$$

and δ and the constants c_i are arbitrary. If we assume that $\boldsymbol{r}(0) = \{0, 0, 0\}$, the constants c_i are determined and the trajectory is given by the following,

$$\boldsymbol{r}(t) = \hat{\boldsymbol{x}}\left[r_L \cos\left(\omega_c t + \delta\right) - r_l \cos\delta\right] + \hat{\boldsymbol{y}}\left[r_L \sin\left(\omega_c t + \delta\right) - r_L \sin\delta\right] + \hat{\boldsymbol{z}}\left(v_\parallel t\right). \quad (44)$$

Next, in order to correctly set the end boundary condition, we must shift the coordinate system so that the origin now lies on the helix axis. The coordinates of the two endpoints now become

$$q' = \{-x_o, -y_o, 0\} \qquad \text{and} \qquad p' = \{p_1 - x_o, p_2 - y_o, p_3\}. \quad (45)$$

The parameter δ corresponds to the angle between the x-axis in the present coordinate system, and the the line connecting the origin to the point q'. This gives the following relations for δ,

$$-x_o = r_L \cos\delta, \qquad -y_o = r_L \sin\delta. \quad (46)$$

We can close the system by considering the boundary condition when the particle reaches the point p'. This occurs when $v_\parallel t_{end} = p_3$. Noting that the particle must also be at the correct p_2 and p_1, the following relations must hold,

$$x\left(t_{end}\right) = p_1 = r_L \cos\left(\omega_c t_{end} + \delta\right) - r_L \cos\delta, \quad (47)$$

$$y\left(t_{end}\right) = p_2 = r_L \sin\left(\omega_c t_{end} + \delta\right) - r_L \sin\delta. \quad (48)$$

Combining all of the above relations gives the following system of six equations and six unknowns,

$$V = \sqrt{v_\parallel^2 + v_\perp^2} \quad (49)$$

$$r_L \sin\left[\frac{qBp_3}{mv_\parallel} + \delta\right] = p_2 - y_o \qquad \text{or} \qquad r_L \cos\left[\frac{qBp_3}{mv_\parallel} + \delta\right] = p_1 - x_o \quad (50)$$

$$y_o = \frac{p_1^2 + p_2^2 - 2x_0 p_1}{2p_2} \quad (51)$$

$$r_L = \frac{m_i v_\perp}{qB} \quad (52)$$

$$r_L = \sqrt{x_o^2 + y_o^2} \tag{53}$$

$$-x_o = r_L \cos\delta, \qquad \text{or} \qquad -y_o = r_L \sin\delta, \tag{54}$$

where the unknowns are $r_L, v_\parallel, v_\perp, x_o, y_o$ and δ. Solving for these unknowns will completely specify the unique trajectory between two specified points.

This system is difficult to solve analytically, consequently a numerical solver was especially developed to solve it.

The final crucial element of this model is the incorporation of the mean free path effects. This is accomplished by calculating the distance from each point to the edge of the cone along the velocity vector. If this distance is greater than two mean free paths, the cell is not included in the calculation. The mean free path increases with increasing distance from the xenon ejector, so a higher percentage of the cone will be included in the calculation with higher r.

5.8 Limitations of the Improved Scattering Model

Throughout the evaluation of the models proposed to reproduce the plasma density enhancement in the ATLAS-1 releases, a major effect has been neglected, namely, that of the wake. As can be seen from Fig. (21), the xenon gas releases were ejected straight out of the top of the shuttle bay into the wake of the spacecraft.

In reality, there will be significant separation of the ionosphere off of the nose of the shuttle, thus creating recirculation in the shuttle bay area. Throughout the investigation, we have been assuming that the relative velocity is unhindered, which may not be true in general. If the separation, D_{min} is as large as a meter, there will be, to a first approximation, no relative motion of xenon and O^+ until t=16 msec. When looking at the Langmuir probe data at this time scale as shown in Fig. (22), we see significant plasma density enhancement within one or two msecs of the release and a factor of 30 enhancement before t=16 msec. This effect requires further investigation in order to determine whether it will somewhat impact the results of the scattering model. Furthermore, the scattering model neglects a significant dynamical effect, that of the drift velocity. This drift velocity, given by

$$\boldsymbol{v}_d = \frac{\boldsymbol{E} \times \boldsymbol{B}}{B^2} = \frac{(\boldsymbol{u} \times \boldsymbol{B}) \times \boldsymbol{B}}{B^2} \simeq \boldsymbol{v}_{orb}, \tag{55}$$

is caused by the moving magnetic field in the frame of the spacecraft. In the frame of the stationary ionosphere, the trajectories of the scattered ions will be purely helical. In the frame of the moving spacecraft, however, the drift velocity will give the ions a velocity component on the order of the orbital velocity in a direction pointing towards the back of the shuttle. This effect will alter the trajectories of the scattered ions, as they will by cycloidal rather than helical. Although we believe that including the above two effects will not alter the conclusions of this study we recommend that they be evaluated in the future.

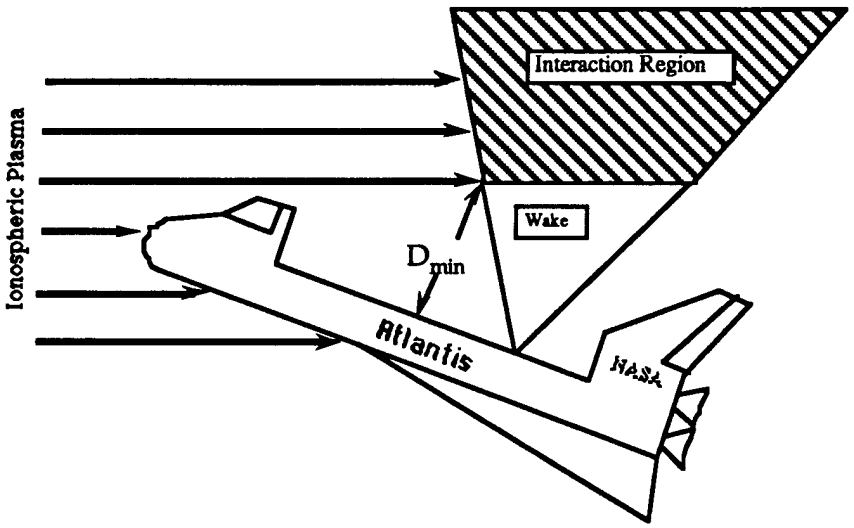

Figure 21: Schematic of wake effect during the ATLAS-1 releases showing separation of ionospheric plasma off the nose of the shuttle.

5.9 Results from the Improved Scattering Model

Fig. (23) shows the output of the computer code which performs the calculation at $t = 16$ msec at different cell sizes. It represents the plasma density that will be measured at the Langmuir probe caused only by magnetized scattering. It is plotted versus the number of cell divisions to test for convergence. The time $t = 16$ msec was chosen for convenience (it occurs when the radius of the cone is 1 m.) and for reasonable calculation time (the calculation time scales with the cube of the number of cells). At this stage, there are three degrees of freedom to vary, which are the three different independent discretization factors. The cone is divided by radius, azimuthal angle, and altitudinal angle. The model was run with equal radial and azimuthal cell sizes, but with a very large number of altitudinal cells. This is due to the fact that the mean free path is only on the order of millimeters. The altitudinal angle can be considered as a spherical analog to the distance from the edge of the cone to the cell. Therefore, the fineness of the altitudinal discretization must be very high on the scale of the mean free path if numerical precision is desired, and since the mean free path is much smaller than the dimension of the cone, the altitudinal number of cells must be much larger than the radial and azimuthal numbers.

The output curves are not smooth throughout. This is due to the fact

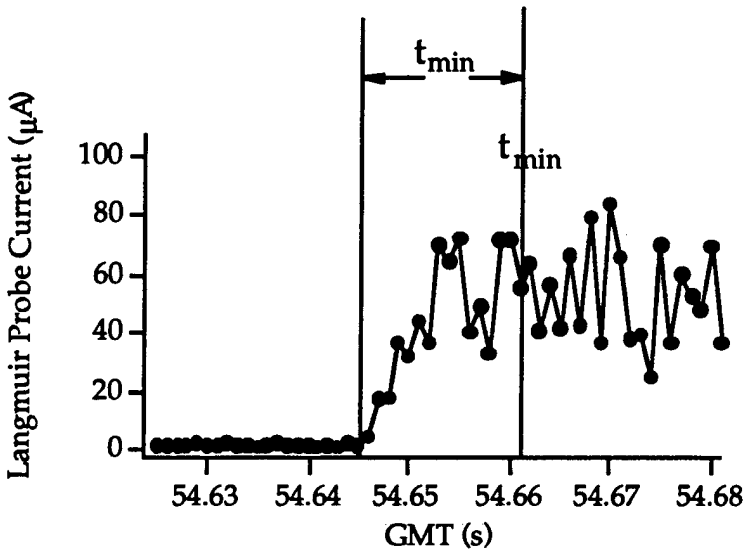

Figure 22: ATLAS-1 Langmuir probe data expanded to show details of probe signal rise time.

that at certain cells, the numerical solution of the trajectory fails, and the contribution from that cell is neglected. This happens only infrequently, and does not significantly alter the outcome of the model.

In order to compare the output of the model with the experiment, the ambient plasma density of $5 \times 10^{10} 1/m^3$ was added to the output. This is due to the fact that the density at the probe will be the ambient plus any enhancement. Fig. (24) shows the same calculated data shown in Fig. (23), but scaled with the values of the ambient and experimental plasma density at $t = 16$ msec.

5.10 Discussion and Conclusions

The model demonstrates good behavior as the number of cells is increased. The numerical inaccuracy is apparent at low altitudinal cell numbers, but levels off to a good convergence as this number is increased. The model does not show clear convergence with increasing azimuthal and radial precision at the cell sizes used. However, we believe that the model will converge before it increases to any significant value greater than the ambient. When the output of the model is

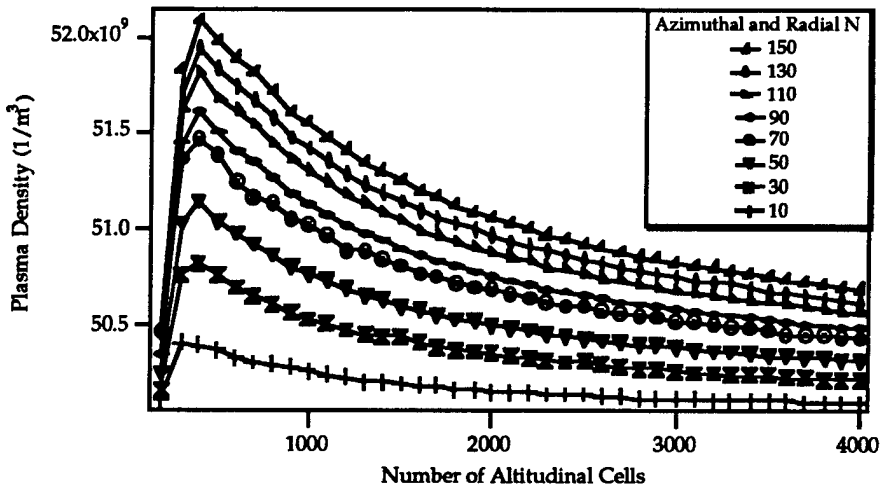

Figure 23: Results of numerical calculations using the improved scattering model.

compared with the actual experimental value, there is no discernible difference between the ambient density and the enhanced density predicted by the model. The ticks in the plot of Fig. (24) are the data points from Fig. (23), and essentially are equal to the ambient density when compared to the experimental value of the density enhancement at $t = 16$ msec. Therefore, the scattering mechanism simulated by the code can in no way be responsible for the plasma density recorded aboard the ATLAS-1 mission. The role of ionization mechanisms, such as CIV, are then more likely to have played a significant role.

6 CIV Experiments on APEX

6.1 General Description of the APEX Releases

APEX (Active Plasma Experiment in Space) is a project of the Institute of Terrestrial Magnetism Ionosphere and Radio Wave Propagation (IZMIRAN) in Russia. The APEX satellite was launched on December 18 1992 and consists an extensive battery of plasma diagnostics and a sub-satellite.

We have conducted a series of neutral gas releases from APEX. During these experiments we staged releases of neutral xenon at different altitudes (between

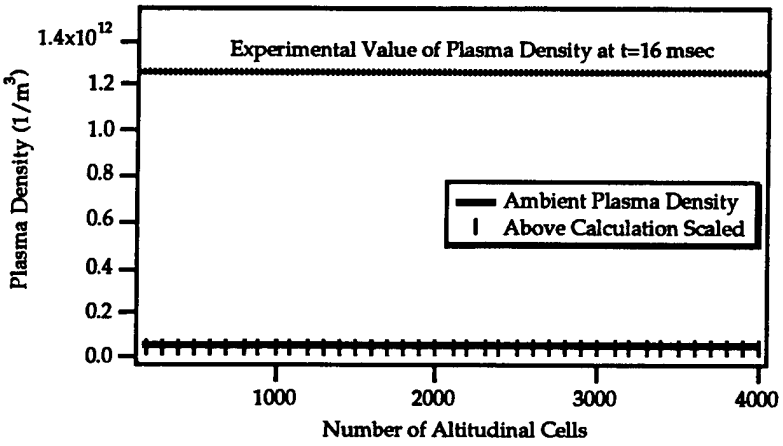

Figure 24: Results of numerical calculations scaled to actual experimental value.

400 and 3000 km) setting up a supracritical relative motion between the injected cloud and the ambient plasma as was done on ATLAS-1. Unlike the ATLAS-1 releases, many of the experimental conditions for the releases (magnitude of the geomagnetic field, release pitch angle, background density, etc..) can be varied widely due to the polar orbit of the spacecraft. Moreover, unlike ATLAS-1, the orbiting APEX satellite provided a longer time (months) for conducting experiments. The most outstanding disadvantage of the APEX releases with respect to their counterparts on ATLAS-1 is the low mass flow rate of xenon. Since all of the hardware on APEX was designed and flight-qualified before the decision to conduct CIV tests was made, we could not increase the mass flow rate above the rated 3 mg/s which is three orders of magnitude lower than the mass flow rate of the ATLAS-1 releases. Furthermore, unlike the ATLAS-1 releases that lasted 100 msec each, the APEX releases lasted a time on the order of minutes.

A picture of the APEX satellite is shown in Fig. (25). The xenon releases were made through a stationary plasma thruster (SPT) operating in a no-discharge mode. The SPT was placed on top of the satellite body with the thruster axis at 45 degrees with respect to the satellite's vertical axis.

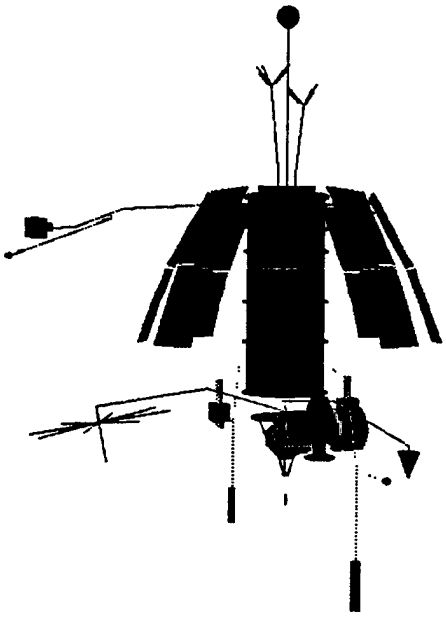

Figure 25: Schematic of the APEX Satellite. The height, excluding the antenna is 2 meters.

6.2 Onboard Diagnostics

A charged particle analyzer was used to measure the energy and pitch angle distribution of electrons and ions with energies between 30 eV and 30 keV. The instrument has 12 directions of view. A complete spectrum is measured in one second.

An electron flux analyzer, intended for satellite potential measurements was used to measure the flux of precipitating electrons with energies ranging between 5 and 1000 eV. Langmuir probes and retarding potential analyzers were used to measure ambient plasma parameters with T_e between .1 and 10 eV.

A radio-frequency ion composition analyzer was also available (1-60 a.u.m.). The LF wave diagnostics permitted the measurement of three components of the electric field up to 700 mV/m with a frequency range of $.01 - 22$ kHz and a sensitivity of 2×10^{-7}-2×10^{-8} V/m/$\sqrt{\text{Hz}}$. The LF wave unit was supposed to measure three components of the magnetic field in the frequency range of .1 –

22 kHz with a sensitivity of 4×10^{-6} nT/$\sqrt{\text{Hz}}$ but unfortunately failed prior to the CIV tests.

The HF wave unit allowed the measurement of one component of the electric field and magnetic fields between .1 and 10 MHz. Data from the onboard scanning spectrometer and the photometer were recorded for the portion of the tests conducted in darkness.

The dc magnetic field is measured with a 3-axis fluxgate magnetometer with a dynamic range of ±6400 nT. Data from another 3-axis service magnetometer, which is part of the attitude control system, were also available as part of the scientific telemetry stream.

6.3 Observations

6.3.1 APEXVIEW Software

A considerable effort was invested at EPPDyL in the development of a stand-alone menu-driven and interactive code for the decoding, reduction and visualization of the data from the various scientific instruments starting from the raw binary-coded telemetry stream. The software, called APEXVIEW, prompts the user for either a span of telemetry frames, or more practically a span of time in GMT and creates a series of multi-labeled color plots showing the calibrated outputs of tens of instrument channels in dimensional form. The software took more than 300 hours of development time and is currently being used by other investigators at IZMIRAN. The software can be easily adapted to process data from other satellites, especially those using the Russian Intercosmos telemetry format.

Since the calibration and data reduction associated with each instrument is known only to the principle investigator responsible for that particular instrument, the task of developing a software that can handle various instruments required many meetings with various instrument PI's. During these meetings conducted during the past two years at IZMIRAN and IKI (Institute of Space Research, Moscow), many scientists spent generously of their time explaining to one of us (EYC) the various recipes for data decoding, calibration and processing that are peculiar to their intsruments. We would like to acknowledge the invaluable help of the following people whose generous instructions made the development of APEXVIEW possible: Dr. V. Afonin (of IKI) for the plasma parameter instruments, Dr. S. Pulinets (of IZMIRAN) for the wide band HF electromagnetic spectra, Dr. V. Chmyrev (of IZMIRAN) for the LF electric and magnetic field spectra, Dr. L. Tyumina (of IZMIRAN) for the DC magnetometer, Dr. M. Pivovarov (of IKI) for the solar sensor and attitude data, Dr. D. Moslov (of IKI) for the service magnetometer, and mostly to Dr. V. Dokukin (of IZMIRAN) for the plasma gun. Dr. Dokukin, who is a co-investigator on this project, arranged and coordinated all these meetings.

6.3.2 Sample Instrument Data

A sample output of APEXVIEW is shown in Fig. (26). The three top panels show the output of the B_x, B_y and B_z channels of the 3-axis DC magnetometer data recorded during the CIV test conducted during orbit number 419. These components are in a reference frame attached to the body of the satellite. The bottom panel shows the masured magnitude of the magnetic field.

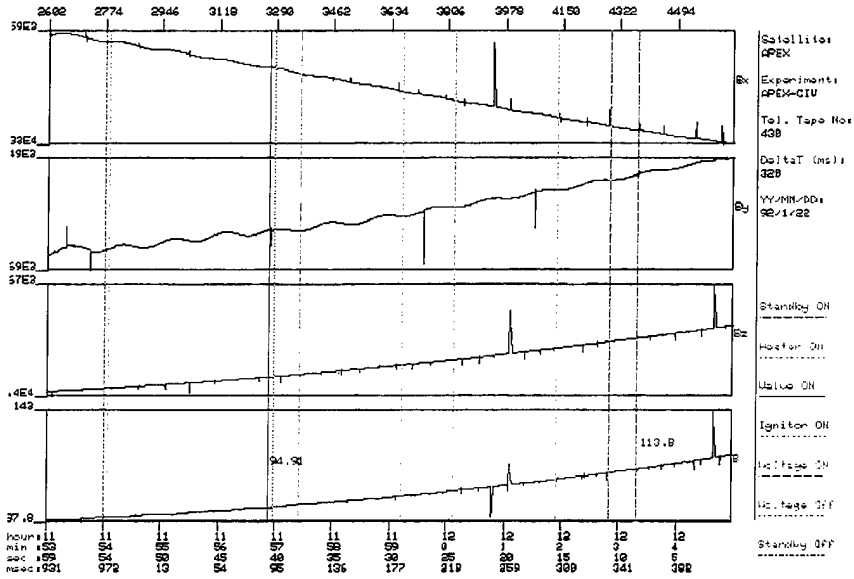

Figure 26: Output of APEXVIEW for 3-axis DC magnetometer data recorded during the CIV test conducted during orbit number 419.

The DC Magnetometer data are of great importance for the CIV tests since, when combined with attitude data from the solar sensor, an orbital dynamic model, a geomagnetic field model and a solar vector model, allow an estimation of the pitch angle of the release (i.e. angle between the velocity vector and the geomagnetic field.) APEXVIEW calculates the pitch angle and the user can display it on any plot by activating a menu command and clicking on any point in the plot.

For the case of this particular release, two pitch angles, 94.9 and 113.8 degrees, are marked for times corresponding to the beginning of the release (about 11:57:10 GMT) and its end (about 12:03:40 GMT).

On each plot the user can mark the events associated with the operation of the SPT used as a source of the released gas. These are shown as a series of

vertical color-coded lines across all the panels of the plot. Starting from the left these lines are:

1. A dashed blue line marking the "Standby On" event when all the SPT subsystems are put on standby

2. A dashed purple line marking the "Heater On" event when the heater to the hollow cathode of the SPT is turned on in preparation to operating the device. The cathode is typically given more than 3 minutes to heat before striking a discharge in the SPT[8].

3. A dashed light blue line marking the "Ignitor On" event when the cathode ignitor is switched on allowing the cathode to emit electrons. In all CIV tests, the ignitor was not operated, even though the plots display the "Ignitor On" event marker.

4. A green solid line marking the "Valve On" event when the actual flow of xenon starts. *This is the line that marks the actual start of the CIV releases.*

5. Brown dashed lines marking the "Voltage On" and "Voltage Off" events when the SPT discharge is either on or off. In all the CIV tests the SPT was operated in a no-discharge mode. This was achieved by not turning the cathode ignitor on. Although the voltage was applied, no discharge current was drawn between the cathode and the anode in the SPT.

6. A final dashed blue line marking the "Standby Off" event when all the SPT subsystems are turned off simultaneously. In particular, the xenon valve is also shut off at this time.

Based on the above description, the only events we need to concern ourselves with in the context of the CIV tests are the "Valve On" and the "Standby Off" events, i.e. the solid green line and the final dashed blue line which mark the beginning and end of the release respectively.

6.4 High Frequency Wideband Data

We have processed many megabytes of telemetry data from various instruments described above looking for signatures that can be attributed to the xenon releases. Unlike the case of ATLAS-1, there were no strong and unequivocal manifestation of the APEX releases in the recorded data with the exception of the HF Wideband data described below. This can most likely be attributed to the far lower mass flow rate of the APEX releases for which, even if a beam

[8]Of course, no discharge was initiated during the CIV tests which required a neutral flow of xenon.

instability is created, the resulting initial turbulence would be much weaker than those recorded on ATLAS-1.

A complete review of the APEX/CIV data will be undertaken during a joint workshop scheduled for September 1995 in Moscow. The only clear manifestation of the releases in the data analyzed to-date is in the HF wideband data which exhibited a well pronounced pitch-angle-dependent signature of the releases in the MHz range.

The features of the observed phenomenon can be summarized as follows:

- All the studied neutral xenon releases with large (near normal) pitch angles, namely between 85 and 115 degrees, excited some high frequency waves in the range 3 to 10 MHz[9].
- All the studied neutral xenon releases with small (i.e. oblique) pitch angles, namely between 57 and 71 degrees, did *not* result in any such wave emission.

These observations are supported by the following HF wideband data which represent two typical high-pitch-angle releases and two low-pitch-angle releases.

6.4.1 High-Pitch-Angle Releases

Orbit #	Start Date (GMT)	Altitude (km)	Lat-N; Long-W	Vel (km/s)	Pitch Angle	Visib.
419	1/22/92 11:57:30	666.4	59.54; -17.75	8.01	95-113	Sunlight
490	1/28/92 11:57:00	838.7	58.91; -8.8	7.84	95-113	Sunlight
426	1/23/92 01:51:20	573.1	46.02; -8.898	8.1	64-71	Darkness
496	1/28/92 23:47:28	522.6	40.31; -29.3	8.15	57-70	Darkness

Table 3: Some orbital parameters for the releases whose HF Wideband data are discussed here.

In Fig. (27) we show typical HF wideband data in the range .1-10 MHz for a neutral xenon release conducted during orbit number 419. The log of the amplitude is shown in color using the rainbow palette, the release events are marked by horizontal lines, the red curves show the electron cyclotron frequency and its first five harmonics. This release was done at high pitch angles starting

[9]No data above 10 MHz are available

at 94.8 degrees when the valve was opened and ending at 113 degrees when it was closed as marked towards the bottom of the plot. The top panel shows the voltage history of the SPT and is not important for the case of neutral gas releases.

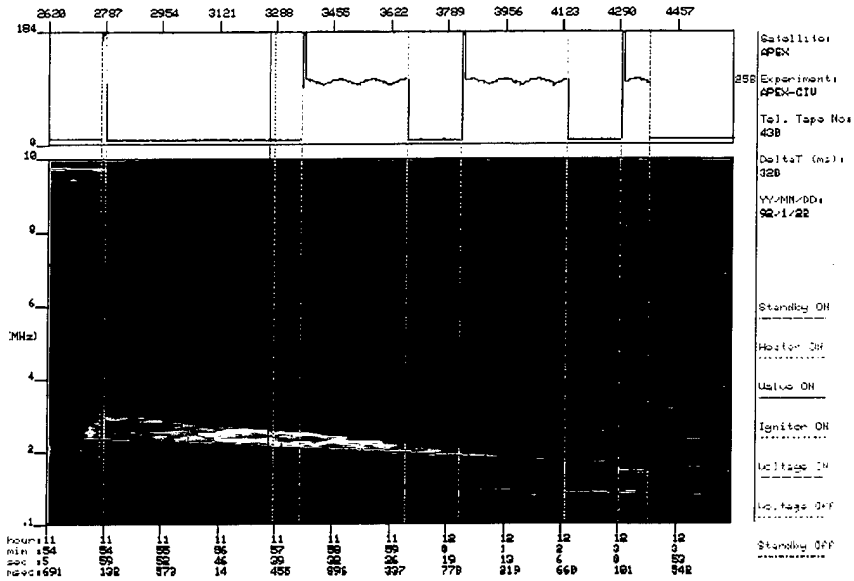

Figure 27: High-Pitch-Angle Release: Wideband HF data in the range .1-10 MHz for a neutral xenon release conducted during orbit number 419. The log of the amplitude is shown in color using the rainbow palette, the release events are marked by horizontal lines, the red curves show the electron cyclotron frequency and its first five harmonics. This release was done at high pitch angles starting at 94.8 degrees when the valve was opened and ending at 113 degrees when it was closed as marked towards the bottom of the plot. The top panel shows the voltage history of the SPT and is not important for the case of neutral gas releases.

The orbital parameters for this release are shown in Table 3.
The following observations can be noted in the HF wideband plot:

1. There is a narrowband activity (appearing as a blue band with shades of green) centered at a frequency of about 3.7 MHz that starts at the time the valve is on (within the time resolution of the instrument) [10] and lasts

[10]The apparent delay in the appearance of this activity with respect to the "Valve On" event is beyond the time resolution of the HF wideband data. In other words, within the time resolution of

until the valve is turned off, after which time it decays in bandwidth and amplitude.

2. There is a more broadband activity (appearing as mainly green band with shades of blue) extending from a frequency of about to 8 MHz to at least 10 MHz that has the same features as the activity described above except that it ends more abruptly when the valve is turned off.

3. Both of the above described bands are flat with respect to time and do not reflect the changes in the magnetic field strength reflected by the electron cyclotron harmonics shown on the same plot.

4. All other features are either natural ionospheric phenomena or wave activity that is not affected by the release.

We cannot presently offer an explanation for the exact nature of these observed wave activities. Since their frequencies do not reflect the substantial changes in the magnetic field and densities occurring during the time interval the data was recorded, they cannot be directly related to natural plasma frequencies. Nonetheless, the fact remains that their appearance and their observed features correlate well with gas release events.

Another example of the HF wideband data for a high-pitch-angle release is shown in Fig. (28). The release was made during orbit number 490 with orbital parameters shown in Table 3.

The same comments made for the wideband data of the release of orbit 419 apply for the activity in the plot of Fig. (28) with the additional observation that there is a clear enhancement to the wideband noise across the entire spectrum starting from the time the cathode heater is turned on and ending at the time when all SPT subsystems are turned off.

6.4.2 Low-Pitch-Angle Releases

Two examples of low-pitch-angle releases are shown in Figs. (29) and (30) (for orbits 426 and 496). The corresponding orbital data are also shown in Table 3.

In contrast to the high-pitch-angle releases discussed above, these plots show no wave activity that can be correlated with the any of the events associated with the neutral gas release.

6.4.3 Some Final Remarks regarding the APEX Releases and the HF Wideband Wave Activity

It is important to note that although the above described effects correlate well with the pitch angle for all the cases studied, it is not clear whether this correlation is fortuitous since other conditions, such as orbital position and associated

---

the instrument, the beginning of the wave activity and the "Valve On" event coincide.

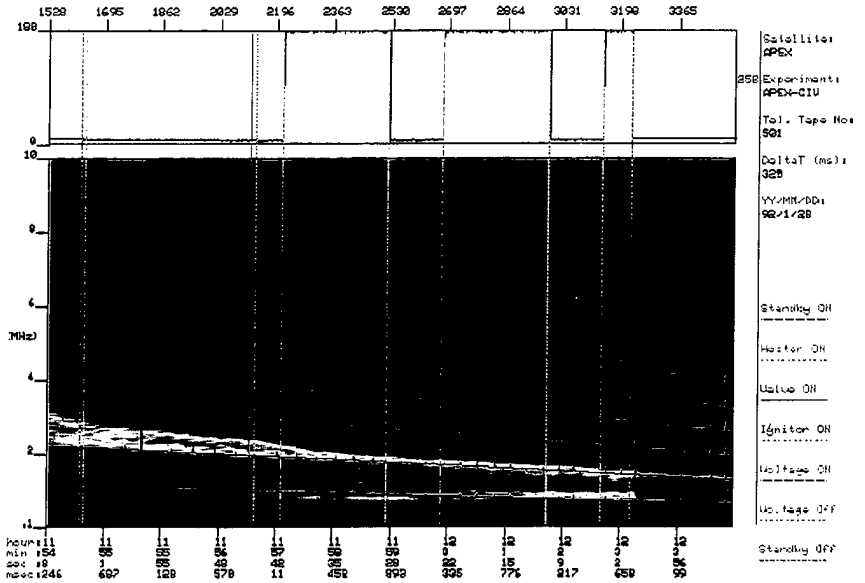

Figure 28: High-Pitch-Angle Release: Wideband HF data for orbit number 490. Same nomenclature as in Fig. (27). Pitch angle varies from 95 to 113 degrees.

plasma environment, which have correlations with the pitch angle may be the true controlling parameters for the appearance of the above mentioned emissions.

In particular, it is interesting to note that all the high-pitch-angle releases that we studied were done in sunlight while all the low-pitch-angle releases were done in darkness. This is due to an unplanned synchronicity between the attitude dynamics along the polar orbit, the solar illumination cycle and the timing of the releases. It is therefore possible that the presence of a solar flux and not the magnitude of the pitch angle is the controlling parameter for the effects described above. In such a case, the role of the solar flux in affecting HF wideband activity through intermediary effects such as plasma enhancement due to photo-ionization may be worthy of investigation. Since the solar flux does not vary much during the time of the release and since the release mass flow rate is constant, such a mechanism may offer an explanation to the constancy of the frequency of the excited bands as a function of time.

Finally, we cannot rule out the role of ground-based broadcasting stations in creating the flat frequency bands observed in the HF spectra. This scenario however begs the question of why these bands appear (or are enhanced) only *during* the releases and not after.

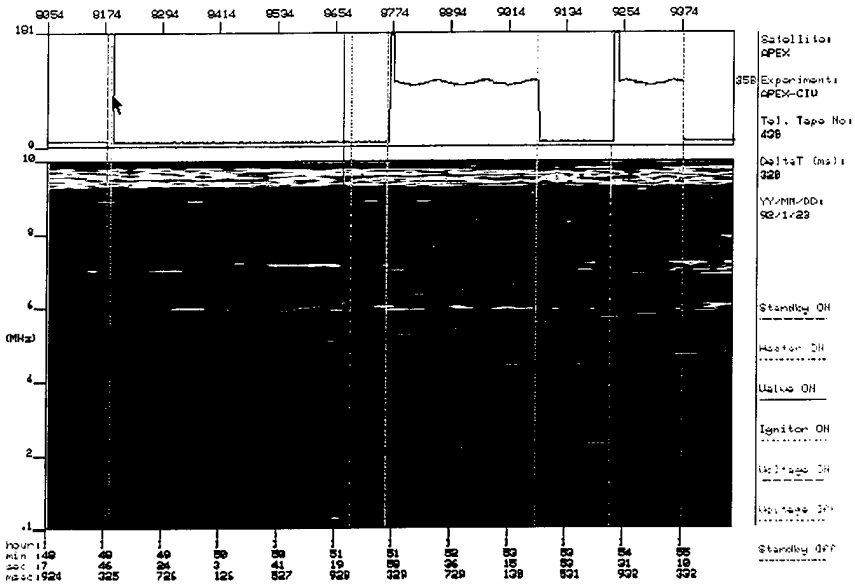

Figure 29: Low-Pitch-Angle Release: Wideband HF data for orbit number 426. Same nomenclature as in Fig. (27). Pitch angle varies from 64 to 71 degrees.

In any case, it is probably conservative to state at this stage that, although the APEX releases have yielded interesting data, correlations and new questions, they have not yet produced a positive test of CIV. In light of the more pronounced evidence of positive CIV tests observed during the ATLAS-1 releases, it may be speculated that the lack of such strong evidence on APEX may well be due to the very low mass flow rate of xenon. Indeed, an evaluation of the CIV criteria described in Section 3.5 for the APEX releases lead to many negative criteria mainly because of the low mass flow rate of released gas.

7 Particle Simulation of CIV Tests in Space

We have invested a substantial effort in the use of advanced PIC (particle in cell) plasma simulation codes for the study and interpretation of the releases we have been studying, in order to gain better insight into the basic processes governing anomalous ionization.

The study of the ATLAS-1 tests can be enhanced by applying advanced numerical simulation codes that can handle realistic conditions of the experiments. In this section of the report, we discuss a numerical simulation model

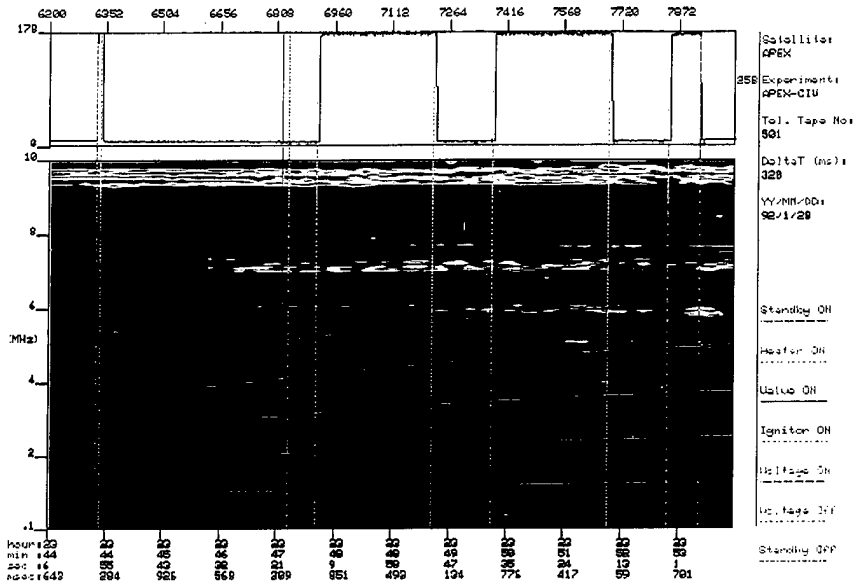

Figure 30: Low-Pitch-Angle Release: Wideband HF data for orbit number 496. Same nomenclature as in Fig. (27). Pitch angle varies from 57 to 70 degrees.

developed specifically to study such neutral gas releases in the ionosphere. We present simulation results obtained by applying the code to the ATLAS-1 CIV tests using realistic parameters reported above and in ref. [23].

7.1 Background on PIC simulation of the CIV Phenomenon

Theoretical studies and observations of staged CIV interactions in the laboratory have characterized the phenomenon as one in which the free energy source associated with the directed kinetic energy of the relative motion between two plasma components excites plasma microinstabilities of the streaming (or beam) type. These instabilities would then channel a substantial part of the relative kinetic energy to heat electrons preferentially creating a substantial population of electrons with energies above ϵ_i, which would then contribute to a substantially enhanced ionization process. The energy going into ionization ultimately comes from the relative motion (i.e. the beam kinetic energy) and consequently the CIV interaction results in slowing down the relative velocity to near u_{ci} during the interaction.

The instability, typically of the lower hybrid mode, is originally ignited by the cross-streaming of "seed" charged particles in the neutral gas with respect

to plasma particles and maintained through the cross-streaming between newly created and old charged particle populations. The lower hybrid wave can easily be destabilized by an ion beam perpendicular to magnetic field when the beam velocity is above the ion thermal speed. It must be emphasized that in all CIV scenarios a "seed" of charged particle must initially exist in the neutral gas. Such seeds could be due to any weak ionization of photonic or thermal origin and, most likely in the case of releases in space, charge exchange collisions.

There has been a few neutral gas injections in the ionosphere to study CIV using shaped charges released from sounding rockets[18]. In these rocket experiments the plasma yield was typically small and difficult to relate conclusively to CIV effects. The following two reasons for the low ionization yield of these experiments have been proposed in the literature: inefficient ion seeding of the neutral gas[39] (due to low rate of charge exchange collisions[40]) and the shortness of the interaction time scale which would produce small yields even if CIV was operative[18].

As mentioned earlier, the ATLAS-1 releases showed a factor of 60 increase in plasma density following each of the 100 msec long neutral xenon releases[23]. Wave activity in the lower hybrid band during the releases was also reported[35] and discussed in Section 3.7 above.

7.2 Previous Numerical Simulations

Since 1984, particle-in-cell (PIC) codes have been used in the study of the CIV effect. The PIC simulations to date have clarified many aspects of the CIV effects including: the threshold aspect of the interaction[41], suprathermal electron production[42], the role of electromagnetic effects[43], the presence of ionization fronts[44], the importance of elastic scattering and the atomic physics such as charge exchange, excitation and ionization from metastable states[40, 45] and the importance of initial ion seed in the neutral gas[39].

Most of the simulations have been one-dimensional except for those in ref. [43, 44] in which two-dimensional simulations with artificial mass ratios were carried out using a small grid. Consequently, until now the simulations have been concerned with the investigation of fundamental aspects of CIV and were not directly applied to any specific gas release experiment in space.

In order to model neutral gas releases in the ionosphere under realistic conditions we use a 2&1/2-dimensional PIC code that can handle real mass ratios and realistic spatial extensions. The effects included in the model are listed in Table 1 for comparison with those of previous simulation models. The present model neglects electromagnetic effects since these were shown not to be important for the CIV interaction when[43]

$$V < (1 + \beta_e)^{1/2} v_A \tag{56}$$

(where V is the relative velocity, β_e the electron beta and v_A the Alfvén velocity) a condition amply satisfied in most ionospheric release experiments. Although

Reference	[41]	[42]	[46]	[43]	[44]	[40]	[45]	[39]	This work
Year	84	85	86	88	88	90	90	92	94
Dimensions	1-D	1-D	1-D	2-1/2-D	2-1/2-D	1-D	1-D	1-D	2-1/2-D
EM effects				√	√				
e^--impact ioniz.	√		√	√	√	√	√	√	√
Charge X. Coll.			√	√	√	√	√	√	√
e^--impact excit.			√	√	√	√	√		
Elastic Scat.			√	√	√	√	√	√	
Real Dimensions									√
Real m_i/m_e								√	√

Table 4: Chronological list (1984-1994) of referenced PIC simulation models used for CIV studies and the effects considered by each. The effects are, dimensionality, electromagnetic effects, ionizing, charge exchange, excitation and elastic collisions, real spatial dimensions and real mass ratios.

various collisional processes can be easily included and handled by the code we limit the simulations discussed here to include only the most important ones, namely ionizing (electron impact) and charge exchange collisions.

7.3 Simulation Model

Shown in Fig. (31) is a sketch of the particle simulation model developed specifically for studying the neutral gas release experiments into the ionosphere. The model is two-and-one-half-dimensional in which two spatial coordinates, x and y, and three velocity components are followed in time. Full dynamics of the ions are followed in time, while the electrons are treated as guiding center particles, where rapid gyration around the guiding center has been averaged out. This averaging is tolerable for our case because we are not interested in the high frequency electron gyromotion, and it allows us to use a larger integration time step, which is essential for simulations using realistic plasma parameters[47]. The code follows the motion of the background and ionized plasma in a given uniform magnetic field representing the geomagnetic field and a self-consistent electrostatic field. Extension to full three dimensions is straightforward by using higher order interpretations to simulate a large three dimensional volume[47].

Using the Langmuir probe measurements for the ATLAS-1 releases reported above and in ref. [23] we set the background oxygen ion density at $5 \times 10^4 cm^{-3}$ and the electron temperature at 0.1 eV. We also set the magnetic field strength at 0.7 gauss and the pitch angle of the velocity vector at 81 degrees as was the case for the actual releases. Main components of the background neutral gases

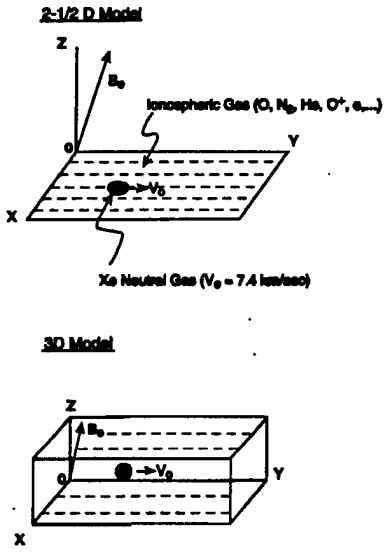

Figure 31: Sketch of the numerical simulation models developed to study neutral gas release experiments into the ionosphere. A two-and-one-half-dimensional model (top) has two spatial coordinates, x and y, and three velocity components. Extension to a three dimensional model (bottom) is straightforward.

are O and N_2 whose densities are $10^7 - 10^8/\text{cm}^3$. The Debye length is typically 1 cm and the electron plasma and gyrofrequencies are about 10^7/s. The oxygen ion plasma frequency which is close to the lower hybrid frequency is about equal to 5.8 x 10^4/s.

The mass flow rate of 1.5 moles/s of the ATLAS-1 releases, which lasted 100 msec each, is equivalent to 10^{23} particles for a typical release. The reported observations suggest that a rapid ionization took place within a few ms[23].

The interaction of the neutral xenon gas with the background plasma is treated by means of the Monte-Carlo technique[48] including charge exchange

$$X_e + O^+ = X_e^+ + \text{O}$$

and electron impact inonization

$$X_e + \text{e} = X_e^+ + 2\text{e}$$

The cross section for the oxygen-xenon charge exchange is 10^{-16}cm^2 at 10 eV electron energy and increases to $2\text{x}10^{-15}\text{cm}^2$ at 100 eV[49]. The ionization

energy of the ground state xenon atom is 12.13 eV and the dependence of the cross section for electron impact ionization on the energy is described in ref. [50] and is shown to increase almost linearly from threshold, reaching the maximum of 6.2 x 10^{-16}cm^2 at 120 eV then decreasing to about 2 x 10^{-16}cm^2 at 1 keV.

In the simulations discussed here, we did not include other binary interactions which could be easily handled by the code. Among such interactions are line excitation, ionization from the (6s) metastable state, which can have cross sections as large as 10^{-14}cm^2 and elastic scattering of the X_e^+ ions by the xenon and oxygen neutral gases. These collisional effects will be included in a future simulation.

The dimensions of the simulation grid, shown in Fig. 1 are set to either $256(x) \times 512(y)$ or $256(x) \times 1024(y)$ which, for our particular case with the Debye length of 1 cm, correspond to either 256 cm × 512 cm or 256 cm × 1024 cm in real dimensions after setting the grid size equal to the Debye length.

Since the space shuttle and hence the neutral xenon gas are moving at 7.4 km/s orbital speed in the y direction, our simulation system is therefore traversed in 1.4 ms, unless the system length is stretched in the y direction.

The ATLAS-1 space observations[23] show, however, that a significant enhancement of ionization takes place within that time scale, so that the present simulation is large enough to study at least the initial stage of the interaction.

As mentioned earlier, real mass ratios are used for the electrons, oxygen and xenon ions. The time step of integration used in the simulation was $(2 - 5)\omega_{pe}^{-1}$ which corresponds to $(2 - 5)\text{x}10^{-7}$ s. While the detailed shape of the xenon gas is not known, we shall assume in our model that it is a sphere with a uniform density moving at the shuttle speed in the ionosphere. Since the xenon gas expansion speed of 61m/s is much lower than the 7.4 Km/s orbital speed, the changes in the radius and the density during the simulation were ignored.

The boundary conditions for the particles and fields are the following. First, the background ionospheric oxygen ions and electrons, which are assumed uniform initially, are assumed periodic. The ionospheric ions, for example, leaving a boundary are inserted back from the opposite boundary. This is roughly equivalent to an assumption of a vast ionospheric background. The xenon ions produced by the impact ionization and charge exchange are assumed lost once they leave the boundary of the simulation. High energy electrons accelerated by the plasma waves are also considered lost once they cross the simulation boundaries. The ideal boundary conditions for the electrostatic potential would be such that the potential vanishes at a point where the distance from the xenon cloud is far enough. This can be approximated by using a sine Fourier transform for the system which sets the values of the potential at the boundary zero. As the waves grow to large amplitude at a later phase of the simulation, however, the plasma waves reach the boundary without much attenuation, so that some of the waves are reflected. In fact, the use of the periodic boundary condition gives results not much different from those that would be obtained using the sine Fourier transform. This is because the largest wave amplitude in the system

remains concentrated near the xenon cloud.

In the example given below, we shall assume that the neutral xenon gas has a density of $3 \times 10^{14}/cm^3$ with its radius of 8 cm. This would corresponds to an early phase of the gas release.

The resulting evolution of the beam instability, the formation of suprathermal tails, the wave emission and the enhancement to ionization under the above listed conditions are described by the simulation results in the next section.

7.4 Simulation Results

The released xenon neutrals have effectively the spacecraft orbital velocity of 7.4 km/s, and can undergo charge exchange with the background oxygen ions, resulting in an energetic xenon ion beam. Such an xenon ion beam is able to excite plasma waves near the oxygen lower hybrid and ion cyclotron waves propagating nearly perpendicular to the magnetic field. The lower hybrid and ion cyclotron waves, in turn, accelerate xenon ions perpendicular to magnetic field and electrons along magnetic field at roughly the same rate[51]. The energetic electrons in turn can enhance ionization of the xenon neutral gas so that the original streaming energy of the neutral xenon is channeled through the waves to the ionization. The coupling of the lower hybrid wave to ions and electrons is comparable at an angle of propagation given by $k_{||}/k_{\perp} = (m_e/m_i)^{1/2}$. If the angle is larger than this value, more energy is fed into the electrons thus enhancing ionization. The threshold ion beam velocity, however, also increases with this angle[51]. This picture is upheld by the following simulation results.

Shown in Fig. (32) are the results of the simulations at $t = 1000\ \omega_{pe}^{-1}$ which corresponds to approximately 0.1 ms. The electrostatic contour plot shown in panel (a) indicates a presence of potential fluctuations near the xenon cloud caused by the newly born xenon ions through charge exchange. Since the neutral xenon density is high, the rate at which the xenon ions is created is substantial. The rate is given by $\sigma_c n_{O^+} n_{X_e} V_r$, so that at t = 1 ms the xenon density becomes comparable to the oxygen density near the xenon cloud. The potential fluctuations arise from the high speed xenon ions moving through the ionosphere. Here V_r is the relative speed between the neutral xenon gas and the oxygen ions.

Shown in panel (b) of Fig. (32) is the location of the xenon cloud moving at a speed of 7.4 km/s. As mentioned earlier, the cloud remains unchanged on the time scale of the simulation. A scatter plot of the electron spatial distribution are shown in panel (c), which indicates that it is essentially uniform at this time. The average electron density shown in panel (d), however, indicates significant perturbations at the center of the system where the xenon cloud is located. This perturbation is created by the newly born xenon ions trying to maintain the charge neutrality. The xenon ions are moving at high speed so that they tend to generate charges at the boundary, generating density perturbations as well as potential fluctuations shown in panels (a) and (d).

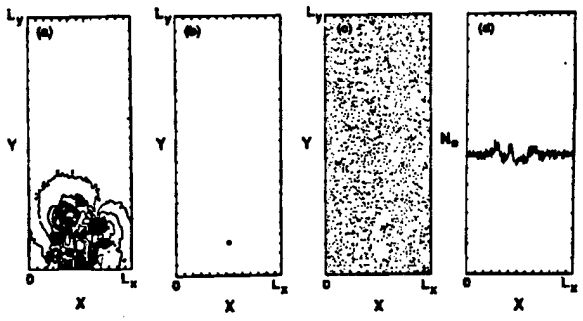

Figure 32: Simulation results for a neutral gas cloud with a density of $3x10^{14}/cm^3$ and a radius of 8 cm at $t = 0.1$ ms. Shown in the Figure are electrostatic potential contours (a), location of the neutral xenon gas in the (x, y) plane (b), scatter plot of the ionospheric electrons (c) and the electron density averaged over y-direction (panel d). At this early time of the simulation, the charge exchange process between the xenon neutral gas and the ionospheric oxygen ions produced a small number of xenon ions generating potential fluctuations near the xenon cloud. Local density perturbations can also be seen in panel (d).

Shown in Fig. (33) are the corresponding distributions for the electron velocity (a), the oxygen ion perpendicular velocity (V_x) (b), xenon ion perpendicular velocity (V_x), (c), and (V_y) , (d) components. Since the time is still short for the lower hybrid waves to grow, electrons and oxygen ions are essentially the same as the initial ionospheric distributions at 0.1 eV. The xenon ions produced by the charge exchange processes are streaming at the orbital speed. Note that the velocities shown in Fig. (33) are normalized with respect to the thermal velocity at the ionospheric temperature.

Shown in Fig. Fig. (34) are the results of the simulations at t = 4 ms for scatter plots for the xenon neutral gas (a), scatter plot for thr xenon ions (b), and newly created electrons (c) produced by electron impact ionization. The xenon neutral cloud has moved further across the magnetic field. The xenon ions also move with the orbital speed, together with the xenon neutral gas. The xenon ions, however, spread radially as they gyrate out from within the cloud. The newly created electrons spread out rapidly as seen in panel (c) of Fig. (34) owing to their large mobility. The charge neutrality is maintained by the background ionospheric oxygen ions and electrons, whose densities are much higher than the newly born electrons at this time. We note that at this time the number of the xenon ions produced by charge exchange is much larger than the electron impact produced xenon ions (the ratio is 100 to 1). This is

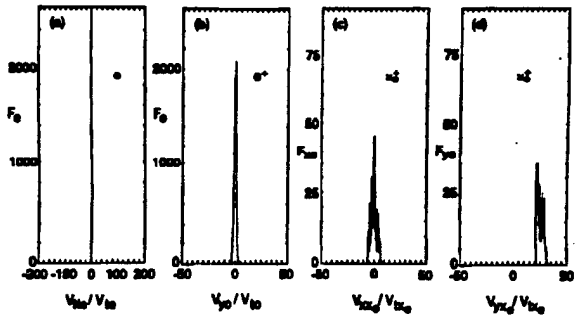

Figure 33: Results of the same simulation as in Fig. (32), showing distributions for the electron velocity along magnetic field (a), the oxygen ion perpendicular velocity V_y (b), the xenon ion perpendicular velocity V_x (c), and the associated V_y component (d). Both the electrons and oxygen ions remain the same as the initial ionospheric distributions, while the xenon beam ions are created through charge exchange. Note that the velocities are normalized by the thermal velocities of the corresponding species at the ionospheric temperature, 0.1 eV.

because there are very few high energy electrons produced at this time.

Shown in Fig. (35) are the corresponding velocity distributions for the electrons (a), oxygen ions (b), and xenon ions (c) at this time (0.4 ms). It is clear that both the electrons and oxygen ions are accelerated somewhat from their initial ionospheric distributions, which are also included in panels (a) and (b). The xenon ion beam plotted in panel (c) shows a slowing down from the orbital speed, and, at the same time, a spreading caused by velocity space diffusion. The acceleration and diffusion of the particles are caused by plasma instabilities near the lower hybrid waves. The energy lost by the xenon ion beam is channeled to the acceleration of the electrons, which can, in turn, enhance the ionization of the neutral xenon gas substantially as the suprathermal electron population increases.

Shown in Fig. (36) is the power spectrum for a Fourier mode, $(m, n) = (4, 3)$, (a), and the spectrum measured at a location near the xenon neutral cloud, (b). It is clearly seen that both spectra have a peak frequency near 2 ω_{po} which is close to the lower hybrid frequency including the electron response[51]. This is a direct evidence for the excitation of the oxygen lower hybrid waves by the xenon beam generated by the charge exchange process. The electrons accelerated by the lower hybrid waves, in turn, should increase the impact ionization leading to further enhancement of the instability and a self-sustaining collective ionization process.

Shown in Fig. (37) are the results of the simulation at t = 0.7 ms. The spatial

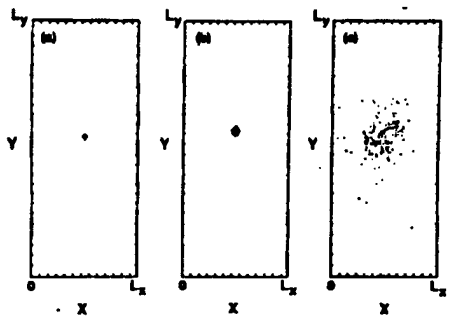

Figure 34: Results for the location of the xenon neutral gas (a), scatter plots for the xenon ions (b), and for the newly created electrons (c) produced by electron impact ionization. Note the xenon ions move with the xenon neutral gas as expected except for radial expansion as shown in panel (b). The newly created electrons, on the other hand, spread out quickly from the neutral gas. Charge neutrality is maintained by the ionospheric oxygen ions and electrons.

distribution of xenon ions produced by electron impact ionization is shown in panel (a). Note that the cloud expands radially as it moves with the shuttle orbital velocity. It is interesting to note that the center of the cloud has much higher density surrounded by the outer region at lower density. This is clearly shown in panel (b) where the average xenon ion density is shown as a function of x. The peak xenon ion density is located near the center of the xenon neutral cloud, and its density is a quarter of the ambient oxygen ion density. At this time the number of xenon ions produced by the electron impact exceeds the number of xenon ions produced through charge exchange with ionospheric ions. More on this point will be said later.

The electron velocity distribution is shown in panel (c) of the same figure at t = 0.7 ms together with the initial ionospheric electron distribution. It is clear that the tail electrons are much hotter now, with a substantial portion having energies as high as 20 eV. Such electrons can indeed enhance the impact ionization of the neutral xenon gas because of both the enhanced density of electrons above the ionization threshold and the increase in the ionization cross section at these higher energies. The xenon ion V_y velocity distribution produced by the impact ionization is shown in panel (d). The drift speed is substantially smaller than the orbital speed, suggesting that the xenon kinetic energy associated with the orbital motion is channeled to the ionization as well as to the acceleration of various kind of particles.

At t = 1 ms, as shown in Fig. (38), the heating of the electrons and ionization of the xenon gas happen at a faster rate. The energy distribution of the electrons

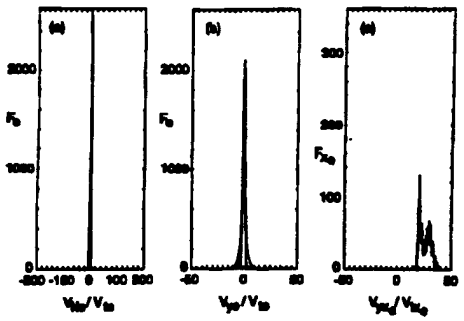

Figure 35: The velocity distributions for the electrons (a), oxygen ions (b), and xenon ions (c) at t = 0.4 ms. It is shown that acceleration of the electrons along and oxygen ions across the magnetic field began to take place as a result of the plasma instability near the oxygen lower hybrid waves. The delta-function-like distributions in panels (a) and (b) correspond to the initial electron and oxygen ion distributions at the ionospheric temperature.

shown in panel (a) indicates a further suprathermal tail enhancement, with a substantial portion of the electrons having energies as high as 60 eV. The ionoshperic oxygen ions shown in panel (b) is also heated substantially. The xenon ions produced by the impact ionization shown in panel (c) and by the charge exchange shown in panel (d) are accelerated and at the same time their drift speed have decreased significantly. Note that the number of xenon ions produced by impact ionization is larger than the number of xenon ions produced through charge exchange by a factor of 3 at this time.

Shown in Fig. (39) is the time record of the xenon ions produced through charge exchange (open circles) and by electron impact ionization (solid circles). It is clear that the impact ionization, once it is triggered, increases much more rapidly than the charge exchange ionization which is more or less linear in time. Since the impact ionization depends on the high energy electron population, it is essential to accurately follow the development of the electron distribution by means of self-consistent means such as by the PIC simulation reported in this work. The electron impact ionization completely dominates over charge exchange ionization after a few hundred microseconds into the simulation demonstrating that an anomalous process such as CIV could indeed be important during neutral gas release experiments in space, in general, and the ATLAS-1 xenon releases, in particular.

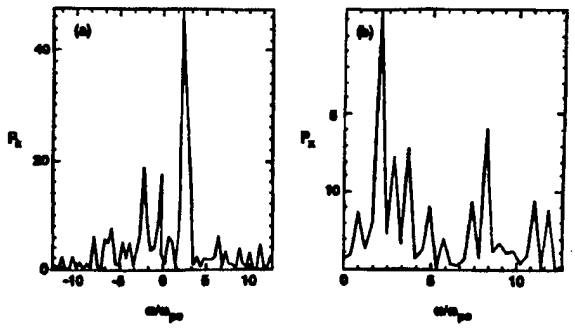

Figure 36: Power spectra of the charge density for a Fourier mode $(m, n) = (4, 3)$ (a), and at a location near the neutral gas in the (x, y) plane (b). Note for both cases, a peak near 2 ω_{po} is clearly seen, which corresponds to the oxygen lower hybrid wave.

7.5 Concluding Remarks regarding the Simulations

We have used a particle simulation model to study the fundamentals of anomalous ionization and gain insight into the character of the wave generation, particle heating, diffusion and enhanced plasma production that accompany this type of ionization.

The model was applied to the xenon gas release experiments conducted during the ATLAS-1 mission. The model still does not include all the subsidiary binary reactions (line excitation and radiation, elastic collisions, stripping ionization and multiple ionization) which will be added in future simulations. It has shown, however, how xenon ions, created from the released gas through charge exchange with ionospheric ions, and streaming with a velocity exceeding u_{ci}, can drive plasma waves near the lower hybrid frequency unstable, which can produce suprathermal electrons that can, in turn, lead to a rapid ionization of the neutral gas. This is essentially the CIV effect.

The number of xenon ions produced through the collective (CIV) effect (i.e. by impact with suprathermal electrons accelerated by the waves) increases much more rapidly than the number of ions created through classical charge exchange ionization. This is in contrast with the finding in ref. [52], where a quenching of the CIV effect was expected to happen when the CIV ionization rate becomes comparable with the charge exchange rate. The reason for this discrepancy may well be due to the neglect of the growing nonlinear effects in the quasi-linear analysis of that work, as suspected by the authors themselves.

While our numerical simulation followed the evolution of the xenon gas release only to about 1 ms time, the total number density of the xenon ions pro-

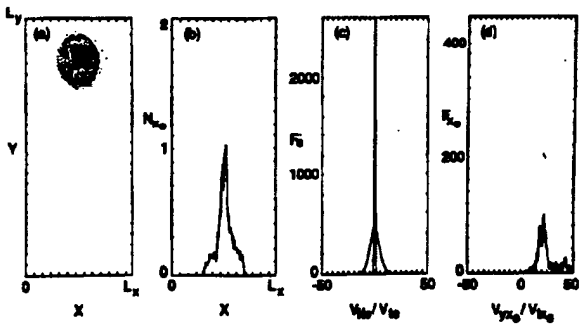

Figure 37: Results of the simulation at t = 0.7 ms for the xenon ion cloud produced by the electron impact in the (x, y) space (a), its average density in x (b), the electron velocity distribution (c), and the xenon ion velocity distribution (d).

duced by CIV and charge exchange becomes already comparable to the density of the ionospheric oxygen ions. With longer simulations we expect the xenon ions produced through the CIV effect to keep on increasing rapidly so that their density can far exceed the oxygen ion density within a relatively short period of time.

Since we found that, for the ATLAS-1 release conditions, CIV ionization dominates over charge exchange after only a short time (a few hundred microseconds), and since the observations show an increase of the density of a factor of 60 a few milliseconds into the release[23], it seems likely that this density enhancement can be attributed to the CIV effect. This would be ascertained more quantitatively when all the relevant subsidiary reactions are included in the model.

The findings described above concerning the nonlinear evolution of wave generation and particle heating during anomalous ionization, will be instrumental in the further development of our model of anomalous ionization in plasma thrusters[53]. By combining the detailed ionization chemistry of that model and the nonlinear plasma physics revealed in the present study, we hope to arrive at a realistic model that can be used to improve the realism of plasma fluid codes of plasma thrusters.

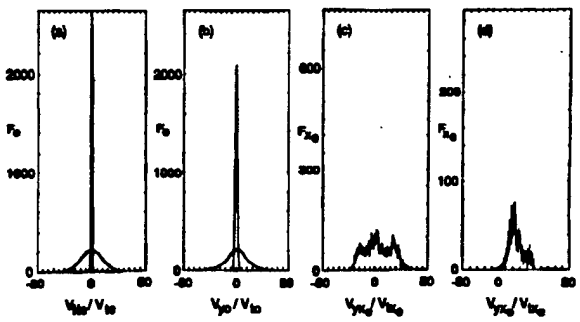

Figure 38: Results of the simulation at t = 1 ms for the velocity distributions of the electrons (a), oxygen ions (b), electron impact produced xenon ions (c), and charge exchange produced xenon ions (d).

8 Analytical Work: Modeling Anomalous Ionization in the MPD Thruster

Synopsis In this section we present a prescription for the electron energy distribution function that allows the representation of suprathermal electron tails such as those produced by the nonlinear effects of plasma microturbulence. The model is specified by a bulk temperature, a tail fraction, a tail energy scaling parameter and a tail spread parameter. The parametric distribution function is combined with a multi-level atomic model of argon and used to calculate the reaction rates for 23 collisional excitation transitions from ground state by electron impact by applying a high-accuracy quadrature on the convolution integrands containing the appropriate cross-sections. The prime goal was the study of the parametric dependencies of the minimum ionization characteristic length on the tail parameters. Calculations are compared with the recent measurements of the dimensions of an ionization "front" observed in a low-power MPD thruster by Randolph et. al. The ionization length which is at least 10 times smaller than that calculated assuming Maxwellian statistics is shown to be more consistent with distributions having suprathermal tail fractions and energies that could be produced by plasma microturbulence. Tail fractions of about 1%, under some conditions, can reduce the spatial extent of ionization to the millimeter level. Typical tail parameters obtained from a particle simulation code designed for the study of anomalous ionization were used to illustrate the model's implications.

Organization We start in Section 8.1, with a model for the electron energy distribution function that allows the representation of suprathermal electron

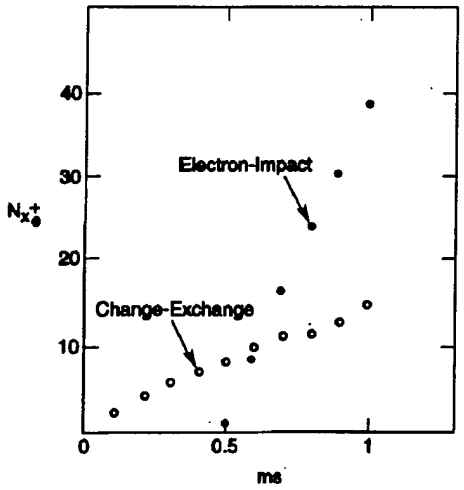

Figure 39: Time record for the charge exchange produced xenon ions (open circles) and electron impact produced xenon ions (solid circles). The average xenon ion density is normalized by the average ionospheric plasma density, assuming that the total xenon ions are confined within the initial xenon neutral cloud. It is shown that the ionization produced xenon ions obtained a density as much as 30 times of the background oxygen ion density if there were no xenon ion diffusion in space. As discussed in the text, xenon ions actually diffused out radially, reducing its density comparable to the oxygen ion density at t = 1 ms.

tails such as those produced by the nonlinear effects of plasma microturbulence. In Section 8.2, we describe aspects of the calculations of collisional excitation reaction rates that are central to our investigation. The resulting numerical model is then used in Section 8.3 for a study of the parametric dependencies of the minimum ionization characteristic length on the tail parameters. Calculations are compared with the recent measurements of the dimensions of the ionization "front" observed in a low power MPD thruster by Randolph et. al.[2]. Finally, is Section 8.4, typical tail parameters obtained from a particle simulation code designed for the study of anomalous ionization are used as an example.

8.1 Electron Distribution Function with a Suprathermal Tail

We start by assuming that the bulk of the electrons corresponding to a fraction $(\mu - 1)$ of the entire distribution (where μ is the tail fraction), are represented

by a Maxwellian with a temperature T_B

$$\left(\frac{dN}{N}\right)_B = \frac{4v^2}{\pi^{1/2}(2kT_B/m)^{3/2}} \exp\left[-mv^2/2kT_B\right] dv, \tag{57}$$

where all symbols are standard and the B subscripts refer to the "bulk" part of the distribution.

In order to control the extent and shape of the tail, we introduce a distribution for the fraction μ representing the suprathermal tail contribution, with a velocity drift u_0 and its own equivalent "temperature" T_T which we will refer to as the "tail energy scaling parameter",

$$\left(\frac{dN}{N}\right)_T = \frac{\dfrac{4v^2}{\pi^{1/2}(2kT_T/m)^{3/2}} \exp\left[-m(v-u_0)^2/2kT_T\right]}{\Omega} dv. \tag{58}$$

where the T subscripts refer to the "bulk" part of the distribution and Ω is a normalization term that must be such that

$$\int_0^\infty \left(\frac{dN}{N}\right)_T = 1. \tag{59}$$

Ω is therefore

$$\begin{aligned} \Omega &= \int_0^\infty \frac{4v^2}{\pi^{1/2}\left(\dfrac{2kT_T}{m}\right)^{3/2}} \exp\left[-\frac{m(v-u_0)^2}{2kT_T}\right] dv \\ &= 2 + \left(2\frac{u_d}{v_{tT}}\right)^2 \end{aligned} \tag{60}$$

where $v_t = (2kT/m)^{1/2}$ is the thermal velocity.

The composite distribution function $f(v)$ is the sum of the bulk Maxwellian and the tail model adjusted by their respective fractions,

$$f(v)dv = (1-\mu)\left(\frac{dN}{N}\right)_B + \mu\left(\frac{dN}{N}\right)_T \tag{61}$$

A parametric plot showing the shape of the resulting distribution and its tail is shown in Fig. (40) where a bulk 2 eV temperature (8.4×10^5 m/s) was chosen along with a tail energy scaling parameter of 6.4 eV (for relevance to the calculations in the following sections). The drift speed was set equal to the thermal velocity at that "temperature" i.e. 15×10^5 m/s and the tail fraction was varied parametrically.

The integral of $f(v)$ is plotted as a function of v in Fig. (41) showing the contribution to the integral of a given velocity range with the varying tail fraction, μ.

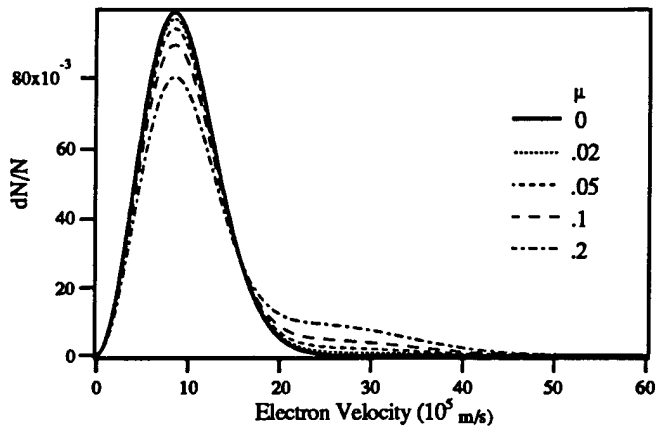

Figure 40: Adopted distribution model for a range of tail fractions, μ. T_i=6.4, $u_d = v_{tT} = 15 \times 10^5$ m/s.

Since our goal is the calculation of reaction rates which are obtained by weighing the cross sections with $vf(v)$ and integrating from a certain reaction energy level to infinity, we choose to use the following convenient parameters.

$$u_{ij} \equiv \frac{\epsilon_{ij}}{kT}; \qquad U_{ij} \equiv \frac{\epsilon}{\epsilon_{ij}}; \tag{62}$$

where the energy ϵ becomes the implicit variable and ϵ_{ij} represents the energy involved in going from level i to level j. The resulting model for the distribution function becomes

$$\begin{aligned} f(U_{ij})dU_{ij} = (1-\mu)\frac{2}{\pi^{1/2}} u_{ij}^{3/2} U_{ij}^{1/2} \times \\ \exp\left[-u_{ij}U_{ij}\right] dU_{ij} \\ +\mu \frac{e^{-\tau^2}}{\pi^{1/2}\left(1+2\tau^2\right)} u_{ij}^{3/2} U_{ij}^{1/2} \times \\ \exp\left[-u_{ij}U_{ij} + 2\tau u_{ij}^{1/2} U^{1/2}\right] dU_{ij} \end{aligned} \tag{63}$$

where we have also introduced the tail spread parameter τ defined by

$$\tau \equiv \frac{u_d}{v_{tT}}. \tag{64}$$

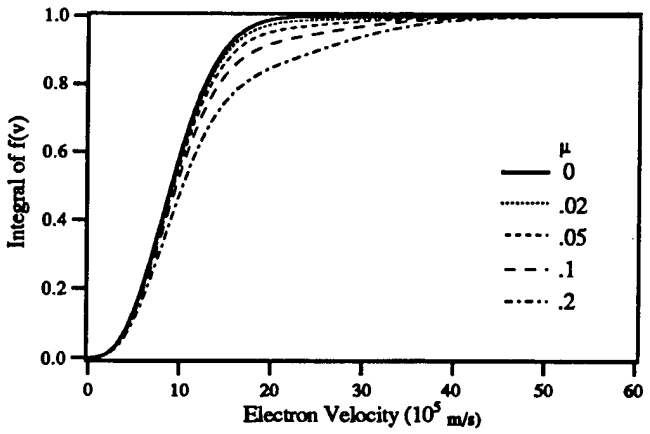

Figure 41: Integral of the adopted distribution model for a range of tail fractions, μ. T_i=6.4, $u_d = v_{tT} = 15 \times 10^5$ m/s.

8.2 Reaction Rate Models for Collisional Excitation

Randolph et. al.[2] treated the case of a Maxwellian distribution and calculated a most conservative estimate of the ionization length, λ_i, (i.e. much shorter than would be predicted by a more accurate model). They found that even the most conservative estimate is still more than an order of magnitude longer than their experimental measurements. For the sake of continuity we follow their conservative assumptions. Namely, we neglect all reactions that tend to increase λ_i and thus limit ourselves to collisional excitation and neglect the reverse processes. This also carries the implicit assumption that once an atom is in a highly excited state it is easily (and thus is considered) ionized. Radiative absorption is one mechanism that could possibly enhance ionization and thus shorten λ_i but it was not considered in ref. [2] with the argument that it should not be substantial at the low density conditions of the low power MPD thrusters[54].

In essence such estimates represent the lowest bound on λ_i for a given set of conditions.

In order to estimate the impact of distributions with suprathermal tails on shortening the effective ionization length from its classical values, we need to use the above model along with the relevant cross-sections to calculate the associated reaction rates.

The reaction rates R_{ij} we are seeking are obtained from

$$R_{ij} = \langle \sigma_{ij} v \rangle = \int_1^\infty v_{th} u_{ij}^{1/2} U_{ij}^{1/2} \sigma_{ij} f\left(U_{ij}\right) dU_{ij} \tag{65}$$

where σ_{ij} is the cross-section for the transition in question. Since we are dealing with excitation by electron impact from the ground state, we have $i = 1$.

For cross-sections of atomic excitation by electron-impact, we use the well-established semi-empirical formulae of Drawin[55]:

For allowed transitions the cross-section σ_{ij}^A is:

$$\sigma_{ij}^A = 4\pi a_0^2 \left(\frac{\epsilon_1^H}{\epsilon_{ij}}\right)^2 f_{ij}^A \alpha_{ij}^A \left[\frac{U_{ij}-1}{U_{ij}^2}\right] \ln\left(1.25\beta_{ij}U_{ij}\right). \tag{66}$$

For parity-forbidden transitions the cross-section σ_{ij}^P is:

$$\sigma_{ij}^P = 4\pi a_0^2 \alpha_{ij}^P \left[\frac{U_{ij}-1}{U_{ij}^2}\right]. \tag{67}$$

For spin-forbidden transitions the cross-section σ_{ij}^S is:

$$\sigma_{ij}^S = 4\pi a_0^2 \alpha_{ij}^S \left[\frac{U_{ij}^2-1}{U_{ij}^5}\right]. \tag{68}$$

In the above, f_{ij}^A is the absorption oscillator strength for optically allowed transitions, α_{ij} and β_{ij} are fit coefficients. All these parameters are part of the atomic physics model adopted for the calculations (see Table 8.2). Finally, ϵ_1^H is the ionization potential of hydrogen from ground state.

We consider 23 known excitation transitions from the ground level of the argon atom. These levels are part of the 65-level lumped atomic model for argon compiled and described by Vlček in ref. [3]. All the information needed to represent these 23 transitions in the above equations are listed in Table 8.2 extracted from ref. [3].

8.3 Results

The integral in Eq. (65) is evaluated with a 16-point Gauss-Legendre quadrature to insure high accuracy.

In order to keep continuity with the previous work, we use the expression for λ_i used by Randolph et. al[2]

$$\lambda_i \simeq \frac{v_f}{n_e \Sigma_{j>1} R_{1j}} \tag{69}$$

where v_f is the flow velocity and n_e is the electron density. In order to find the shortest predicted λ_i we set v_f to its lowest value in the MPD thruster $v_f = v_{\text{inlet}} \simeq 320\ m/s$ and set n_e to the highest possible density for the low

power MPDT ($n_e = 1 \times 10^{14}$ cm^{-3}). In the same spirit we choose for the electron (bulk) temperature T_B the high end of the values measured for the low power thruster (i.e. T_B=2 eV). We set the tail spread parameter τ to unity (i.e. $u_d = v_{tT}$) to reduce the number of tail control parameters and vary the other two tail quantities: the tail fraction, μ and the tail energy scaling parameter T_T.

Figure (42) shows results from these calculations along with the experimental bounds . The Maxwellian limit is obtained when the tail fraction goes to zero. We recover there the result of ref. [2]. It is thus clear that even under the most favorable conditions, Maxwellian electrons cannot account for the smallness of λ_i. It is also clear that at these conditions, tail fractions of the order of a few percent can bring down λ_i in the millimeter range that contains the experimentally measured values.

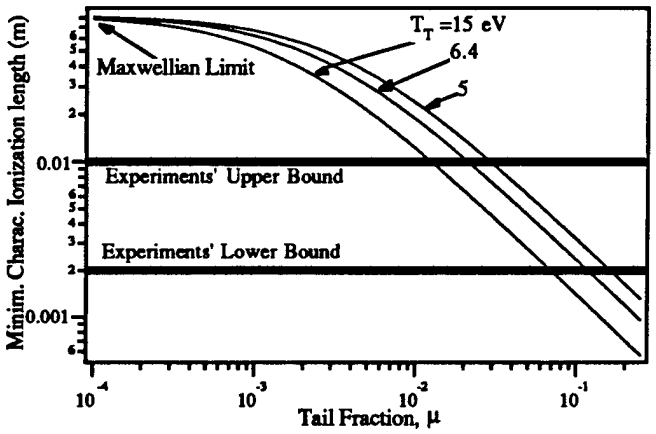

Figure 42: Calculated minimum values of λ_i as a function of the tail fraction. T_e=2.0 eV, $\tau = 1$. Experimental values from ref. [2]

It should also be noted that λ_i is not always a monotonic function of the tail parameters due to the complex interplay between the tail's shape and the cross-section-energy dependence. Depending on the energy level and the tail parameters, contributions to λ_i from allowed, spin-forbidden and parity-forbidden transitions alternate in importance.

An illustration of how increasing the tail's energy scaling parameter T_T can either increase or decrease λ_i is shown in Fig. (43). The curves go through a minimum around 20 eV. At that minimum, tail fractions of 1 percent and higher can bring λ_i down to within the experimental bounds.

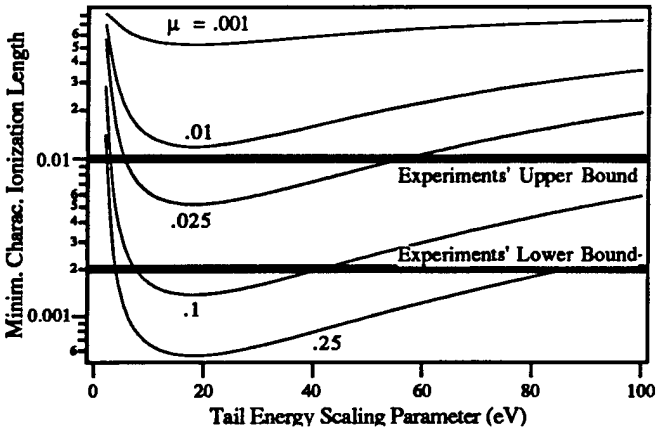

Figure 43: Calculated minimum values of λ_i as a function of the tail energy scaling parameter, T_T. T_e=2.0 eV, $\tau = 1$. Experimental values from ref. [2]

8.4 Insight from Particle Simulations of CIV Tests in Space

The calculations above are based on assumed or parametrically varied tail parameters. Some a priori knowledge of the extent of the departure of the distribution function from the Maxwellian case is required and can be in principle be obtained from 1) Experiments, 2) nonlinear or quasilinear plasma theory or 3) particle simulations.

In this section we briefly illustrate how some insight on the sizing of suprathermal tail parameters can be obtained from particle simulation codes.

In particular, we use a particle code that we have been applying to the study of anomalous ionization through CIV tests using gas releases from an orbiting spacecraft. The code is a $2\frac{1}{2}$-dimensional, electrostatic particle-in-cell (PIC) code in a slab geometry. It includes guiding center approximations for the electrons and the full dynamics for the ions and allows simulations with real mass ratios. A Monte Carlo collision operator is added to the self-consistent particle motion in order to model various collisional processes inherent to interaction studies. The code's nucleus has been described in detail by Lee and Okuda[47].

We have been studying, using this code, the CIV test conducted recently onboard the ATLAS-1 mission[23]. The simulation geometry is shown schematically in Fig. (44).

The dimensions of the simulations are 256 by 1024 cm and the plasma conditions are those of the ionosphere in LEO at high latitudes. In particular, we

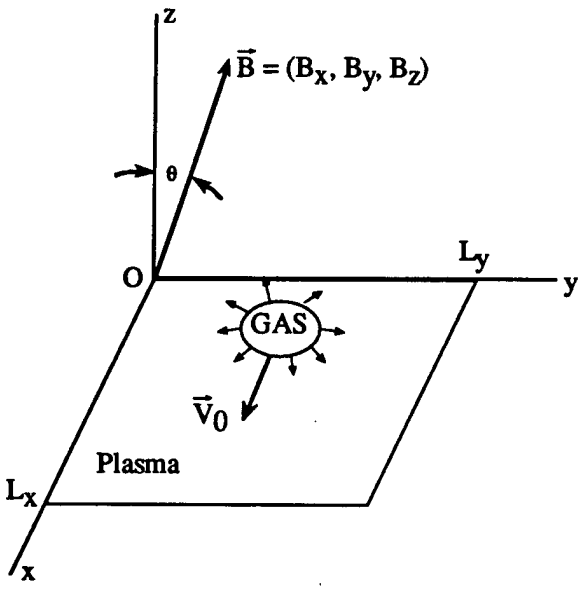

Figure 44: Configuration for the particle simulation study of anomalous ionization. The neutral gas (xenon) which is injected from an orbiting spacecraft is expanding and moving with respect to the ionospheric plasma with the orbital velocity v_0 and is subject to collective ionization (CIV).

have $n_e = 2\times10^5 \text{cm}^{-3}$, $T_e = 0.1\ eV$ and the magnetic field $B = .5\gamma$. The neutral gas which is injected from the orbiting spacecraft is expanding and moving with respect to the ionospheric plasma with the orbital velocity v_0 and is subject to collective ionization (CIV).

Figure (45) shows a planar contour map of the electrostatic potential over the plasma slab a few thousand plasma periods (about .2 msec) into the simulation. The coherent structure reflects the presence of strong plasma oscillations which are central to the electron energization process. The electron energization is illustrated in the associated plot of the electron distribution function shown in Fig. (46) where the formation of a suprathermal electron tail can be seen.

In terms of the parameters of the model in Section 8.1, the following numerical values can be extracted by fitting the model to the simulation results (after setting $\tau = 1$): $\mu \simeq .02$, $T_T \simeq .32\ eV$.

If we use the ratio $T_T/T_B = 3.2$ from the simulations to scale the tail of the distribution function for the low power thruster studied in Section 8.3, we would get $T_T = 6.4$. The λ_i values for $T_T = 6.4$ have been purposely plotted

Figure 45: Contour map of the electrostatic potential over the simulation slab showing coherent structure that reflect the presence of strong plasma oscillations.

in Fig. (42) to illustrate this case. It can be seen from that figure that, for this value and for the tail fraction inferred from the simulation, we get a λ_i of a few millimeters.

8.5 Concluding Remarks on Analytical Modeling of Anomalous Ionization in MPD Thrusters

A prescription for the electron energy distribution function that allows the representation of suprathermal electron tails such as those produced by the nonlinear effects of plasma microturbulence has been combined with a detailed model of collisional excitation in argon. The resulting tool was used to investigate the effects of suprathermal tails on the minimum characteristic length for ionization. The ionization length which is at least 10 times smaller than that calculated assuming Maxwellian statistics is shown to be more consistent with distributions having suprathermal tail fractions and energies that could be produced by plasma microturbulence.

The numerical model can be easily extended to include other radiative-collisional processes. Ultimately, it can be used in fluid flow codes of the MPD thruster as an interface between the atomic physics and the nonlinear collective plasma processes.

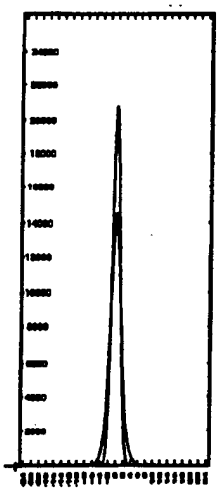

Figure 46: The velocity distribution functions $f(v_{ez})$, (where v_{ez} is the electron velocity along the magnetic field), at $t = t_0$ (large peak) and at a later time (small peak) showing the formation of the tail.

9 Non-technical Material

9.1 Publications supported by the AFOSR Grant

We have published results from this work in the following peer-reviewed journals

- *Physics of Plasmas*
- *Geophysical Research Letters*
- *Advances in Space Research*

The following six papers from the AFOSR-supported work, listed in the reference list and referred to here with a citation number, have already been published: refs. [56, 24, 23, 57, 53, 58].

The following five technical reports, listed in the reference list and referred to here with a citation number, have been published worldwide: [59, 60, 61, 62, 34].

ref. [53] was voted best paper in the Plasma Thruster Theory Session at the 23^{rd} International Electric Propulsion Conference.

9.2 Particpating Professionals under this Contract

- Dr. Edgar Y. Choueiri, Chief Scientist and Manager of EPPDyL, Princeton University.

- Prof. Robert G. Jahn, Professor of Aerospace Sciences, MAE dept. Princeton University.
- Prof. Hideo Okuda, Senior Physicist with Rank of Professor, Plasma Physics Lab. Princeton University.
- Dr. Torsten Neubert, Senior Physicist, Space Physics Research Lab (SPRL), University of Michigan.
- Prof. Victor Oraevsky, Director of IZMIRAN, Moscow Russia.
- Dr. Vladimir Dokukin, Physicist, IZMIRAN, Moscow Russia
- Dr. Alexander Volokitin, Physicist, IZMIRAN, Moscow Russia

9.3 Student Participation

The following students participated in the investigations supported by this AFOSR contract:

- Brian Kantsiper, Physics Department, Princeton University.
- Marlo Graves, MAE Department, Princeton University.
- Jonathan Nichols, MAE Department, Princeton University.

9.4 Professional Interactions

We have presented various results from this work at the following seven conferences:

- American Geophysics Union (AGU) Fall Meeting, San Francisco CA, 1992
- AGU Spring Meeting, Baltimore MD, 1993
- American Physical Society (APS) Plasma Physics Annual Meeting, Aneheim CA, 1993 (Invited Talk)
- IAGA Conference, Buenos Aires Argentina, 1993
- International APEX Workshop, Warsaw Poland, 1994
- COSPAR Meeting, Hamburg Germany, 1994
- AIAA Plasma Dynamics and Lasers Conference, Colorado Spring, CO 1994
- International Electric Propulsion Conference, Seattle WA, 1994

Level n	Designation	Excitation energy (eV)	Type of transition	Coefficients α_{1j}^{F} or $\alpha_{1j}^{A} f_{1j}^{A}, \beta_{1j}$
1	$3p^6$	0	-	-
2	$4s[3/2]_2$	11.548	S	6.70×10^{-2}
3	$4s[3/2]_1$	11.624	A	1.92×10^{-2},4
4	$4s'[1/2]_0$	11.723	S	9.50×10^{-3}
5	$4s'[1/2]_1$	11.828	A	4.62×10^{-2},4
6	$4P[1/2]_1$	12.907	P	3.5×10^{-2}
7	$4P[3/2]_{1,2}, [5/2]_{2,3}$	13.116	P	1.15×10^{-1}
8	$4P'[3/2]_{1,2}$	13.295	P	3.50×10^{-2}
9	$4P'[1/2]_1$	13.328	P	7.00×10^{-3}
10	$4P[1/2]_0$	13.273	P	7.00×10^{-3}
11	$4P'[1/2]_0$	13.480	P	3.50×10^{-2}
12	$3d[1/2]_{0,1}, [3/2]_2$	13.884	S	1.50×10^{-1}
13	$3d[7/2]_{3,4}$	13.994	S	9.00×10^{-2}
14	$3d'[3/2]_2, [5/2]_{2,3}$	14.229	P	4.20×10^{-2}
15	$5s'$	14.252	A	3.71×10^{-3},4
16	$3d[3/2]_1, [5/2]_{2,3} + 5s$	14.090	A	3.33×10^{-2},4
17	$3d'[3/2]_1$	14.304	A	1.79×10^{-2},2
18	$5p$	14.509	P	7.00×10^{-2}
19	$5p'$	14.690	P	5.00×10^{-2}
20	$4d + 6s$	14.792	A	5.15×10^{-2},1
21	$4d' + 6s'$	14.976	A	3.06×10^{-2},1
26	$5d' + 7s'$	15.324	A	6.50×10^{-4},1
27	$5d + 7s$	15.153	A	3.69×10^{-2},1
33	$6d + 8s$	15.347	A	2.40×10^{-2},1

Table 5: Data for the 23 transitions considered in our calculations. A, optically allowed; P, parity-forbidden; S, spin-forbidden transitions. From ref. [3]

References

[1] S. Sasaki, S. Kubota, N. Kawashima, K. Kuriki, M. Yanagisawa, T. Obayashi, W.T. Roberts, D.L. Reasoner, W.W.L. Taylor, P.R. Williamson, P.M. Banks, and J.L. Burch. An ehnacement of plasma density by neutral gas injection observed in SEPAC Spacelab-1 experiment. *Journal of Geomagnetism and Geoelectricity*, 37:883–894, 1985.

[2] T.M. Randolph, W.F. Von Jaskowsky, A. J. Kelly, and R. G. Jahn. Measurement of ionization levels in the interelectrode region of an MPD thruster. In 28^{th} *Joint Propulsion Conference*, Nashville, TN, 1992. AIAA-92-3460.

[3] J. Vlcek. A collisional-radiative model applicable to argon discharges over a wide range of conditions. *Journal of Physics D*, 22:623–631, 1989.

[4] E.Y. Choueiri, A.J. Kelly, and R.G. Jahn. Plasma instabilities and transport in the MPD thruster. Final Technical Report to AFOSR. Technical Report AFOSR Contract No. AFOSR-91-0162, EPPDyL, Princeton University, 1994.

[5] A.P. Bruckner. *Spectroscopic Studies of the Exhaust Plume of a Quasi-Steady MPD Accelerator*. PhD thesis, Princeton University, Princeton, NJ, USA, 1972.

[6] E.Y. Choueiri, A.J. Kelly, and R.G. Jahn. The manifestation of Alfvén's hypothesis of critical ionization velocity in the performance of MPD thrusters. In 18^{th} *International Electric Propulsion Conference*, Alexandria, Virginia, USA, 1985. AIAA-85-2037.

[7] N. Brenning. Review of the CIV phenomenon. *Space Science Reviews*, 59:209–314, 1992.

[8] E.Y. Choueiri, A. J. Kelly, and R. G. Jahn. Current-driven plasma acceleration versus current-driven energy dissipation part II : Electromagnetic wave stability theory and experiments. In 22^{nd} *International Electric Propulsion Conference*, Viareggio, Italy, 1991. IEPC-91-100.

[9] D.L. Tilley, E.Y. Choueiri, A.J. Kelly, and R.G. Jahn. An investigation of microinstabilities in a kW level self-field MPD thruster. In 22^{nd} *International Electric Propulsion Conference*, Viareggio, Italy, 1991. IEPC-91-122.

[10] E.Y. Choueiri, A. J. Kelly, and R. G. Jahn. Current-driven instabilities of an electromagnetically accelerated plasma. In 20^{th} *International Electric Propulsion Conference*, Garmisch-Partenkirchen, W. Germany, 1988. AIAA-88-042.

[11] N. Brenning. Review of the CIV phenomenon. *Space Science Reviews*, 59:209–314, 1992.

[12] V.A. Abramov, A.K. Vinogradova, Y.P. Dontsov, Y.A. Zavenyagin, P.E. Kovrov, V.I. Kogan, and A.I. Morozov. Investigation of electron temperature and plasma radiation in a quasi-stationary high-current discharge between coaxial electrodes. In *Proceedings of the Eighth International Conference on Phenomena in Ionized Gases*, 1968. Panel 33.1.11.

[13] R.K. Seals and H.A. Hassan. Analysis of MPD arcs with nonequilibrium ionization. *AIAA Journal*, 6(12):1452–1454, 1968.

[14] E.J. Sheppard and M. Martinez-Sanchez. Nonequilibrium ionization in MPD thrusters. In 21^{st} *International Electric Propulsion Conference*, Orlando, Florida, 1990. AIAA-90-2608.

[15] E.J. Sheppard and M. Martinez-Sanchez. Ionization ignition at the inlet of an MPD thruster. In 22^{nd} *International Electric Propulsion Conference*, Viareggio, Italy, 1991. IEPC-91-088.

[16] E. Möbius, R.W. Boswell, A. Piel, and D. Henry. A Spacelab experiment on the critical ionization velocity. *Geophysical Research Letters*, 6:29–31, 1979.

[17] G. Haerendel. Alfvén's critical velocity effect tested in space. *Z. Naturforsch*, 37a:728–735, 1982.

[18] R.B. Torbert. Review of critical velocity experiments in the ionosphere. *Advances in Space Research*, 10:47–58, 1990.

[19] C.M. Swenson, M.C. Kelley, F. Primdahl, and K.D. Baker. CRIT II Electric, Magnetic, and Density Measurements within an Ionizing Neutral Stream, 1991. To be published in Geophysical Research Letters.

[20] C.M. Swenson, S. Mende, R. Meyerott, and R. Rairden. Charge exchange contamination of CRIT II barium CIV experiment, 1990. Unpublished.

[21] E.Murad and C. Lai, 1992. Personal communication.

[22] S. Sasaki, N. Kawashima, K. Kuriki, M. Yanagisawa, T. Obayashi, W.T. Roberts, D.L. Reasoner, W.W.L. Taylor, P.R. Williamson, P.M. Banks, and J.L. Burch. Gas ionization induced by a high speed plasma injection in space. *Geophysical Research Letters*, 13(5):434–437, 1986.

[23] J.A. Marshall, J.L. Burch, E.Y. Choueiri, and N. Kawashima. CIV experiments on ATLAS-1. *Geophysical Research Letters*, 20(6):499–502, 1993.

[24] J.L. Burch, W.T. Roberts, W.L. Taylor, N. Kawashima, J.A. Marshall, S.L. Moses, T. Neubert, S.B. Mende, and E.Y. Choueiri. Space experiments with particle accelerators: SEPAC. *Advances in Space Research*, 14(9):(9)263–(9)270, 1994.

[25] S.T. Lai and E. Murad. Inequality conditions for critical velocity ionization space experiments, 1992. Accepted for Publication in IEEE Transactions on Plasma Science.

[26] M. Tanaka and K. Papadopoulos. Creation of high-energy electron tails by means of the modified two-stream instability. *Physics of Fluids*, 26:1697–1699, 1983.

[27] K. Papadopoulos. On the shuttle glow: The plasma alternative. *Radio Science*, 19:571, 1984.

[28] N. Brenning. Experiments on the critical ionization velocity interaction in weak magnetic fields. *Plasma Physics*, 23:967, 1981.

[29] I. Axnäs and N. Brenning. Experiments on the magnetic field and neutral density limits on CIV interaction. *Advances in Space Research*, 10:27–30, 1990.

[30] S. Lai, W. McNeil, and E. Murad. The role of metastable states in critical ionization velocity discharges. *Journal of Geophysical Research*, 93(A6):5871–5878, 1988.

[31] S. Lai, E. Murad, and W. McNeil. An overview of atomic and molelcular processes in critical velocity ionization. *IEEE Transactions of Plasma Science*, 17:124, 1989.

[32] G. Haerendel. The role of momentum transfer to the ambient plasma in critical ionization velocity experiments. Technical Report SP-195, European Space Agency, Neuilly, France, 1983.

[33] N. Yanagisawa, S. Sasaki, N. Kawashima, and T. Obayashi. SEPAC data base product tape. Technical Report ISAS RN 283, Institute of Space and Astronautocal Science (ISAS), Tokyo, Japan, 1985.

[34] E.Y. Choueiri and J. Marshall. Processing of wave data recorded during the CIV tests on ATLAS-1 In the November/December Bimonthly Progress Report of the Electric Propulsion and Plasma Dynamics Laboratory. Technical Report MAE 1776.40, EPPDyL, Princeton University, 1992.

[35] E.Y. Choueiri, J.A. Marshall, J.L. Burch, H. Okuda, and N. Kawashima. Collective plasma phenomena observed during the CIV tests on ATLAS-1. In *1993 Spring Meeting of the American Geophysical Union*, page 233, Baltimore, CA, 1993. SA51C-10.

[36] J.O. Nichols. Analysis of ATLAS-1 CIV test data Junior Independent Project, . Technical report, MAE Dept., Princeton University, 1994.

[37] T. Neubert, 1994. Space Physics Lab, University of Michigan. Personal communication.

[38] I. Axnäs. Some necessary conditions for a critical velocity interaction between the ionospheric plasma and a xenon cloud. *Geophysical Research Letters*, 7:933–936, 1980.

[39] R.J. Biasca. *Numerical Simulation of the Crirical Ionization Velocity Mechanism.* PhD thesis, Massachusetts Institute of Technology, Cambridge, MA, USA, 1992.

[40] J.D. Person, H. Resendes, and D. Hastings. Effects of collisional processes on the critical ionization velocity hypothesis. *Journal of Geophysical Research*, 95:4039, 1990.

[41] S. Machida, T. Abe, and T. Terasawa. Computer simulation of critical ionization velocity. *The Physics of Fluids*, 27:1928, 1984.

[42] T. Abe and S. Machida. Production of high energy electrons caused by counterstreaming ion beams in an external magnetic field. *The Physics of Fluids*, 28:1178, 1985.

[43] S. Machida and C. Goertz. The electromagnetic effect on the critical ionization velocity. *Journal of Geophysical Research*, 93:11495, 1988.

[44] S. Machida, C. Goertz, and G. Lu. Simulation study of the ionizing front in the critical ionization velocity phenomenon. *Journal of Geomagnetism and Geoelectricity*, 40:1205, 1988.

[45] W. McNeil, S. Lai, and E. Murad. Interplay between collective and collisional processes in critical velocity ionization. *Journal of Geophysical Research*, 95:10345, 1990.

[46] S. Machida and C. Goertz. A simulation study of the critical ionization velocity process. *Journal of Geophysical Research*, 91:11965, 1986.

[47] W.W. Lee and H. Okuda. A simulation model for studying low frequency microinstabilities. *Journal of Computational Physics*, 26:139, 1978.

[48] C.K. Birdsall, 1991. IEEE Trans. Plasma Sci. **19**, 65.

[49] M. Matic, V. Sadis, M. Vujovic, and B. Cobic, 1990. J. Phys. B: Atom, Molec. Phys. **13**, 3665.

[50] D. Rapp and P. Englander-Golden. Total cross sections for ionization and attachement in gases by electron impact I. Positive ionization. *Journal of Chemical Physics*, 43(5):1464–1479, 1965.

[51] J.M. Kindel, H. Okuda, and J.M. Dawson, 1972. Phys. Rev. Lett. **29**, 995.

[52] E. Moghaddam-Taaheri and C.K. Goertz. Quasilinear numerical study of the critical ionization velocity effect. *Journal of Geophysical Research*, 98(A2):1443, 1993.

[53] E.Y. Choueiri and H. Okuda. Anomalous ionization in the MPD thruster. In 23^{rd} *International Electric Propulsion Conference*, Seattle, WA, USA, 1993. IEPC-93-067.

[54] T.M. Randolph, 1993. Personal communication.

[55] H.W. Drawin. Collision and transport cross-sections. Technical Report EUR-CEA-FC-383, Euratom-CEA, 1967.

[56] H. Okuda and E.Y. Choueiri. Numerical simualtion of neutral gas release experiments in the ionosphere. *Physics of Plasmas*, 1:1669–1675, 1994.

[57] E.Y. Choueiri and H. Okuda. Studies of anomalous ionization. In 25^{th} *AIAA Plasmadynamics and Lasers Conference*, Colorado Springs, CO, 1994. AIAA-94-2465.

[58] H. Okuda and E.Y. Choueiri. Numerical simualtion of neutral gas release experiments in the ionosphere. *Bulletin of the American Physical Society*, 38:2042, 1993.

[59] E.Y. Choueiri. Contributions to the Semi-Annual Progress Report for the period June 1994-December 1994. Technical Report No. EPPDyL-TR-94F, EPPDyL, Princeton University, 1994.

[60] E.Y. Choueiri and J.A. Marshall. CIV experiments on ATLAS-1 In the May/June Bimonthly Progress Report of the Electric Propulsion and Plasma Dynamics Laboratory. Technical Report MAE 1776.37, EPPDyL, Princeton University, 1992.

[61] E.Y. Choueiri and B. Kantsiper. Plasma wave physics of the xenon releases on ATLAS-1 In the July/August Bimonthly Progress Report of the Electric Propulsion and Plasma Dynamics Laboratory. Technical Report MAE 1776.38, EPPDyL, Princeton University, 1992.

[62] E.Y. Choueiri. Charge exchange ionization of an expanding neutral gas cloud released in the ionosphere In the September/October Bimonthly Progress Report of the Electric Propulsion and Plasma Dynamics Laboratory. Technical Report MAE 1776.39, EPPDyL, Princeton University, 1992.